



TAMPEREEN TEKNILLINEN YLIOPISTO
TAMPERE UNIVERSITY OF TECHNOLOGY

Marja Mettänen

**Measurement of Print Quality: Joint Statistical Analysis
of Paper Topography and Print Defects**



Julkaisu 935 • Publication 935

Tampere 2010

Tampereen teknillinen yliopisto. Julkaisu 935
Tampere University of Technology. Publication 935

Marja Mettänen

Measurement of Print Quality: Joint Statistical Analysis of Paper Topography and Print Defects

Thesis for the degree of Doctor of Science in Technology to be presented with due permission for public examination and criticism in Sähköotalo Building, Auditorium S4, at Tampere University of Technology, on the 10th of December 2010, at 12 noon.

Tampereen teknillinen yliopisto - Tampere University of Technology
Tampere 2010

ISBN 978-952-15-2477-6 (printed)
ISBN 978-952-15-2503-2 (PDF)
ISSN 1459-2045

Abstract

Printing papers constitute 45 % of the global paper consumption. As printed products compete with electronic media, printability has become increasingly important as a cost-efficiency factor. It refers to the properties of the paper that ensure trouble-free running through the printing machine and high print quality. The treatment of printability in this thesis is constrained to print quality. The focus is on the dependences between print unevenness caused by small-scale print defects and the local characteristics of paper surface. The dependences are sought using image based measurements.

A set of probabilistic analysis methods is proposed and applied to 2D maps of print reflectance and surface topography. A cross-correlation based image registration procedure is first presented to align the images acquired before and after printing. The large amount of data in the aligned images is used to estimate the joint probability density of print reflectance and surface topography. As the probability density deviates from that of multivariate normal distribution, Gaussian mixture modeling is chosen as a flexible parametric representation of the density estimate. The statistical dependence between print reflectance and surface topography is then quantified by mutual information, thus avoiding any assumptions about the linear or nonlinear nature of the dependence. The results from offset printed newsprint and gravure printed supercalendered papers suggest that linear models cannot entirely capture the dependences.

The presented analyses are largely concentrated on the low probability tail areas of the distributions that correspond to the abnormally high print reflectance values and deep depressions on the paper surface. Presenting the locations of these extreme values as anomaly maps allows the evaluation of the conditional probability of finding missing ink in regions that exhibit abnormal behavior of surface topography. The results indicate that missing ink in the examined samples is considerably more probable in regions of abnormal surface topography than in randomly selected regions. As expected, however, a majority of the missing ink spots are attributed to other reasons than surface depressions. Anomaly maps are also used to select subsets of the multivariate data, and mutual information is evaluated in these subsets. The dependences expressed by mutual information are weak, but simulations verify that they are statistically significant. The capability of the surface topography values to explain print reflectance is higher in the most abnormal points of topography than overall in the images.

The photometric stereo principle applied in this work is a fast method for acquiring surface topography maps that, based on the results, carry information about the printability of the paper. In addition, the probabilistic methods are expected to be applicable to several property maps besides print reflectance and surface topography. The characterization of the probabilistic dependences serves the Bayesian modeling of print quality as a combination of attributes related to the unprinted and printed paper.

Preface

The research presented in this thesis has been carried out at the Department of Automation Science and Engineering at Tampere University of Technology (TUT), Finland, during the years 2005-2010. The funding received from the PMGS graduate school of TUT is gratefully acknowledged. It is a pleasure to thank the people who have made this thesis possible.

First, I would like to express my gratitude to my supervisor, Professor Risto Ritala for his guidance and support throughout this study. I am grateful for the possibility to work at the department and to get involved with this interesting field of research. I would also like to thank Dr. Ulrich Hirn and Professor Wolfgang Bauer for the opportunity of working in their research group in Graz, Austria, during the spring and summer in 2008. It was a very inspiring experience.

The work for this thesis has been carried out during two projects, PapSurface and DigiQ, both funded by the Finnish Funding Agency for Technology and Innovation (TEKES) and by several Finnish and international companies in the paper and printing industry. I am grateful to the project partners for the financial support and for the technical insight and input. In particular, I would like to thank Päivi Miettinen and Mika Anttila from FPC, Bo Sundqvist from Stora Enso and Juha Lahtinen from UPM for their contribution to the measurement data. I also want to thank Dr. Toni Kuparinen from LabVision Technologies for working so persistently for our common research purposes.

The colleagues I have worked with during these years deserve the warmest gratitude for making the work enjoyable and for giving advice whenever needed. I am especially grateful to my co-authors, laboratory engineer Heimo Ihalainen, M.Sc. Mikko Lauri, M.Sc. Pekka Kumpulainen, Dr. Ulrich Hirn and Professor Risto Ritala, for their valuable contribution. I also greatly appreciate the technical expertise and help from Mr. Matti Jukola, M.Sc. Kalle Rynnänen and M.Sc. Juuso Grén.

The constructive comments from the reviewers of this thesis, Dr. Jukka Ketoja from VTT, Finland, and Dr. William Sampson from the University of Manchester, UK, are gratefully appreciated.

Finally, I like to thank my friends and family for support and understanding. I am particularly grateful to my parents who have been an unfailing source of encouragement in all my ambitions. I also wish to express my sincere gratitude to my husband Hannu for always being there for me.

Tampere, December 2010

Marja Mettänen

Contents

Abstract.....	i
Preface	iii
Contents	v
List of acronyms	vii
List of symbols	ix
List of publications	xiii
1 Introduction.....	1
1.1 Status of paper and printing industry in Finland	1
1.2 Research problem.....	2
1.3 Hypotheses and objectives	3
1.4 Contributions and limitations	4
1.5 Outline of the thesis.....	5
2 Quality of printed products and paper.....	7
2.1 Printability and print quality.....	8
2.1.1 Subjective quality assessment.....	8
2.1.2 Technical quality	10
2.2 Physical properties of paper	11
2.2.1 Air-leak testers.....	13
2.2.2 Topographical scanning and imaging	14
2.2.3 Contact area measurements	18
2.3 Literature on the dependence between print quality and paper surface properties ...	18
3 Methods for quantifying statistical dependence.....	23
3.1 Probability density.....	24
3.1.1 Histogram and kernel density estimates	25
3.1.2 Gaussian mixture model	26
3.2 Characterization of statistical dependence	29
3.3 Bayes network	32

4	Methods applied to paper and print quality analysis.....	37
4.1	Image acquisition	37
4.2	Image alignment	40
4.3	Statistical analysis methods	42
4.3.1	Preprocessing	43
4.3.2	Non-Gaussianity of probability densities	44
4.3.3	Anomaly maps	45
4.3.4	Mutual information and its significance	47
5	Experiments and results	51
5.1	Measurement data.....	51
5.2	Non-Gaussianity	53
5.3	Coincidence of anomalies	54
5.4	Mutual information.....	57
5.5	Discussion	59
6	Conclusions.....	63
	Bibliography	65
	Publications	75

List of acronyms

AFM	atomic force microscope
BN	Bayes network
CCD	charge-coupled device
CIE	Commission Internationale d'Eclairage
CLSM	confocal laser scanning microscope
COV	coefficient of variation
DFT	discrete Fourier transform
dpi	dots per inch
EM	expectation maximization
FFIF	Finnish Forest Industries Federation
GMM	Gaussian mixture model
ISO	International Organization for Standardization
I3A	International Imaging Industry Association
KL	Kullback-Leibler
LWC	light weight coated
MCMC	Markov chain Monte Carlo
MI	mutual information
ML	maximum likelihood
MP	multi-planar
pdf	probability density function
PPS	Parker Print Surf

PQE	perceptual quality element
RGB	red, green, blue
RMS	root mean square
SC	supercalendered
SEM	scanning-electron microscope
SFO	sheet-fed offset
SNR	signal-to-noise ratio
UCA	uncovered areas

List of symbols

\mathbf{C}, \mathbf{C}_i	covariance matrix (of the i th component in GMM)
$C(q)$	limit value of probability density to make anomaly map of abnormality degree q
c_i	weight of the i th component in GMM
D_{KL}	Kullback-Leibler distance
D	print density
d	dimensionality (of a random variable)
e	the base of natural logarithm
$F(m,n)$	intensity image
$f(x)$	probability density function of real-valued random variable X
\mathbf{h}	width of histogram bin
h_G	bandwidth of Gaussian kernel
h_{opt}	an optimal width of histogram bin (in one dimension)
$I(X;Y)$	mutual information between X and Y
\mathbf{I}_d	identity matrix
I_R	intensity of reflected light
I_0	intensity of incident light
$\mathcal{J}(u,v)$	imaginary part of Fourier coefficient
i	imaginary unit, $\sqrt{-1}$
K	number of parameters to specify a GMM
k	number of GMM components

x	
L	log likelihood
L^*, a^*, b^*	coordinates of the CIELAB color space
M	number of histogram bins (in one dimension)
$\mathcal{M}(u,v)$	amplitude of Fourier coefficient
m,n	horizontal and vertical image coordinates in spatial domain
N	number of observations
$\mathcal{N}(\mathbf{x} \boldsymbol{\mu},\mathbf{C})$	Gaussian distribution
P	probability
$p(x)$	probability density function of discrete-valued random variable X
q	abnormality degree, i.e., mask percentage
R	reflectance of the print
R_q	RMS roughness from line profile
R^2	coefficient of determination
$\mathcal{R}(u,v)$	real part of Fourier coefficient
S_m, S_n	width and height of an image
S_q	RMS roughness from surface
s_j	sample standard deviation in the j th dimension
u,v	spatial frequencies in horizontal and vertical direction
w_{ij}	responsibility of the i th GMM component in generating the j th observation
X,Y	random variables (vector when boldface)
x,y	observed values of random variables (vector when boldface)
$\alpha_i(\mathbf{x})$	auxiliary term of the i th GMM component in GMM regression
γ	illumination angle in photometric stereo
δ	distance parameter of control points in the first phase of image registration
$\boldsymbol{\theta}$	parameter vector of GMM
λ_{\max}	upper wavelength limit of surface topography maps
μ, μ_i	expected value (of the i th component in GMM)
ρ	correlation coefficient

$\sigma, \sigma_X, \sigma_Y$	standard deviation
$\phi(u, v)$	phase of Fourier coefficient

List of publications

This thesis is based on the following publications:

- I Lähdekorpi¹, M., Ihalainen, H. and Ritala, R. (2006): Using image registration and alignment to compare alternative 2D measurements. *Proc. XVIII IMEKO World Congress*, Rio de Janeiro, Brazil, September 2006.
- II Mettänen, M., Ihalainen, H. and Ritala, R. (2008): Alignment and statistical analysis of 2D small-scale paper property maps. *Appita Journal*, Vol. 61, No. 4, pp. 323-330.
- III Mettänen, M., Lauri, M., Ihalainen, H., Kumpulainen, P. and Ritala, R. (2009): Aligned analysis of surface topography and printed dot pattern maps. *Proc. Papermaking Research Symposium*, Kuopio, Finland, June 2009.
- IV Mettänen, M., Hirn, U., Lauri, M. and Ritala, R. (2009): Probabilistic analysis of small-scale print defects with aligned 2D measurements. *Trans. 14th Fundamental Research Symposium: Advances in Pulp and Paper Research* (ed. S.J. I'Anson), Oxford, UK, September 2009, pp. 1293-1323.
- V Mettänen, M. and Ritala, R. (2009): Measurement as information channel with an application to printability. *Proc. XIX IMEKO World Congress*, Lisbon, Portugal, September 2009, pp. 1086-1090.
- VI Mettänen, M. (2010): Methods for measuring and predicting the printability of paper. *Nordic Pulp & Paper Research Journal*, Vol. 25, No. 3, pp. 391-404.

The author of this thesis made the following detailed contributions to the publications. For Publication I, the author registered the measurements spatially and wrote the article. The author was responsible for the multivariate image analyses and results, except for the spectral analysis of individual measurement maps that was performed by M.Sc. Ihalainen. The MATLAB® software for image registration and alignment used throughout this work was developed and implemented by the author of this thesis together with M.Sc.

¹ The surname of the author changed in October 2006. The maiden name, Lähdekorpi, is used in the publication before this date.

Ihalainen. The measurement data analyzed in Publication I was provided by Mr. Bo Sundqvist from Stora Enso. For publication II, the author participated in the image based measurements of the paper sheets before and after printing, registered the acquired images, performed all the analyses and drafted the entire manuscript. The photometric stereo based measurements utilized in Publication II, and later in Publications IV, V and VI, were made by M.Sc. Kalle Rynnänen. The author registered the images and wrote the main body of Publication III, in which M.Sc. Kumpulainen performed the analysis and documentation for the parts related to self-organizing maps and clustering, and the author was responsible for the rest of the analyses. The detection of the raster pattern from images of halftone print was developed and documented in co-operation between M.Sc. Lauri, the author, and M.Sc. Ihalainen. The photometric stereo based measurements utilized in Publication III were made by M.Sc. Juuso Grén. For Publication IV, the author of this thesis drafted the entire article and was responsible for all the analyses made. The manuscript was complemented by Dr. Hirn with paper physical background and interpretations. M.Sc. Lauri assisted in the implementation of the analysis tools and maintained the MATLAB® software by which the parameters of the continuous probability density function models were estimated. This software was used in Publications II, IV and VI. The author of this thesis wrote Publication V. For Publication VI, the author performed all the image analyses and wrote the manuscript.

1 Introduction

Printed media has an established position in the everyday life of millions of people. For instance, newspapers are one of the most significant mass media even in today's market where printed products compete with electronic media. Advertising in newspapers and magazines reaches a great number of people and it is affordable compared to advertising in television. The fact that readers and advertisers move to Internet, however, is a challenge to the printing industry and dampens the demand for printing papers. In order to maintain profitability, high-quality papers with reasonable price and cost-efficient printing with high print quality are required. This thesis aims to contribute to this area by proposing methods for the analysis of paper and print quality.

1.1 Status of paper and printing industry in Finland

Forest industry has been a prominent driving force of the growth of Finnish national economy in the 20th century. The share of forest products of the total value of exports per annum in Finland was 69 % in 1960 (Diesen 1998 (p. 23)). Since then the amount has declined steadily, but in 2009 it was still almost 20 %, larger than anywhere else in the world (FFIF² 2010). Forest industry gives work directly to 50 000 Finnish people, half of whom work with pulp and paper industry (FFIF 2010). Finland is the world's sixth largest producer of paper and paperboard (Finnish Forest Association 2010). Heavy modernizations have been necessary during the last decade to maintain the competitiveness of the Finnish paper industry, and this has shut down pulp and paper mills and reduced jobs. However, the forest sector is expected to serve the well-being and economic sustainability in Finland also in the future. Modern production facilities and the internationally recognized high-level knowledge of paper manufacturing and converting will be valuable in the ongoing renewal of the paper industry products.

Communications business provides a significant value added to paper and constitute a large customer group for Finnish paper. Particularly in Finland, printed products have a strong position in the market for media (FFIF 2010). A Finnish person spends on average one hour per day reading magazines and newspapers (FFIF 2010). The printing industry in Finland has also been enhanced by export to Russia. Like forest industry in general,

² Finnish Forest Industries Federation

printing industry is transforming to respond to the consumers' requirements and adapting to the coexistence of electronic and printed media. The recession has reduced advertising in printed media and caused overcapacity of paper and printing industry. The demand for newspapers and magazines is not predicted to increase in the developed countries, but increasing markets are found in Asia and South America (FFIF 2010). The demand for printed products in countries like Finland is expected to be maintained by the ageing of population, changes in life style due to upturn in the standard of living, increasing packaging, and new paper and paperboard products (FFIF 2010). Printed publications will not be superseded by electronic media because paper is a convenient user interface for many purposes and it is comfortable to read. Furthermore, paper is a lightweight and recyclable material.

The future trends of printing include the shortening of printing runs, closely targeted products with high quality requirements, and increase in digital printing (O'Neill et al. 2010). High-speed inkjet printers are being developed to satisfy the market demand. Offset is currently the most widely used printing technique and it is anticipated to maintain its position in the near future (Nutbeem et al. 2010). Offset presses are getting faster and wider, and the dot frequency in offset has increased from 150 dpi (dots per inch) to 300 dpi, which requires very homogeneous surface of the paper (O'Neill et al. 2010). Gravure printing can be expected to maintain its status as the technique providing very high quality and cost-effectiveness in notably large print runs.

1.2 Research problem

Printability is the quality potential of the paper as a substrate in a specified printing process (Suontausta 1999 (p. 183)). While the definition can be considered to include the runnability of the paper in the printing machine, the scope of this thesis rules out runnability issues and examines only print quality. Further definition is needed because the concept of quality is ambiguous. The quality of a printed product is ultimately judged by the customer, whose assessments of the product are likely to involve various aesthetic aspects and subjective preferences. In the lack of resources to examine all these aspects, and in the lack of a definition of quality that would make quality a measurable property (Ferris 2004), print quality is examined in this thesis through print defects: the presence of defects is interpreted to reduce the quality. The defects of particular interest are spots of inadequate or missing ink. They cause unevenness of the printed image, which can be visually disturbing on otherwise uniform image areas (Saarelma and Oittinen 1993).

Locally incompletely transferred ink can be caused by various reasons but usually not in a (locally) deterministic manner. In the printing methods studied in this work – offset and gravure – the transfer of ink from the printing cylinder to the paper involves the interaction of paper and ink properties combined with the settings of the printing press. If the defects related to the inking of the printing cylinder are ruled out, and if the local failures (i.e., breaking down) of the surface of the paper during printing can be neglected, the most prominent reason for missing ink is the incomplete contact between the paper

and the applied ink film (Kajanto et al. 1998; Lyne 1976b; Preston et al. 2008). The surface roughness and the conformability of the paper in the printing nip are therefore important paper properties in printing.

The surface roughness of paper is most commonly measured with standardized air-leak based laboratory equipment. They provide roughness indices that have been shown to correlate with the unevenness of print density (Bristow and Ekman 1981; Heintze 1982; Kajanto 1990; Parker 1971). On the other hand, it has been recognized early that compared to air-leak based measurements, a more precise description of the surface properties is the distribution of surface heights (Karttunen 1973; Parker 1973). Line profiles or surface height maps can be measured with scanning profilometers. In addition, a device based on photometric stereo and providing fast measurement of surface topography has been quite recently put on the market by the trade name of OptiTopo (Johansson and Hansson 2004). Aligned maps of surface topography and local print density are large data sets from which the point-wise dependence between topography and density can be analyzed. So far, few studies have been published that utilize such spatially aligned maps (Barros 2006; Dickson 2006; Hansson and Johansson 2000; Hirn et al. 2009; Mesic et al. 2006). In all of the cited studies both the density map and the topography map have been acquired from the printed paper. Weak linear dependence – correlation coefficients below 0.4 – between surface topography and print density has been found by the point-wise correlation of the aligned maps (Dickson 2006; Hirn et al. 2009). Linear correlation cannot, however, describe the potential non-linear dependences between the measured properties. Barros (2006) has thresholded the gray scale images of surface topography and print reflectance and indicated that the surface depressions of cardboard samples can explain part of the missing ink in flexographic printing. While the methods applied by Barros are interesting and straightforward to use, publications reporting the corresponding analysis in offset or gravure printed printing papers have not been found. The potential of the image based surface topography measurement in explaining and predicting the printability of paper could be investigated further.

The research problem of this thesis is to characterize the probabilistic relationship between small defects in ink coverage and the topographic features of the paper surface using image based measurements.

1.3 Hypotheses and objectives

In this work, the term print unevenness refers to unevenness of print density that is observed through image based measurement of print reflectance. It is hypothesized that the microstructure of paper affects its printability, and that fast camera based measurements of surface topography and print reflectance can be used to characterize this relationship. In contrast to the earlier publications, the topographic data is acquired before printing. This is feasible because the printing methods selected for experimenting use paper in sheets or small strips. The variations of surface topography and print reflectance

are studied on a wavelength range from hundredths of millimeters ($20\ \mu\text{m}$) to a few millimeters and the term small-scale variation is used to refer to this size scale.

The working hypothesis is that the point-wise dependences between the measured properties are non-deterministic and the properties may be non-linearly related to each other. The full joint probability density function (pdf) of the measured properties describes the dependences that are then quantified by mutual information (MI). MI is a generalized measure of statistical dependence that characterizes the interdependence of random variables without restricting the analysis to the Gaussian statistics.

The objective in this work is to present statistically justifiable methods for characterizing the dependences between paper properties and print quality. This includes the investigation into the predictability of aspects of print quality, such as the uniformity of print density on a given area, based on a measurement of a paper property before printing. The proposed analysis methods are prepared for both solid prints and raster patterns. The possibility of modeling the perceived print quality by Bayes network is considered. Bayes network is assumed to support the probabilistic inference about subjective print quality attributes given instrumental measurements of paper and/or print properties. The emphasis of the work is, however, on the probabilistic analysis of the dependences between the surface topography of paper before printing and the reflectance of the same area after printing.

1.4 Contributions and limitations

Methods have been developed for quantifying the statistical dependences between print quality and paper properties, and for predicting print defects given measurements of the paper properties before printing. The methods are intended for small-scale data acquired by image based measurement.

The main contributions of this work are:

- accurate image alignment that enables the joint analysis of small-scale 2D measurements of paper and print properties,
- introduction of probabilistic analysis methods into the analysis of dependences between local properties of paper and print, and subsequent quantification of the amount of information carried by a paper property measurement on a print quality property,
- verification of the statistical significance of the dependences by simulation based tests,
- presenting evidence that surface topography maps produced by the photometric stereo method carry information about printability,
- recognition of the Bayesian network as a means for relating instrumental measurements and perceived print quality.

The analysis methods presented in this thesis have been developed using surface topography as the physical property of paper that is to explain or predict the print quality. The methods are expected to be applicable to various properties of paper, for example local basis weight, but other measurements besides surface topography have not been tested in the context of print defect analysis. Another limitation concerns the paper grades. The image registration and alignment procedure has been tested with uncoated and coated paper and board, but the print quality analyses presented in this work has been restricted to uncoated papers.

This thesis contains six publications. Publication I introduces the image registration procedure and, using aligned surface topography maps from various devices, compares alternative methods for measuring the topography of paper. Linear models and spectral analysis reveal the basic strengths and weaknesses of the fast but indirect photometric stereo method that is used for surface topography measurement throughout the rest of this work. Publication II describes the framework for the statistical analysis of the small-scale image based measurements of print and paper properties, introducing the pdfs and the concentration of the analysis on the anomalies, i.e., the tails of the pdfs. Publications III and IV present the main results of this research, applying the analysis methods to gravure printed supercalendered (SC) paper and offset printed newsprint, respectively. Publication V connects the probabilistic analysis procedure to a wider information theoretic approach that pursues the modeling of the human perception of print quality. The main procedure proposed for the analysis and prediction of abnormal print quality is summarized in publication VI. It presents the components of the image based analysis procedure and discusses the advantages and observations regarding the application of the proposed methods to measurement data acquired before and after printing.

1.5 Outline of the thesis

The body of this dissertation is organized as follows. Chapter 2 first describes the subjective and objective dimensions of print quality and reviews methods for characterizing the small-scale properties of paper and its surface. A short summary is then given of the relevant existing approaches to quantifying the dependence between print and paper quality. Chapter 3 introduces the information theoretic principles and methods applied in this work for the characterization of probabilistic dependences. Chapter 4 describes the methods related to the image acquisition, preprocessing and analysis of the experimental data. Chapter 5 contains a summary of the results and discussion. Conclusions are drawn in Chapter 6.

2 Quality of printed products and paper

The purpose of a printed product, containing text and images, is to convey a message. The information transmitted by the product should be such that the receiver can easily interpret it in a manner intended by the sender. Consequently, the general requirements for the information channel – the printed product in this case – are the capability to transmit the information and the capability to preserve the nature of the message such that the likelihood of easy and correct interpretation is high. This perspective places great emphasis on the informativeness and naturalness of the printed work, where naturalness refers to the correspondence between the visual appearance of the product and the prior “knowledge of reality” stored in the memory of the receiver (Janssen and Blommaert 1997). Investigations into the subjectively assessed image quality (Janssen and Blommaert 1997; Leisti et al. 2009) confirm that these attributes really play an important role in the communication through images. The relative relevance of informativeness (also referred to as usefulness or clarity), naturalness, and other attributes present in the subjective assessment of the image, depends on the context and content of the transmitted message (Nyman et al. 2006).

Communication through printed work involves four principal elements: the content of the message (image), the carrier (paper), the transfer of the message to the carrier (printing) and the retrieval of the message (human visual system). All four elements are relevant to the study of printability, a concept to be discussed in Section 2.1. In practice, as stated in (Oittinen and Saarelma 1998 (p. 119)), printability studies often omit the high-level communication perspective and concentrate on the structure of paper and on the interactions between paper and the printing press variables. In the current chapter, the higher level concepts related to the message retrieval and the effects of image content are borne in mind, but the focus is on the small-scale structure of paper and its predictive capability with respect to the print quality.

Paper, the carrier of the printed message, is an intricate topic in itself, and a subject to textbooks such as (Niskanen 1998). Paper is a planar structure that consists of a stochastic network of fibers together with fillers (minerals) and chemicals. The random process by which the fibers and other constituents settle in the web causes the mass to be non-uniformly distributed along the plane. This is observed also visually as the non-uniform appearance of paper sheets illuminated from the side opposite to the viewing side. More generally, the random process of paper forming, together with the properties of the raw materials, induces the statistical geometry of the fibrous network, for instance pore size

distribution (Corte and Lloyd 1965). The arrangement of the constituents of paper largely determines its functional properties, such as the printing properties. The stochastic nature of paper also inspires the probabilistic approach chosen in this work for the characterization of the dependences between print quality and paper properties.

This chapter is a brief review of the methods for characterizing paper and print quality. Section 2.1 discusses printability and introduces the basic approaches to characterizing print quality. The paper physical background related to this work is presented in Section 2.2, with the emphasis on the surface structure of paper. A short summary of previously published studies on the relationship between paper and print quality is presented in Section 2.3.

2.1 Printability and print quality

The concept of printability of paper is ambiguous yet of high practical importance in the communication and operation of paper and printing industry. Printability is the quality potential of the paper as a substrate in a specified printing process (Suontausta 1999 (p. 183)). A closely related concept, runnability, refers to the efficiency of the printing in terms of speed and absence of trouble, without compromising the quality. When runnability is regarded as a part of the quality potential of paper, a paper of good printability is such that it does not jam or break in the printing process, withstands post-press operations without ink smearing or papers sticking together, and has high print quality. The treatment of printability in this thesis is focused on print quality. Suontausta (1999) defines print quality as the quality of the printed image, but quality itself is ambiguous. Subjective quality can be judged by human observers, and technical measurements provide objective indices to describe the quality properties. The relation between the visually detected quality parameters and the instrumentally determined parameters cannot be expected to be straightforward. The approach taken in this work is a simplification of the problem. It deals with print defects defined as local incorrectly transferred pieces of information that are due to assignable local causes. It is assumed that these print defects, measurable and predictable by technical means, deteriorate the visual quality experience (Saarelma and Oittinen 1993 (p. 357)) and hence the quality of the printed product can be enhanced by avoiding the defects. The intricate nature of quality experience is discussed in the following to motivate the probabilistic approach to the problem of predicting printability.

2.1.1 Subjective quality assessment

Print quality is high-dimensional and does not have absolute measures. Unanimous understanding of the number of dimensions relevant for print quality has not been reached, and may not be worth pursuing due to the strong context dependence of the experienced quality. According to a recent literature survey (Mangin and Dubé 2006), the most frequently occurring descriptors in print quality studies include various expressions of uniformity or unevenness, density, gloss, color properties, contrast and sharpness, and

specifically roughness when describing paper properties. While many of the listed properties can be characterized to some degree by technical measurements from printed images, Mangin and Dubé emphasize the importance of the subjective assessment of the print quality dimensions. The human perception of quality ultimately determines the customer requirements for the printed product.

To model the visual printed image quality, the subjective quality experience has been considered as a hierarchy of attributes of decreasing degree of abstractness (Oittinen et al. 2008). The five layers of the model consist of overall quality, interpretation based quality attributes, lower level perceptual attributes, instrumental quality measurements of the print, and instrumental measurements performed on the unprinted paper (Oittinen et al. 2008). The hierarchical construction is also supported by the work of I3A (International Imaging Industry Association) that deals with the conceptualization of human image quality experience of camera phones (I3A 2007). Subjective evaluation tests of various image contents can be planned so that the observers are asked to evaluate first the high-level overall quality and then the more specified (predefined) lower level quality attributes. Qualitative data on the lower level attributes can also be collected by interviewing each observer about the reasons for their quality ratings (Leisti et al. 2009).

Subjective quality evaluations in general can apply three techniques: paired comparison, rank ordering and scaling (Keelan 2002 (Chp 7)). In paired comparison, the observer is given two samples and he or she decides which one is better with respect to a given quality criterion. The technique is simple and allows very fine differences between the samples to be detected, but it gets very time consuming if the number of samples is large. Rank ordering means that the observer is asked to arrange the given series of samples into the order of preference. Scaling is an extended version of the ranking method, asking the observer to express the distances between the ordered samples along the quality dimension that is being tested. Techniques for assessing the rationality of the responses given by the group of observers, i.e., the jury, have been examined by Pulla (2007). These techniques are useful for inferring whether the jury provided useful information, or if the evaluation task was too complicated.

The problem remaining after collecting the subjective evaluation data and instrumental measurement results is to describe the dependences between the quality attributes – both within and between the abstraction levels – in a meaningful and efficient manner. Modeling the overall subjective quality experience is the ultimate goal. A bottom-up hierarchical approach is to utilize the knowledge of the operation of the human visual system, e.g., contrast sensitivity and luminance adaptation, to sum the contributions of individual low-level attributes (Eckert and Bradley 1998; To et al. 2008). A top-down approach constructs the understanding of the subjective quality experience by exploring which visual quality attributes are most commonly used by people in the quality evaluation test. The possibility of implementing the top-down quality model as a Bayes network (see Section 3.3) has been investigated (Oittinen et al. 2008; Eerola et al. 2010). In practice, studies found in the literature are usually constrained to describe the interrelationships within rather small subsets of quality attributes. The most common

approach is to construct regression models based on the parallel observations of attributes, for instance sharpness and clarity, or instrumentally and visually evaluated blurriness. Recently, a technique called cumulative match score (Phillips et al. 2000) has been successfully applied to prove that computational features of print quality, such as mottling index, color differences and edge raggedness, can predict similar quality ranking order as experienced by human observers (Eerola et al. 2008a and 2008b).

2.1.2 Technical quality

There exists no generally accepted or formulated way of measuring the overall printability. Although various equipment exist that are called printability testers (e.g., the Prüfbau Multipurpose Printability Tester and the IGT Printability Tester (Suontausta 1999)), none of them is able to cover the complex combination of paper properties, printing and the perception of print quality. Printability testers are laboratory equipment designed for studying the effects of certain printing variables in controlled conditions and they provide very limited possibilities to study runnability problems. Pilot-scale and production-scale printing tests are costly but enable testing conditions closer to commercial printing.

Typical indicators of printability include density, ink requirement, ink gloss, color range, mottling and print-through (Oittinen and Saarelma 1998). The list is not comprehensive. Density is calculated as (Oittinen and Saarelma 1998 (p. 197))

$$D = -\log_{10} R, \quad (1)$$

where R is the reflectance of the print, defined as the ratio of the intensities of the light reflected from the print (I_R) and light which would be reflected from an ideal diffuser (I_0): $R = I_R/I_0$ (Vaarasalo 1999 (p. 165)). For density calculation, the reflectance is normally measured using diffuse illumination in 45° angle of incidence and 0° detection angle relative to the surface normal (Oittinen and Saarelma 1998 (p. 197)). Gloss is measured in the TAPPI T 480 standard using specular illumination and detection in 75° angle relative to the surface normal (Vaarasalo 1999 (p. 164)). According to Leskelä (1998), international standards specify the measurement geometry, the spectral characteristics of the incident light, and the calibration of the instruments for reflectance measurements.

Print density is proportional to the thickness of the ink film on the paper at low and medium levels of ink film thickness, but when the ink film is thick enough to fully cover the paper surface, density levels off (Karttunen 1973; Tollenaar and Ernst 1969; Walker and Fetsko 1955). A one color print on a rough and matt surface cannot be darker than 1.4 density units (Karttunen 1973, Oittinen and Saarelma 1998 (p. 197)). Ink requirement describes the print density achieved with a given amount of ink on the paper. Print-through is the density of the reverse side of the paper, inversely related to opacity. The color gamut of the print is described by measuring the color coordinates, typically in the CIELAB color space (Vaarasalo 1999), from solid print patches and from the white paper. The volume bounded by connecting the coordinates in the 3-dimensional space indicates

the color gamut, as demonstrated for example in (Oittinen and Saarelma 1991). The three coordinates of the CIELAB color space are the luminance, L^* , and two chrominance coordinates, a^* and b^* . Non-uniform thickness of the ink film and penetration of the ink into the paper reduce print density and limit the color range (Oittinen and Saarelma 1998).

The unevenness of print density (or that of reflectance) in even areas of the image is often called noise. A noise parameter can be computed from an image of local density or reflectance variations as the coefficient of variation: $COV = \sigma/\mu$, where σ denotes the standard deviation and μ is the mean. The logarithm of the inverse of COV is the signal-to-noise ratio (SNR). For a more precise description of the nature of noise, it can be divided into three categories according to the characteristic wavelengths of the unevenness (Oittinen and Saarelma 1998 (p. 208)): (1) invisible scale at wavelengths smaller than $10\ \mu\text{m}$, (2) micro scale at wavelengths $10\ \mu\text{m} - 1\ \text{mm}$, and (3) macro scale at wavelengths larger than $1\ \text{mm}$. The categories reflect the origins of the noise. For instance, the microscopic roughness of the paper surface induces gloss variations at the invisible wavelength scale and affects the perceived mean gloss (Oittinen and Saarelma 1998). The maximum of the visual contrast sensitivity function is roughly in between the micro and macro scales (Kipphan 2001 (p. 90)) when viewing the target from a distance of $30\ \text{cm}$. Micro and macro scale noise is influenced by the properties of both the base paper and the coating particles. Speckles, when defined as missing gravure dots (Heintze 1982), or comparable low density areas of less than $1\ \text{mm}$ in size (MacGregor and Connors 1987), are an example of micro scale noise source. Linting and dusting (Ionides 1984), which mean the detaching of fiber and pigment particles from the paper surface, causes micro and macro scale noise to the print (Oittinen and Saarelma 1998). Mottling is low contrast macro scale noise that is typically associated with paper formation.

Image analysis has been increasingly applied to evaluate print quality. The large number of data points in the image enables repeatable objective results with high statistical confidence. As mentioned above, image analysis can be used to characterize mottling and other types of print unevenness (e.g., (Kajanto 1991; MacGregor and Connors 1987)). Automated image analysis facilitates the counting of missing halftone dots, which is a typical print quality problem in gravure printing (Vartiainen 2007). Various parameters can also be computed from images to examine the fine structure and shape of printed dots and lines (e.g., (Eerola et al. 2007; Eerola et al. 2008a)). Collected methods for characterizing the spectral content and orientation of textures in print and paper images have been presented by Nguyen and Jordan (1989).

2.2 Physical properties of paper

The stochastic process of paper forming has invoked the investigation of the structural properties in close connection with theoretical statistical models. One of the significant early treatments of the statistical geometry of paper was presented by Kallmes and Corte in the early 1960's. (Corte and Kallmes 1961a; Kallmes and Corte 1960; Kallmes et al. 1961). They presented the distributions of fundamental structural properties of two-

dimensional random fiber networks, such as the number of fiber crossings per unit area and per fiber, the free fiber lengths³, and the areas of polygons (holes) formed by the free fiber segments. They also discussed the challenges of extending the study to real sheets of paper that differ from ideal 2D structures by being three-dimensional and by having non-random fiber orientation and non-random spatial distribution of the fiber centers (Corte and Kallmes 1961a). Despite these idealizations, statistical geometry was found to provide satisfactory tools for describing the geometric arrangement of fibers and voids in paper (Corte and Kallmes 1961a). Moreover, the models developed for the ideal random fiber networks serve as references when analyzing the properties of real paper sheets (Sampson 2001a; Dodson and Sampson 2005).

The distribution of pore radii has been found approximately log-normal (Corte and Lloyd 1965) in multi-planar (MP) sheets that resemble handsheets (Corte and Kallmes 1961b). Although “fibres of normally formed sheets do not occur in specific layers as in MP sheets” (Corte and Kallmes 1961b (p. 357)), the log-normal form of pore size distribution seemed adequate and has been referred to ever since. Dodson and Sampson (1996) derived the pore size distributions through gamma-distributed free fiber lengths and found that the resulting distributions are very similar to the log-normal pore size distributions that assumed negative exponential distribution for the free fiber lengths (Corte and Lloyd 1965). The introduction of gamma distribution to the pore radius theory is motivated by the associated ability to model non-random, flocculated, fiber networks (Dodson and Sampson 1996). The standard deviation of pore radii is proportional to the mean pore radius (Corte and Lloyd 1965; Bliesner 1964) and the coefficient of variation of pore radii is insensitive to the basis weight and formation (Sampson 2001b). Similar observations have been made by Bloch and Rolland du Roscoat (2009) who also illustrate the curved porosity profiles in the thickness direction with various papers. The distribution of pore sizes in the thickness direction is well described by the negative exponential distribution (Bloch and Rolland du Roscoat 2009; Dodson 2001; Niskanen and Rajatoro 2002) which is a special case of gamma distribution. The pore heights have also been found to have a controlling influence on the measured pore size distribution (Sampson and Urquhart 2008).

The distribution of internal and surface pore sizes is relevant for the end use properties of paper. Calendering transforms the variations of uneven mass distribution into variations of other properties such as mass density, and may increase the variations in porosity while decreasing the average porosity and surface roughness (Kajanto 1991). The porosity variation affects ink transfer and contributes to mottling in offset printing (Engström 1994). Pores on the paper surface, when deep enough, prevent perfect contact with the ink film and thus obstruct the ink transfer. Gravure printing is particularly sensitive to paper roughness because ink transfer from the raster cup to the paper is only possible in direct contact. Offset print quality may also suffer from missing ink because the viscous ink cannot flow to the deep surface voids (Kajanto et al. 1998).

³ Free fiber lengths are the distances between crossings in a fiber network.

The most basic properties to describe paper for marketing and end use purposes are basis weight (mass per unit area of paper, g/m^2), moisture content, thickness, density and filler content (Levlin 1999). The measurement of each of these properties is standardized (Levlin 1999). To ensure good printability, the small-scale spatial variation of these properties should be minimized. The runnability of the paper in the printing press depends also on the strength properties, but they fall outside the scope of this thesis. The following presentation focuses on the characterization of the surface structure of paper.

Several techniques have been developed for describing the surface roughness of papers simply and efficiently. The most widely used devices for this purpose measure the air leakage between the paper surface and a measuring head, and provide a roughness or smoothness index to describe the result. Air-leak based measurements are fast, and the equipment is relatively inexpensive and straightforward to use (Barros 2006). Scanning profilometers and microscopy are typically slower than air-leak measurements but provide 3D presentations of surface topography, applicable for detailed quantitative analysis and visual inspection. Fast camera based imaging equipment can in some cases replace scanning. In addition to surface roughness, the compressibility of the paper surface is essential for printing as it affects the contact fraction of the paper with the printing cylinder. The compressive force of the printing nip is taken into account in variable ways in the air-leak based roughness measurements. There are also devices for measuring the contact smoothness under dynamic pressure conditions.

2.2.1 Air-leak testers

The Bekk tester⁴ (e.g., (Bichard 1992)) reports smoothness as the time required for a defined volume of air to flow between the paper surface and a flat annular reference surface under controlled pressure. A soft rubber pad supports the reverse side of the paper. Smooth papers make a tight contact with the rigid measuring head, which means that the time required for the air flow is long and the smoothness index is high.

Common air-leak based roughness testers include Bendtsen, Sheffield and Parker Print Surf a.k.a PPS⁵ (Parker 1971). They measure the rate of air flow between the paper surface and the measuring head. Rough surfaces allow relatively high flow rates and thus give high roughness readings. The development of roughness testers has pursued faster measurement, higher sensitivity to small surface depressions and less error due to air flow through the paper, by replacing the annular reference surface with a narrow edge – down to 51 μm in width in the PPS device. The PPS tester is also known for allowing clamping pressures comparable to those in a printing nip. On the other hand, it leaves marks on the paper surface (Barros 2006). A comparison of the four air-leak devices mentioned above can be found in (Bichard 1992) together with illustrations of the measuring principles.

⁴ Bekk: ISO 5627

⁵ Bendtsen: ISO 8791-2; Sheffield: ISO 8791-3; PPS: ISO 8791-4

Air-leak based testers are common in paper laboratories, largely due to being standardized. The smoothness and roughness indices have been widely applied to predict printability (Bristow and Ekman 1981; Heintze and Gordon 1979; Lyne 1976b; Mangin et al. 1993; Parker 1965). A quantity called printing roughness has also been derived based on theories of ink transfer, and this quantity has shown high correlation with the traditional roughness indices in specified printing conditions (Mangin and Geoffroy 1989). However, it is recognized that air-leak based methods have serious limitations. The same PPS roughness reading can be obtained by measuring papers of varying internal pore volume (Mangin et al. 1993), or by measuring papers that show varying degrees of print unevenness (Bristow and Ekman 1981). Air-leak based roughness readings are highly sensitive to large surface pores (Parker 1971). As stated by Bliesner already 40 years ago, “the results obtained with an air-leak instrument represent a gross average whereas smoothness in a printing sense represents local variations of a highly individual nature” (Bliesner 1970 (p. 1871)).

2.2.2 Topographical scanning and imaging

Compared to a single smoothness or roughness index, a considerably more precise description of the surface properties is the distribution of surface heights, or the distribution of surface void sizes (Bliesner 1970; Karttunen 1973; Lipshitz et al. 1990; Parker 1973). The early approaches to measure surface heights applied a mechanical stylus to literally sense the surface profile along a scanning line. Connections between printability and the profiles were established (Hendry 1961; Roehr 1955). Combining adjacent line profiles resulted in 3D topographical maps (Thomas 1982 (pp. 12-41)).

Optical profilometry and interferometry techniques provide non-contact alternatives to stylus profilometry. An autofocus laser profilometer scans the surface of the target by a laser light beam and records the movements of the detector lens system required to keep the light beam focused on the surface whose height varies from point to point. Another laser based technique applies triangulation geometry to compute the surface height from the position at which the reflected light beam hits the detector, but this provides coarser spatial resolution than the autofocus method (Kajanto et al. 1998 (p. 102)). Laser profilometry has been applied to paper surfaces by, e.g., Lipshitz et al. (1990), Wågberg and Johansson (1993), and Kuparinen (2008). An on-line applicable laser profilometry principle for monitoring of a running paper web has also been reported (Chase and Goss 1997). Interferometers are based on analyzing the fringe pattern detected when the sample light beam reflected from the sample surface has an optical path different from that of the reference light beam (Bruning et al. 1974). The sample and reference light beams are split from a common source. White light interferometry has been used to determine the surface topography of paper and printing plates (Preston 2009) but the method has been reported to require careful isolation from environmental vibrations and more reflective sample surfaces than laser profilometry requires (Stout and Blunt 1995).

Images of paper surface and bulk structure have also been acquired by various microscopy techniques. For example, confocal laser scanning microscope (CLSM) has been used to

detect surface topography changes caused by increasing clamping pressure (Mangin et al. 1993) and by successive calender runs (Moss et al. 1993). MacGregor et al. (1994) have aligned images of local small-scale gloss variation with 3D surface topography measurements acquired with CLSM from printed paper. Nanometer-scale pixel size is attainable with atomic force microscope (AFM) and scanning-electron microscope (SEM). They have been commonly applied to analyze the structure of paper coating layers (Preston 2009). An extensive review of microscopy in the analysis of printing papers has been recently published by Chinga-Carrasco (2009).

OptiTopo is a non-contacting instrument for acquiring surface topography images without the need for scanning. This fast method is based on a patented photometric stereo principle (Johansson and Hansson 2004). Using a camera and lights positioned in a grazing angle, images are first captured that present variation of gray scale values according to the shape of the surface and the illumination direction. The gradient of the target surface is proportional to the difference of the two images that have opposite illumination direction. The surface height at each point is computed from the gradient by integration in the Fourier domain. In addition to the surface topography map, the method produces the reflectance map from exactly the same area (Hansson and Johansson 2000). Figure 1 presents the principle with two lights opposite to each other, both forming an angle γ with the optical axis of the camera which is located right above the imaged

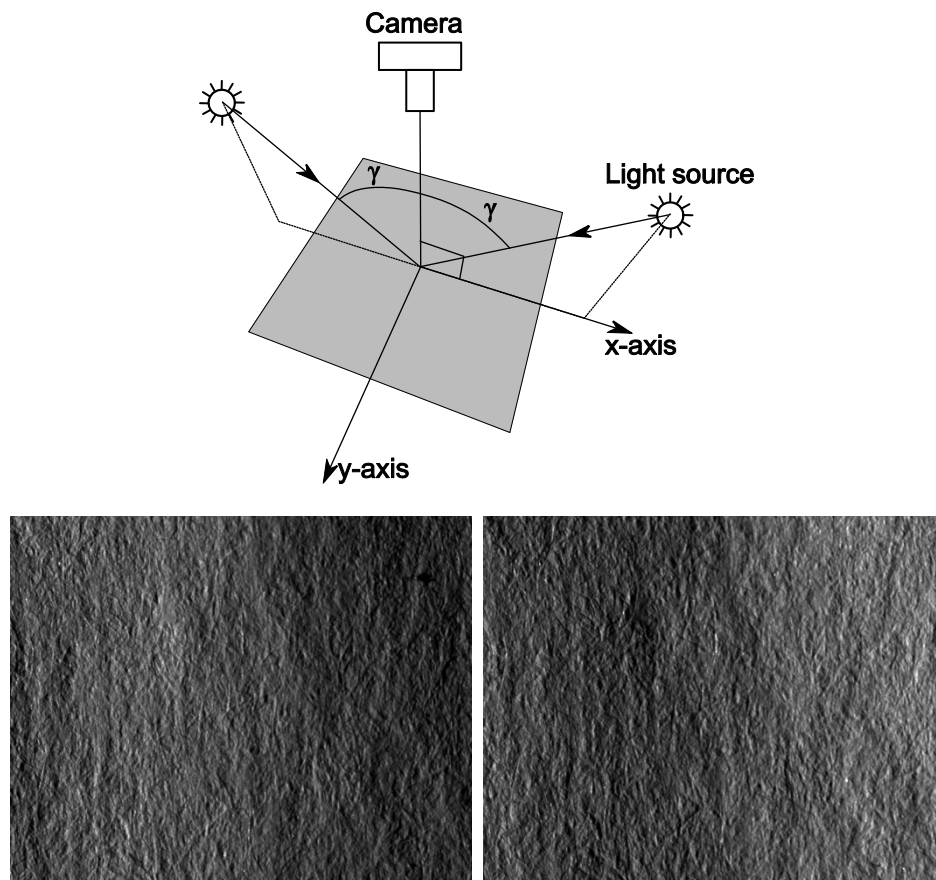


Figure 1. Illustration of the photometric stereo principle (top) and photographic images of a piece of SC paper illuminated from left and right at angle $\gamma = 76^\circ$ (bottom left and right, respectively). Figure provided by Mr. Matti Jukola.

sample. The images of a piece of SC paper illuminated with $\gamma = 76^\circ$ from left and right are shown at the bottom of Figure 1. Barros (2006) has applied the photometric stereo technique to acquire topography and reflectance images of printed paper and cardboard, and shown that depressions on the surface of the substrate explain uncovered areas (UCA), i.e., missing ink. The topography and reflectance maps analyzed in this dissertation have been acquired by a similar system, but using four instead of two light sources, thus largely resembling the commercial OptiTopo device.

The profile scans and 3D surface topography maps have been characterized by diverse methods. Many of the parameters have been developed within inspection of metal surfaces (Thomas 1982). Already the mechanically scanned line profiles of paper were characterized by the number and widths of surface depressions (Roehr 1955) and by time series modeling and spectral parameter computation (Kapoor et al. 1978). A micro roughness index was calculated from the line profile (Hendry 1961), conforming to one of the standardized parameters to describe roughness based on 3D profiles (Thomas 1982 (pp. 80-90)). 3D topography data can be processed into parameters that describe the amplitude and height distributions, the spatial properties, or the functional properties of the surface (Stout and Blunt 2000). Indices of the first category to describe paper surface properties include the root mean square (RMS) roughness, S_q , and the skewness and kurtosis of surface height distribution (Stout and Blunt 2000 (pp. 157-159)). The spatial properties of 3D surfaces can be characterized, for example, by the surface pit distribution (Kajanto et al. 1998 (p. 100)) or by the autocorrelation function (Järnström et al. 2008). The distribution of local relative areas and the distribution of the inclinations of the surface combine spatial and amplitude information and have been shown to explain the glossiness differences of papers (Chinga et al. 2007; Lipshitz et al. 1990; MacGregor et al. 1994). Roughness volume (MacGregor et al. 1994) is an example of a roughness index that describes also the functional properties of the surface, namely ink filling capability.

In the characterization of surface roughness, it is important to note that the computed parameter values are usually sensitive to the spatial and height resolution of the 3D profile, and the relevant size scales at which to compute the parameters depend on the application. Figure 2 exemplifies the sensitivity of the R_q roughness index, i.e. the RMS roughness of a line profile, to the wavelength range at which it is computed. Roughness can be divided into three categories (Kajanto et al. 1998 (p. 100)): (1) optical roughness at length scales below $1 \mu\text{m}$, (2) micro roughness at $1 \mu\text{m} - 100 \mu\text{m}$, and (3) macro roughness at $0.1 \text{ mm} - 1 \text{ mm}$. With reference to these categories, for instance, gloss depends mostly on the optical and micro roughness (Chinga et al. 2007; Kajanto et al. 1998; Lipshitz et al. 1990) whereas printing and coating properties are more closely related to macro roughness that originates from individual fibers and fiber bundles (Kajanto et al. 1998; Suontausta 1999).

The size scale considerations are essential also when the surface height distribution is of interest. Several studies support the theory of log-normally distributed depth and/or width of surface voids (Bliesner 1970; Hsu 1962; Parker 1973). An alternative approach is to

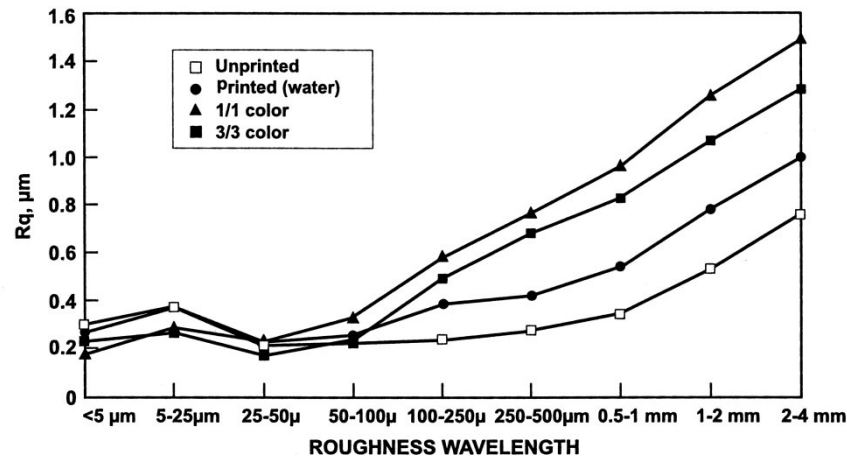


Figure 2. Roughness of LWC paper before and after printing in heatset offset (Suontausta 1999 (p. 201)). R_q is the standard deviation of surface heights that have been measured in this case with a laser profilometer and band-pass filtered into signals that present various wavelength ranges.

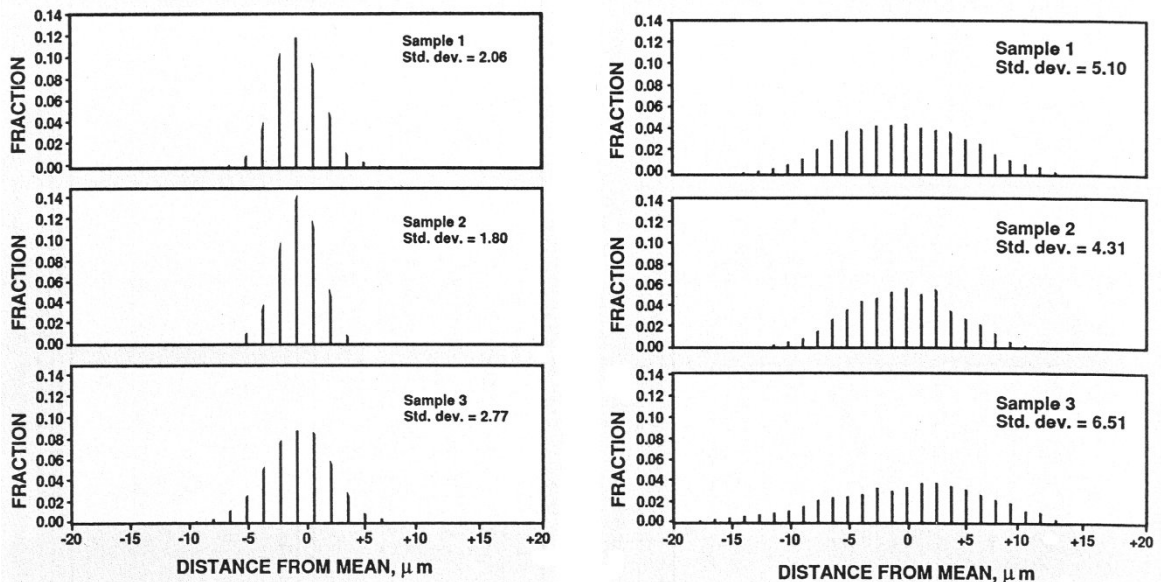


Figure 3. Distributions of surface heights measured from three coated paper samples with different spacing of adjacent measurement points. The coordinate data is “spaced $10.1 \mu\text{m}$ apart by columns and $20 \mu\text{m}$ apart by rows” (left), or “ $1.3 \mu\text{m}$ apart by columns and $2.5 \mu\text{m}$ apart by rows” (right) (Lipshitz et al. 1990).

assume that the height of the surface profile with respect to its mean is normally distributed (Heikkilä 1997), but this seems to be the case mainly with the microstructure of coated paper surfaces (Gate et al. 1973; Lipshitz et al. 1990). Lipshitz et al. (1990) have demonstrated how the spatial resolution of surface topography measurement alters the shape of the distribution of topography values. Results from their experiments are exemplified in Figure 3. In the topography measurements presented and analyzed in this dissertation, one pixel typically represents a local area of $10 \times 10 \mu\text{m}^2$, and the distribution of the surface height values around the mean level resembles the distributions on the left hand side of Figure 3. This resolution has been chosen because it is expected to be relevant to the small-scale print defects.

2.2.3 Contact area measurements

Apart from electronic printing (inkjet and electrophotography), the transfer of ink to the paper involves mechanical contact under pressure, and hence the measurement of contact area has been investigated alongside with the development of surface topography characterization. Several techniques for measuring the contact area have been proposed. The Chapman principle (see, e.g., (Kajanto et al. 1998 (p. 103))) and its application in the Fogra-Kam (Kontakt Anteils Messung) method and are most commonly referred to. The idea is to deduce the optical contact of the paper surface with a glass prism by measuring the intensity of the light reflected from the glass. In the points and areas where the paper is not in contact with the prism, the incident light is reflected away from the detector which is thus seeing darkness. In areas of contact between the paper and the glass, the intensity of light reflected to the detector depends on the fraction of optical contact in that area. According to (Kajanto et al. 1998), this measuring principle is sensitive to the macro roughness of paper.

Criticizing the static nature of the compression in the Chapman instrument, Bliesner (1970) developed a dynamic smoothness tester that measures contact smoothness and compressibility under conditions approximating to those in the printing nip. In his system, smoothness parameters are computed from the contact area photographs taken with a xenon flash. Bliesner has shown that the sizes of the local contact areas are approximately log-normally distributed. Another development of the Chapman principle has been presented in (Blokhuis and Kalff 1976) where a laser beam scans the contact point of the paper and a rolling glass cylinder. Lyne (1976a) has applied a similar instrument and characterized the roughness under pressure as the variance distribution of surface void sizes.

In measurements of dynamic contact smoothness based on digital imaging, the contact area is detected from the signal of a CCD (charge-coupled device) camera. Examples of such implementations are the Pira printing smoothness tester (Safadi 1992) and the equipment of Heikkilä et al. (1994) that also utilizes the rolling transparent cylinder. Preston et al. (2008) characterize the dynamic contact of paper and printing cylinder by attaching a carbon paper to the white paper under examination, running them through the printing nip and scanning the set-off pattern produced on the paper by the carbon copy paper ink. The Print Simulation Tester of Rycobel Group is an example of a laboratory tester that deduces the contact areas under dynamic pressure by image analysis and thus “detects” missing dots without printing (Rycobel Group 2010).

2.3 Literature on the dependence between print quality and paper surface properties

Spots of missing ink can be visually disturbing print defects, particularly when occurring in image areas that are supposed to be uniform. Even if the missing ink spots are small

enough to correspond to micro scale⁶ noise, they cause print unevenness that is visually “recognized as not belonging to the image” and considered to have a large influence on the perceived print quality (Saarelma and Oittinen 1993 (p. 357)). Depending on the paper and printing conditions, the reason for the local absence of ink may be attributable to imperfect contact in the printing nip, to unfavorable chemical conditions, or even to a surface strength problem that leads to the disintegration of the printed paper surface (linting; typically encountered in offset printing). This section summarizes the previous work relevant to the study of print unevenness that originates from missing ink or inadequate ink coverage. The main focus is on the relationship between small-scale print density variations and the topography of paper surface. Two other important properties of paper affecting printability, namely formation and compressibility, are briefly discussed.

Barros (2006) has analyzed the occurrence of uncovered areas (UCA) of print in flexography. His study applies methods similar to those in this thesis, the most prominent being surface topography measurement with photometric stereo, combined with simultaneous print reflectance measurement, and the point-wise analysis of the aligned image data. Barros has analyzed solid print areas of cardboard samples printed in laboratory conditions. He has tested various principles of thresholding the topography map in order to maximize the coincidence of the thresholded topography map with the binary map of UCA (Barros and Johansson 2006). Both topography and reflectance maps are obtained from printed samples. Approximately 50 % of the UCA points coincide with topography depressions, and the wavelengths of the topography map most relevant for the prediction have been reported to be from 0.15 mm to 0.75 mm (Barros et al. 2005; Barros and Johansson 2006). UCA analysis has also been reported in (Mesic et al. 2006).

Another print quality case applying aligned image data and binary feature maps derived from the measured 2D property maps has been presented by MacGregor and colleagues. They have acquired a topography map of an offset printed supercalendered LWC (light weight coated) paper sample with CLSM and registered it with a small-scale gloss image captured with a CCD camera from the same area (MacGregor et al. 1994). The topography map of pixel size of approximately $2.5 \mu\text{m} \times 2.5 \mu\text{m}$ has been processed into a facet angle map that describes the local inclinations of the paper surface. The relationship between gloss and facet angle has been quantified by evaluating the coincidence of thresholded binary images, resembling the approach of Barros described above. As much as 75 % of local areas of approximately “flat” surface have been found to coincide with local areas of high print gloss (MacGregor et al. 1994). This analysis principle has been named earlier as “feature correlation” by MacGregor and Johansson and applied to LWC paper samples (MacGregor and Johansson 1990 and 1991). The registered image stack consists of various measurements of, e.g., gloss, light transmittance and mass distribution. The experiments have indicated, for example, that areas of high gloss often coincidence with areas of high local amount of coating (MacGregor and Johansson 1990 and 1991).

Several studies have been published about the influence of surface topography and compressibility on missing dots in gravure. In (Heintze and Gordon 1979; Heintze 1982),

⁶ In (Saarelma and Oittinen 1993) micro scale is defined as wavelengths from 10 μm to 100 μm .

surface roughness has been characterized by air-leak based indices and speckle has been expressed as the number of missing dots in a defined area. PPS roughness has been found to explain only one third of speckle, and thus the majority of the print density variations have been interpreted to be due to variations of printing press conditions. Bristow and Ekman (1981) have emphasized the role of paper compressibility in predicting gravure print quality while confining themselves to characterizing the paper by PPS measurement. Mangin et al. (1993) have studied missing dots in connection with the topography and compressibility of uncalendered papers. They have constructed a series of 3D topography presentations from CLSM images taken under increasing compression. Roughness and static compressibility indices have been derived through the analysis of the topography maps. Missing gravure dots have also been counted, and a deterministic relation has been proposed between the printing pressure and the number of missing dots. Hirn et al. (2009) have applied multiple linear regression to stacks of six point-wise aligned property maps in order to explain the local density variations of gravure printed samples by five paper properties. Using a modeling resolution of $250 \times 250 \mu\text{m}^2$ per pixel, the study has identified local mass density (acquired by beta radiography) and local ink penetration as the major factors affecting the local print density, while surface topography alone has been found to explain less than 20 % of the print density variation.

Kajanto (1991) has applied image based analysis and point-wise correlations to assess the factors that induce larger scale print unevenness, i.e., mottle, within offset printing. 2D maps of print reflectance and local mass density have been registered, and the variation of mass density has been shown to explain a maximum of 28 % of the variation in print reflectance with woodfree offset papers (Kajanto 1989). The dependence decreases by increasing print density. Dickson (2006) has also presented image based analysis of newsprint printed with a laboratory scale offset printing unit. He has captured and registered maps of surface topography, mass density and solid print coverage with a pixel size of approximately $40 \times 40 \mu\text{m}^2$. He has then computed the point-wise correlation between the measured properties in local regions of size 0.16 mm^2 . According to the results, local print density can be slightly better explained by local mass density than by surface topography (approximately 20 % vs. 9 % of the variation in the local print density is explained), but the latter will be increasingly important when the print quality is high. Studies focused specifically on small scale print defects in offset have not been found.

The observations that print density and its variation affect the dependence measures, as described above, are related to the general theory of ink transfer. Several analytical models have been proposed to express the amount of ink transferred to the paper as a function of the amount of ink on the printing plate. Parameters describing the smoothness of the paper and the immobilization and splitting of the ink are estimated from data gathered from test printing. Foundations of the ink transfer theory have been laid 50-60 year ago (Walker and Fetsko 1955; Ichikawa et al. 1962), and notable reviews of their development have been given by Karttunen (1973) and Mangin et al. (1982). When predicting the occurrence of incomplete ink transfer based on surface topography measurement, the key point to recognize is that ink transfer depends strongly on the thickness of the ink film on the plate, particularly when this thickness is small (Karttunen

1973; Walker and Fetsko 1955). This explains the increased dependence between print unevenness and paper properties (formation, topography, compressibility) with decreasing print density. The weak point of ink transfer theory is that it deals with parameters that describe the average properties of the paper and are thus not suited for local analysis (Barros 2006 (p. 43)).

3 Methods for quantifying statistical dependence

One of the main objectives in this work is to evaluate the statistical dependence between print density and paper properties. The starting point for the analysis is a large set of multivariate data acquired by image based measurements. This chapter describes the methodology for assessing the statistical dependence: general principles of probability density estimation, statistical analysis and probabilistic inference. Precise descriptions of the procedures applied to the print quality data will be given in Chapter 4.

Throughout this work, random variables are denoted with upper case letters and the values they take with corresponding lower case letters. Boldface symbols denote vectors and matrices. Having observations of random variables X and Y as (x, y) pairs, the most straightforward and widely used method for describing the dependence between the variables is to estimate the correlation coefficient (a.k.a. Pearson correlation) from the observations (Draper and Smith 1998 (p. 40)). It measures linear dependence but cannot describe non-linear relationships. An example is given in Figure 4 where two sets of 1000 (x, y) pairs are presented as scatter plots. On the left hand side of Figure 4, X and Y are linearly correlated, but on the right hand side they are not, and this is reflected in the corresponding correlation coefficients, ρ . However, the variables on the right hand side of Figure 4 are not statistically independent of each other; they clearly exhibit non-linear interdependence. In fact, mutual information (MI; a statistical dependence measure to be discussed in Section 3.2) between X and Y is equal in both subfigures. Although the

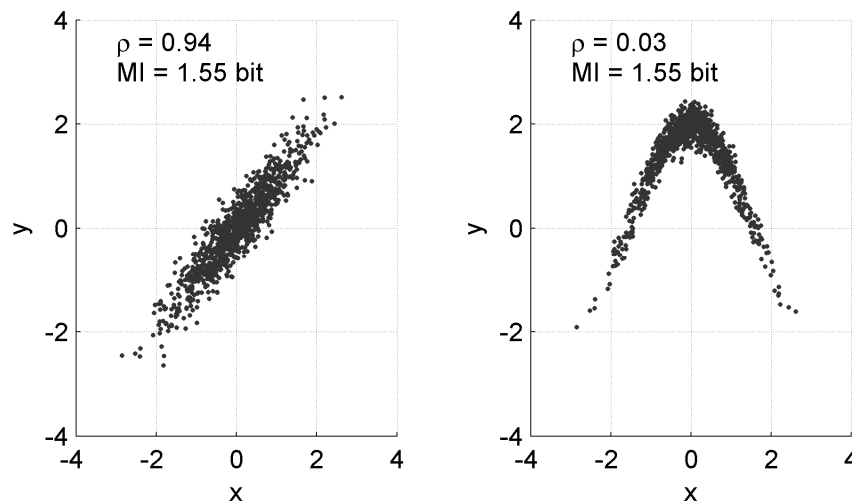


Figure 4. Examples of linear (left) and non-linear (right) dependence.

example is extreme and rarely confronted with measurement data, it demonstrates the need for more versatile ways of describing statistical dependence than linear correlation. In a monotonic but nonlinear case, for instance, rank correlation measures such as Spearman's rank correlation coefficient (Stuart et al. 1999 (p. 488)) and Kendall's tau (Kendall 1938) describe the association between random variables better than Pearson correlation. Rank correlation measures are not based on the pure data observations but on the rank information of the observations, ordered according to their magnitude.

Considering the stochastic structure of paper and the local random processes involved in the application of printing ink to the paper, it is reasonable to expect that there are no deterministic point-to-point relationships between local print density and the local structural properties of paper, such as surface height. Instead, the relationships are probabilistic and thus they are appropriately described with the full joint probability density functions (pdfs) of the measured properties (see, e.g., (Papoulis 1990)). Probability density estimation is essential for various applications including data modeling, pattern recognition and probabilistic inference, and constitutes a research area in itself (e.g., (Scott 1992; Bishop 2006 (Chp 2); McLachlan and Peel 2000)), but this thesis is limited to the basics of the topic. Section 3.1 describes three methods for estimating the probability distribution from observed multivariate data and discusses their benefits and drawbacks. Section 3.2 concentrates on the evaluation of the information carried by the pdf estimate, including means of quantifying the dependence. Correlation coefficient will show up as a special case of the general expression of dependence. Section 3.3 introduces the Bayes network as a model for describing and utilizing probabilistic dependences when there are many stochastic variables to be analyzed simultaneously. In case of print quality analysis, the model combines instrumentally measured and subjectively assessed quality attributes.

3.1 Probability density

Probability density estimation infers, given the measurement data, about a model for the distribution that the observed values are originating from. A fast and simple approach is to construct a histogram of the observed values. Histogram is typically classified as a non-parametric density estimation method in that the form of the distribution estimate does not depend on a specified analytical model but rather on the size of the data set (Bishop 2006 (p. 68)). In contrast, parametric density estimation involves an assumption of the form of the distribution, typically presentable by a few parameters that are identified from the data. Subsection 3.1.1 briefly introduces two non-parametric density estimation methods: the histogram and its advanced version, the kernel approach. Subsection 3.1.2 deals with parametric density estimation, concentrating on the Gaussian mixture model (GMM) (Bishop 2006 (pp. 110-113 and 430-439); Nabney 2002) which is a versatile parametric approach to cases in which a justifiable assumption about the form of the distribution cannot be made. It is noteworthy that both the non-parametric and parametric density estimates are approximations, and the true probability distribution that generated the observed data remains unknown regardless of the selected estimation method.

3.1.1 Histogram and kernel density estimates

The histogram approximation of the joint probability density of the d -dimensional variable \mathbf{X} divides the range of each variable in the d -dimensional space into bins of width \mathbf{h} and counts the number of observations falling into each bin. Normalizing the counts by the bin width and by the number of data points, N , produces the probability density estimate. The bins are typically chosen to have the same width in a given dimension.

Histograms are straightforward to construct and serve as quick visualization tools for data in one or two dimensions. On the other hand, the histogram approach involves severe problems (Bishop 2006 (p. 121); Härdle and Simar 2007 (p. 13)). First, the bin width, \mathbf{h} , controls the shape of the histogram. Too wide bins smooth the density estimate so that important details of the shape of the probability density may be lost. Too narrow bins result in a very variable estimate with spurious peaks and increased uncertainty about the probability density. For d -dimensional data that is assumed to follow a multivariate Gaussian distribution, an optimal bin width in the j th dimension is $h_{\text{opt}} = 3.5N^{-1/(2+d)}s_j$ (Martinez and Martinez 2008 (p. 311)), where s_j denotes the sample standard deviation in the j th dimension. However, the locations of the bins also have an influence on the shape of the histogram (Härdle and Simar 2007 (pp. 11-12)). Second, the usability of the histogram is limited by the fact that the number of bins scales exponentially with the dimensionality; if each of the d dimensions is divided into M bins, the total number of bins in the histogram is M^d . Increasing the dimensionality of the data space thus leads to a rapidly increasing demand for data to get meaningful density estimates. Third, the bin edges cause discontinuities in the probability density estimate. Finally, information is lost when the observations are replaced by the center locations of the histogram bins.

Kernel density estimation can circumvent the two last-mentioned problems of histograms. In this method, a kernel function, also called a *Parzen window*, is evaluated at each data point, which specifies the contribution of the data point. The contributions are added together, and the result is normalized by N to produce the probability density estimate (Bishop 2006 (p. 123)). There are several options for the kernel function, varying from a uniform hypercube to smooth Gaussian kernel, see, e.g., (Martinez and Martinez 2008 (p. 327)). They produce different shapes of the estimated density, but the key parameter determining the shape is the bandwidth of the kernel function. The effect of the bandwidth is similar to that of the width of the histogram bin: too large values cause over-smoothing and too small values generate noisy density estimates. A normal reference rule for the bandwidth of the Gaussian kernel in the j th dimension is $h_G = (4/(N(d+2)))^{-1/(4+d)}s_j$, where s_j again denotes the sample standard deviation (Martinez and Martinez 2008 (p. 328)). With increasing number of data points, the kernel density estimator converges to the true probability density (Bishop 2006 (p. 123)). However, while not losing information, the kernel density estimate is inefficient in that it requires the entire data set to be stored.

3.1.2 Gaussian mixture model

A parametric probability density estimate can condense large amounts of observed data into a small set of parameters. The two main issues to solve in the parametric approach are the choice of the functional form of the model and the identification of the parameters from the data. The Gaussian distribution is often selected as the model, which in many cases can be justified by the central limit theorem (e.g., (Haigh 2002 (p. 105))). Furthermore, of all distributions with the same variance, Gaussian distribution has the largest entropy (e.g., (Cover and Thomas 1991 (p. 234))), which means that the Gaussian model makes the fewest presumptions about the form of the probability density. Obviously prior knowledge of the source or nature of the data may support the selection of a parametric model other than Gaussian. Parameters are typically identified with the maximum likelihood (ML) method (Kay 1993 (pp. 157-217)) which estimates the distribution parameters with those maximizing the likelihood of the observed data. Thus ML estimation is an optimization problem. The ML estimates of the distribution parameters have closed form expressions in the case of Gaussian model (Seber 1984 (pp. 59-61)), but in general the optimization problem must be solved numerically.

A basic parametric density model, such as a single Gaussian, is restricted by its functional form and may not be well adaptable to the observed data. Furthermore, selecting the appropriate form of model with little prior knowledge of the source distribution is difficult. A mixture distribution model (McLachlan and Peel 2000), i.e., a linear combination of basic distributions, may then be an appropriate choice. GMM is a linear combination of Gaussian distributions (Bishop 2006 (pp. 110-113 and 430-439); Nabney 2002). It is an attractive choice for a density model due to its simple and efficient formulation. GMM approximates the probability density function of a d -dimensional random variable \mathbf{X} as:

$$\begin{aligned} f(\mathbf{x}|\boldsymbol{\theta}) &= \sum_{i=1}^k c_i \mathcal{N}(\mathbf{x}|\boldsymbol{\mu}_i, \mathbf{C}_i) \\ &= \sum_{i=1}^k c_i (2\pi)^{-d/2} (\det(\mathbf{C}_i))^{-1/2} \exp\left[-\frac{1}{2}(\mathbf{x} - \boldsymbol{\mu}_i)^T \mathbf{C}_i^{-1}(\mathbf{x} - \boldsymbol{\mu}_i)\right], \end{aligned} \quad (2)$$

where $\boldsymbol{\theta}$ is the complete set of parameters specifying the model. Each Gaussian component, $\mathcal{N}(\mathbf{x}|\boldsymbol{\mu}_i, \mathbf{C}_i)$, is parameterized by its mean (vector), $\boldsymbol{\mu}_i$, and covariance matrix, \mathbf{C}_i . The total number of Gaussian components in the model is k , and the weight of the i th Gaussian is c_i . The weights are also called priors and their sum must equal to one for normalization. With sufficiently high number of component distributions, GMM can in principle describe any continuous distribution (Bishop 2006 (p. 111)). However, the number of components, k , directly affects the number of parameters, $K(k)$, needed to specify a GMM in d -dimensional space: $K(k) = (k-1) + k(d + d(d+1)/2)$. An increasing number of components leads to a more complicated model and may result in over-fitting problems, such as the ‘‘collapsing’’ of a Gaussian component onto a single data point.

The ML estimates of the parameters, $\hat{\boldsymbol{\theta}} = (\hat{c}_1, \dots, \hat{c}_{k-1}, \hat{\boldsymbol{\mu}}_1, \dots, \hat{\boldsymbol{\mu}}_k, \hat{\mathbf{C}}_1, \dots, \hat{\mathbf{C}}_k)$ of GMM cannot be solved analytically. The GMM ML problem reads as:

$$\begin{aligned}\hat{\boldsymbol{\theta}} &= \operatorname{argmax}_{\boldsymbol{\theta}}\{L(\{\mathbf{x}_1, \dots, \mathbf{x}_N\}|\boldsymbol{\theta})\} = \operatorname{argmax}_{\boldsymbol{\theta}}\{\log \prod_{j=1}^N f(\mathbf{x}_j|\boldsymbol{\theta})\} \\ &= \operatorname{argmax}_{\boldsymbol{\theta}}\{\sum_{j=1}^N \log \sum_{i=1}^k c_i \mathcal{N}(\mathbf{x}_j|\boldsymbol{\mu}_i, \mathbf{C}_i)\}\end{aligned}\quad (3)$$

where $\{\mathbf{x}_1, \dots, \mathbf{x}_N\}$ is the set of observed data and $L(\{\mathbf{x}_1, \dots, \mathbf{x}_N\}|\boldsymbol{\theta})$ is the log likelihood of the data given the model parameters. The GMM parameters are estimated by the iterative expectation maximization (EM) algorithm with strong convergence properties (Dempster et al. 1977). The model parameters c_i , $\boldsymbol{\mu}_i$, and \mathbf{C}_i are first initialized, and the EM algorithm then updates the parameter estimates by alternating the E step and M step described below (Bishop 2006 (p. 438)). The iterations are terminated when a convergence criterion is met. Initialization and convergence will be discussed later in this section.

E step. Responsibility, w_{ij} , of the i th component in generating the j th observation:

$$w_{ij} = \frac{c_i \mathcal{N}(\mathbf{x}_j|\boldsymbol{\mu}_i, \mathbf{C}_i)}{\sum_{m=1}^k c_m \mathcal{N}(\mathbf{x}_j|\boldsymbol{\mu}_m, \mathbf{C}_m)} \quad (4)$$

M step. Re-estimating the parameters using the current responsibilities:

$$\boldsymbol{\mu}_i^{\text{new}} = \left(\sum_{j=1}^N w_{ij}\right)^{-1} \sum_{j=1}^N w_{ij} \mathbf{x}_j \quad (5)$$

$$\mathbf{C}_i^{\text{new}} = \left(\sum_{j=1}^N w_{ij}\right)^{-1} \sum_{j=1}^N w_{ij} (\mathbf{x}_j - \boldsymbol{\mu}_i^{\text{new}}) (\mathbf{x}_j - \boldsymbol{\mu}_i^{\text{new}})^T \quad (6)$$

$$c_i^{\text{new}} = \frac{1}{N} \sum_{j=1}^N w_{ij} \quad (7)$$

The log likelihood function also determines the uncertainty of the parameter estimates. The covariance matrix of the parameter estimates is obtained – asymptotically and under “regularity” conditions – through the likelihood as follows (Kay 1993 (p. 167); Bishop 2006 (pp. 213-215); Roberts et al. 1998). By the definition of the ML estimate of the parameters, the first derivative of log likelihood function vanishes at $\hat{\boldsymbol{\theta}}$. Assuming the log likelihood (shortened to $L(\boldsymbol{\theta})$ in the following) narrowly peaked around $\hat{\boldsymbol{\theta}}$, it can be approximated by Taylor expansion up to the second order term:

$$\begin{aligned}L(\boldsymbol{\theta}) &\approx L(\hat{\boldsymbol{\theta}}) + (\boldsymbol{\theta} - \hat{\boldsymbol{\theta}}) \left. \frac{\partial L(\boldsymbol{\theta})}{\partial \boldsymbol{\theta}} \right|_{\boldsymbol{\theta}=\hat{\boldsymbol{\theta}}} + \frac{1}{2} (\boldsymbol{\theta} - \hat{\boldsymbol{\theta}})^T \left. \frac{\partial^2 L(\boldsymbol{\theta})}{\partial \boldsymbol{\theta}^2} \right|_{\boldsymbol{\theta}=\hat{\boldsymbol{\theta}}} (\boldsymbol{\theta} - \hat{\boldsymbol{\theta}}) + o\left((\boldsymbol{\theta} - \hat{\boldsymbol{\theta}})^3\right) \\ &\approx L(\hat{\boldsymbol{\theta}}) - \frac{1}{2} (\boldsymbol{\theta} - \hat{\boldsymbol{\theta}})^T \mathbf{A} (\boldsymbol{\theta} - \hat{\boldsymbol{\theta}}).\end{aligned}\quad (8)$$

The matrix \mathbf{A} is the negative Hessian (the second derivative with respect to the parameters) of the log likelihood function evaluated at the estimate $\hat{\boldsymbol{\theta}}$ (McLachlan and Peel 2000 (p. 42)). Taking exponential function of both sides of Eq. (8) shows that, in this approximation, the parameters have a Gaussian distribution with covariance matrix equal to the inverse of \mathbf{A} . McLachlan and Peel (2000) remind that the sample size has to be “very large” for the covariance matrix approximation to be valid. Furthermore, the covariance matrix is often tedious to calculate analytically. Hence numerical methods are often applied, namely Markov chain Monte Carlo (MCMC) sampling (Richardson and Green 1997) and bootstrapping (McLachlan and Peel 2000 (p. 68)). The large number of

independently measured data points in the multivariate images provides a strong basis for probability density estimation and statistical inference.

The number of components, k , suitable for modeling the unknown pdf by a finite mixture model cannot be determined from the ML criterion (Eq. (3)) because the likelihood is a non-decreasing function of k (Figueiredo and Jain 2002). Several criteria have been proposed to estimate the appropriate number of components. McLachlan and Peel review the criteria from the clustering point of view (McLachlan and Peel 2000 (Chp 6)), and Figueiredo and Jain (2002) briefly discuss the criteria in the context of finite mixture models. The general idea in the various criteria is to maximize an expression of log likelihood while penalizing for increasing k . A typical procedure for determining a suitable value for k is to form several density estimates with a range of values of k , and to choose as the final estimate the model that optimizes the selected criterion (e.g., (Roberts et al. 1998)).

Estimating several versions of the probability density model with the same data, and selecting the final model based on the results, is also important to circumvent the inherent problem of the EM algorithm that it may converge to a local maximum of the likelihood function instead of the global maximum. The initialization of the parameters of the mixture model has a significant impact on the outcome of the basic EM algorithm (Dempster et al. 1977; McLachlan and Peel 2000). According to Figueiredo et al. (1999), the mean vectors of GMM can be initialized as uniformly distributed over the range of the data values, or chosen randomly among the data points when the dimensionality of the data is low (4 variables or less in their work) (Figueiredo and Jain 2002). The initial covariance matrices are made proportional to the identity matrix, $\hat{\mathbf{C}}_i = \sigma^2 \mathbf{I}_d$, where σ^2 is a fraction, e.g., 1/10, of the mean of the variances along each dimension of the data (Figueiredo and Jain 2002). For higher dimensional data Figueiredo et al. (1999) suggest to initialize the GMM with the K-means clustering algorithm. On the other hand, the component-wise EM algorithm proposed in (Figueiredo and Jain 2002) is reported to be quite insensitive to the initialization as long as the initial number of GMM components is high enough to spread the components throughout the data space (see (Figueiredo and Jain 2002) for details). The main idea in this method is to start with the user-specified maximum number of components and to let those components die during the EM iterations whose weight, c_i , goes to zero. When this happens, the probability mass of the annihilated component is redistributed to the remaining GMM components. This is also the version of the EM algorithm applied in this thesis.

Probability density estimates are needed in this work for characterizing the dependences between print quality and the surface topography of paper. GMM is an attractive choice for this purpose for three reasons. Firstly, the joint pdf of the measured properties has an unknown form that is clearly not Gaussian. Secondly, GMM is a very compact representation of the large amount of data. Thirdly, the parametric representation enables the analytical calculation of conditional pdfs of individual variables. The drawback of GMM is that due to the parametric presentation, it may lose some details that are present in the original data, such as a detailed shape of the tail of a distribution. The histogram can

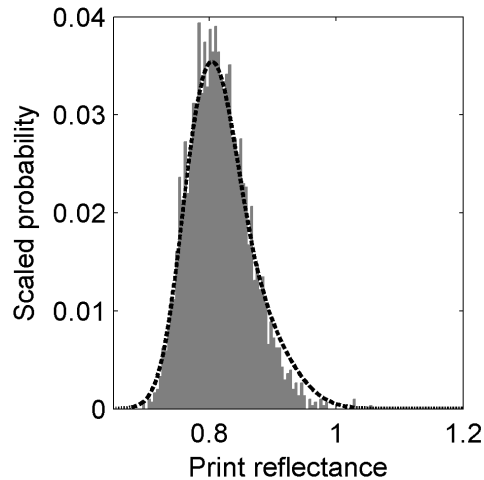


Figure 5. Example of the conditional distribution of print reflectance given that surface height is $-3 \mu\text{m}$. The histogram is presented by the gray bars and the GMM estimate as dashed line. The GMM contains 4 components.

better preserve the fine details in the tails and therefore histograms are occasionally resorted to, for instance in visualizations. Figure 5 gives an example of a 1D density estimate, presented by both histogram and GMM.

3.2 Characterization of statistical dependence

Both parametric and non-parametric probability density estimates provide several possibilities to assess the dependence between the variables. A practical and well advised method is to first visualize the estimated probability density to gain insight into the multivariate data and dependences therein. A density estimate also readily provides regression estimates and their uncertainty without making assumptions about the linear or non-linear nature of the regression dependence. The main emphasis of this section is on quantifying the dependences by the generic statistical measure called *mutual information* (MI). The determination of MI from the density estimate is presented and its interpretation and applications are briefly discussed.

For the purposes of this section, the probability density functions are formulated according to (Papoulis 1990 (pp. 136-179)). The general form of the joint probability density function of random variables (vectors) \mathbf{X} and \mathbf{Y} is written as

$$f(\mathbf{x}, \mathbf{y}) \, d\mathbf{x} \, d\mathbf{y} = P(\mathbf{x} < \mathbf{X} \leq \mathbf{x} + d\mathbf{x}, \mathbf{y} < \mathbf{Y} \leq \mathbf{y} + d\mathbf{y}), \quad (9)$$

where P denotes probability. Correspondingly, the conditional pdf of random variable \mathbf{Y} given \mathbf{x} is

$$f(\mathbf{y}|\mathbf{x}) \, d\mathbf{y} = P(\mathbf{y} < \mathbf{Y} \leq \mathbf{y} + d\mathbf{y} | \mathbf{X} = \mathbf{x}). \quad (10)$$

The regression describes the expected value of \mathbf{Y} according to this conditional density, thus it is a function of \mathbf{x} :

$$\boldsymbol{\mu}_Y(\mathbf{x}) = E\{\mathbf{Y}|\mathbf{x}\} = \int_{-\infty}^{\infty} \mathbf{y}f(\mathbf{y}|\mathbf{x}) \mathbf{d}\mathbf{y}. \quad (11)$$

The variance of the regression estimate, assuming that the parameters of the pdf are known exactly, is

$$\sigma_Y^2(\mathbf{x}) = E\left\{(\mathbf{Y} - \boldsymbol{\mu}_Y(\mathbf{x}))(\mathbf{Y} - \boldsymbol{\mu}_Y(\mathbf{x}))^T \middle| \mathbf{x}\right\} = \int_{-\infty}^{\infty} \mathbf{y}\mathbf{y}^T f(\mathbf{y}|\mathbf{x}) \mathbf{d}\mathbf{y} - \boldsymbol{\mu}_Y^2(\mathbf{x}). \quad (12)$$

The general definition of Eq. (11) does not specify whether the regression dependence is linear or non-linear, and it is applicable to all kinds of density estimates. The familiar expression, in which the regression of \mathbf{Y} is a linear function of \mathbf{x} , results if the joint probability density of \mathbf{X} and \mathbf{Y} is a multivariate Gaussian distribution. A thorough practical description of linear regression is given, e.g., in (Draper and Smith 1998). Regression is computed from GMM as:

$$\hat{\mathbf{y}}^{(regr)}(\mathbf{x}) = \sum_{i=1}^k c_i \alpha_i(\mathbf{x}) \left[\boldsymbol{\mu}_i^{(y)} + \mathbf{C}_i^{(yx)} (\mathbf{C}_i^{(xx)})^{-1} (\mathbf{x} - \boldsymbol{\mu}_i^{(x)}) \right], \quad (13)$$

where the expectation and covariance matrix of each GMM component have been partitioned as:

$$\boldsymbol{\mu}_i = \begin{bmatrix} \boldsymbol{\mu}_i^{(y)} \\ \boldsymbol{\mu}_i^{(x)} \end{bmatrix}, \quad \mathbf{C}_i = \begin{bmatrix} \mathbf{C}_i^{(yy)} & \mathbf{C}_i^{(yx)} \\ \mathbf{C}_i^{(xy)} & \mathbf{C}_i^{(xx)} \end{bmatrix}, \quad (14)$$

and the auxiliary term is

$$\alpha_i(\mathbf{x}) = \frac{\det(\mathbf{C}_i^{(xx)})^{-1/2} \exp\left[-\frac{1}{2}(\mathbf{x} - \boldsymbol{\mu}_i^{(x)})^T (\mathbf{C}_i^{(xx)})^{-1} (\mathbf{x} - \boldsymbol{\mu}_i^{(x)})\right]}{\sum_{i=1}^k c_i \det(\mathbf{C}_i^{(xx)})^{-1/2} \exp\left[-\frac{1}{2}(\mathbf{x} - \boldsymbol{\mu}_i^{(x)})^T (\mathbf{C}_i^{(xx)})^{-1} (\mathbf{x} - \boldsymbol{\mu}_i^{(x)})\right]}. \quad (15)$$

The covariance matrix of the GMM based regression estimate is

$$\begin{aligned} \mathbf{C}_{YY}(\mathbf{x}) = & \sum_{i=1}^k c_i \alpha_i(\mathbf{x}) \left\{ \left[\boldsymbol{\mu}_i^{(y)} + \mathbf{C}_i^{(yx)} (\mathbf{C}_i^{(xx)})^{-1} (\mathbf{x} - \boldsymbol{\mu}_i^{(x)}) \right] \left[\boldsymbol{\mu}_i^{(y)} + \mathbf{C}_i^{(yx)} (\mathbf{C}_i^{(xx)})^{-1} (\mathbf{x} - \boldsymbol{\mu}_i^{(x)}) \right]^T + \right. \\ & \left. \mathbf{C}_i^{(yy)} - \mathbf{C}_i^{(yx)} (\mathbf{C}_i^{(xx)})^{-1} \mathbf{C}_i^{(xy)} \right\} - \hat{\mathbf{y}}^{(regr)}(\mathbf{x}) \hat{\mathbf{y}}^{(regr)}(\mathbf{x})^T. \end{aligned} \quad (16)$$

The marginal pdf of \mathbf{X} is obtained from the joint pdf of \mathbf{X} and \mathbf{Y} as

$$f(\mathbf{x}) = \int_{-\infty}^{\infty} f(\mathbf{x}, \mathbf{y}) \mathbf{d}\mathbf{y} \quad (17)$$

and similarly for the marginal pdf of \mathbf{Y} , $f(\mathbf{y})$. Variables \mathbf{X} and \mathbf{Y} are statistically independent if their joint pdf is the product of their marginal pdfs, i.e., if $f(\mathbf{x}, \mathbf{y}) = f(\mathbf{x})f(\mathbf{y})$. The mutual information between \mathbf{X} and \mathbf{Y} is defined on the basis of the joint and marginal pdfs (Bishop 2006 (p. 57)):

$$I(\mathbf{X}; \mathbf{Y}) = \int \int f(\mathbf{x}, \mathbf{y}) \log \left(\frac{f(\mathbf{x}, \mathbf{y})}{f(\mathbf{x})f(\mathbf{y})} \right) \mathbf{d}\mathbf{x} \mathbf{d}\mathbf{y}, \quad (18)$$

where the integration is over the domains of \mathbf{X} and \mathbf{Y} . If the logarithm is of base e , the unit of MI is nat, and with base 2 logarithm the unit is bit. It is worth noting that both \mathbf{X}

and \mathbf{Y} can be multidimensional. In case of discrete representations of the pdfs, integration is replaced by summation.

Mutual information is a measure of how much information a variable carries about another variable, or equivalently, how much the uncertainty about one variable is reduced by knowing the value of the other variable. MI is symmetrical ($I(\mathbf{X};\mathbf{Y}) = I(\mathbf{Y};\mathbf{X})$) and non-negative – it reaches the value of zero if and only if the variables are statistically independent of each other. The interpretation of any nonzero value of MI may be less intuitive. Two methods are presented in this thesis to assist interpreting the MI results. First, the relation between MI and the commonly applied linear dependence measure, Pearson correlation, is presented. Second, Chapter 4 will introduce a method for producing reference MI readings from synthesized image data in order to assess the statistical significance of MI being nonzero.

When the random variables \mathbf{X} and \mathbf{Y} , having covariance matrices \mathbf{C}_X and \mathbf{C}_Y , respectively, follow a jointly Gaussian distribution with covariance matrix \mathbf{C} , it can be shown that their mutual information is

$$I(\mathbf{X}; \mathbf{Y}) = -\frac{1}{2} \log \left(\frac{|\mathbf{C}|}{|\mathbf{C}_X| |\mathbf{C}_Y|} \right) \quad (19)$$

with $|\mathbf{C}|$ denoting the determinant of matrix \mathbf{C} . In this case, mutual information does not reveal any additional information about the dependence compared to linear correlation carried by the joint covariance matrix. This is even more clearly seen when X and Y are scalar random variables with variances σ_X^2 and σ_Y^2 , respectively, and their Pearson correlation coefficient is ρ . The determinant of their covariance matrix is $|\mathbf{C}| = \sigma_X^2 \sigma_Y^2 (1 - \rho^2)$ and mutual information becomes

$$I(X; Y) = -\frac{1}{2} \log(1 - \rho^2). \quad (20)$$

In practice, the increase in MI between two (or more) variables can be often anticipated from the increasing correlation coefficient between them, even when the joint pdf of the variables is non-Gaussian. This reflects the fact that, while mutual information is a generic measure of the dependence between random variables, correlation coefficient is often a useful approximation of MI.

In several applications, the absolute values of MI are not as important as the maximization (or minimization) of MI when a variable is altered. This is the case, for instance, in various image registration applications where the objective in optimizing the image transformation parameters is to maximize the mutual information between the pair of images (e.g., (Viola and Wells 1997; Thévenaz and Unser 1998)). The minimization of MI has been found useful in blind source separation using independent component analysis (Kraskov et al. 2004). In this thesis, the main use of MI is in the comparison of various data selection setups. MI is estimated in this work from the parametric GMM presentation of the joint pdf instead of histogram, because the former produces relatively robust MI estimates whereas the histogram based MI tends to increase with increasing number of histogram bins.

3.3 Bayes network

Generally, given a set of random variables that are somehow related to each other, a complete description of the interdependences is the joint probability distribution of the variables. When this description is known, and data of one or several of the variables is obtained, inferring about a chosen variable (or variables) is accomplished through conditional distributions and marginalizing. This section introduces Bayes network (BN) as a tool for handling a large number of such probabilistically related random variables. The hierarchical image quality model of Oittinen et al. (2008) is briefly viewed to illustrate how the complicated construction of subjectively assessed quality can be systematically modeled by a Bayes network. At the end, a numerical example is given on the inference through BN.

Since the human experience of the printed product ultimately defines its quality and value, models have been sought to link the subjective assessments of print quality to the instrumentally measurable quality parameters of paper and print (Eerola et al. 2010; Lyne 1979; Mangin and Dubé 2006; Oittinen et al. 2008). The dependences between the subjective assessments and instrumental measurements are statistical rather than deterministic, which makes joint pdf the appropriate method for describing them. However, the number of variables can be large, and therefore the model of the overall joint pdf is not the most efficient approach. By introducing restrictions that allow the joint pdf to be written as a product of conditional pdfs, the number of parameters in the model is reduced. The resulting chain structure can be presented as a directed graphical model that is called Bayes network.

The Bayes network has been found a promising tool for the development of an evaluation framework for overall image quality (de Freitas Zampolo and Seara 2004; Eerola et al. 2010; Oittinen et al. 2008). BN is a directed acyclic graph that presents random variables and their dependencies probabilistically (Bishop 2006 (pp. 360-383)). In the graph, the nodes represent the random variables and the edges between the nodes denote conditional dependencies. The probabilistic modeling framework is in accordance with describing measurement uncertainty in more traditional measurement systems since each node actually contains a conditional probability for the node element value, given the values of the elements from which an arrow is pointing to the node in question. Thus the Bayes network model can account for the subjectivity of human assessments, as well as the uncertainties in instrumental measurements, and makes it possible to view the overall image quality as a probability distribution of states of quality.

The Bayes network can be used to simulate the hierarchical construction of printed image quality by a top-down layered structure (e.g., (Oittinen et al. 2008)). There may be several hierarchical levels in the perception of quality, and the instrumentally measured quality of the print is also considered to depend on the quality of the paper in a hierarchical manner. Figure 6 exemplifies the structure of a BN model of print quality with four levels, omitting the paper quality properties. The highest level is the subjectively assessed overall

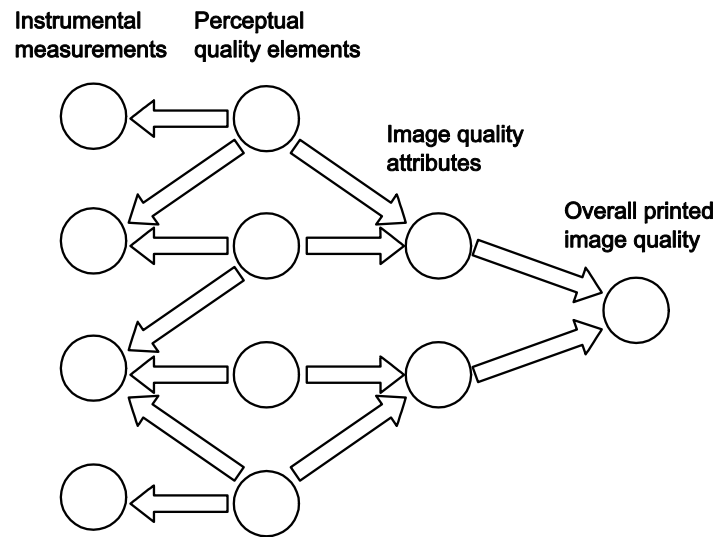


Figure 6. Graphical scheme of Bayes network model (Oittinen et. al 2008).

image quality on the right hand side of Figure 6. The second highest level consists of the high-level quality attributes such as the naturalness and informativeness discussed in Chapter 2. The essential difference between the overall quality and the high-level quality concepts is that the former is expected to be context dependent while the latter are not. The lowest perception level in the model of Figure 6 consists of special concepts called perceptual quality elements (PQEs). They are assumed to be the attributes of the image that the humans can directly assess and that their assessments – despite the non-physical nature – are objective. The PQEs reflect the state of reality concerning the perceived image quality and thus determine statistically both the instrumental measurement values of print quality and the higher level subjective print quality.

The identification of the structure and parameters of the BN requires reference measurements at the various abstraction levels. The subjective assessments of print quality made by a group of humans are used as reference. The edges that connect the attributes of consecutive levels of the model can be identified using a specified dependence measure, and placing edges where the dependence is relatively strong. Pearson correlation, mutual information and cumulative match score are examples of available dependence measures (Eerola et al. 2008a and 2008b; Phillips et al. 2000). Knowledge about the construction of the quality experience, based on studies of human behavior, can also be utilized in placing the edges (Janssen and Blommaert 1997; Leisti et al. 2009). The links in the structure are finally described by conditional probability densities.

The key idea in modeling the quality assessment with a Bayes network is that once the model has been identified, all probabilities can be updated with any new set of data. In particular, any evidence about a node state can be propagated through the network so that the probabilities of the image quality attributes and those of the states of overall image quality are updated. Obtaining evidence of quality attribute values through instrumental measurements and then inferring about the overall quality is the main intended use. However, it is recognized that predicting the overall print quality based on the instrumental quality measurements of the print – let alone the paper – is extremely

difficult. The uncertainty about the values of subjective quality attributes may become impractically large unless the quality evaluation task is carefully restricted with respect to the context, content of the images, printing method and paper type.

Finally, an example is given to illustrate how the BN model is used to infer about a print quality attribute given measurements of paper quality properties. Figure 7 illustrates a fictitious BN model in which smoothness and the uniformity of formation represent paper quality attributes that are observed only through measurements. Evenness and edge cleanness represent low level print quality properties, and naturalness is the higher level print quality attribute and the target of interest. The edges between the nodes have been placed for demonstration purposes and thus the model may not describe completely realistic dependences. In the following, smoothness, formation uniformity, print evenness, edge cleanness and naturalness are denoted by subscripts s, f, e, c and n, respectively, and measurements are denoted by apostrophes. According to Figure 7, the model can be written as

$$p(x'_s, x'_f, x_s, x_f, x_e, x_c, x_n) = p(x_s)p(x_f)p(x'_s|x_s)p(x'_f|x_f)p(x_e|x_s, x_f)p(x_c|x_s)p(x_n|x_e, x_c). \quad (21)$$

When the model is being used and experimental evidence on paper smoothness and formation are obtained through instrumental measurements x'_s and x'_f , the probability of each state of smoothness is obtained by the Bayes formula:

$$p(x_s|x'_s) = \frac{p(x'_s|x_s)p(x_s)}{\sum_{x_s} p(x'_s|x_s)p(x_s)}, \quad (22)$$

and similarly for formation uniformity. The probabilities of print evenness, edge cleanness and naturalness, given the measurements of paper smoothness and formation, are obtained by solving the conditional distribution

$$p(x_s, x_f, x_e, x_c, x_n|x'_s, x'_f) = \frac{p(x'_s, x'_f, x_s, x_f, x_e, x_c, x_n)}{\sum_{x_s} \sum_{x_f} \sum_{x_e} \sum_{x_c} \sum_{x_n} p(x'_s, x'_f, x_s, x_f, x_e, x_c, x_n)} = \frac{p(x'_s, x'_f, x_s, x_f, x_e, x_c, x_n)}{(\sum_{x_s} p(x'_s|x_s)p(x_s))(\sum_{x_f} p(x'_f|x_f)p(x_f))} \quad (23)$$

and then marginalizing this conditional joint distribution with respect to all quality attributes except the one that is of interest. For example, the distribution of naturalness is

$$p(x_n|x'_s, x'_f) = \sum_{x_s} \sum_{x_f} \sum_{x_e} \sum_{x_c} p(x_s, x_f, x_e, x_c, x_n|x'_s, x'_f). \quad (24)$$

In this example, each of the nodes of the BN model is assumed to have three discrete states, except smoothness and its measurement, which have five states. The states are denoted by numbers from 1 to 3 (or 5) so that an increase in the number means an increase in the given attribute. For example, state 5 in smoothness denotes high smoothness of the paper surface, state 3 in the uniformity of formation denotes small variation of local basis weight, and state 3 is the highest state of naturalness. Lacking the necessary measurement

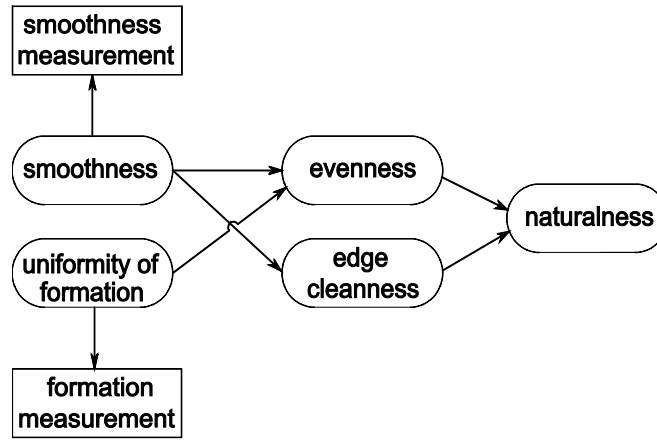


Figure 7. Graphical scheme of the example BN model.

data, the conditional probabilities that connect the nodes have been chosen synthetically for this example, and they are shown in the following tables. The measurement descriptions for the imperfect measurements are given in Table 1 and the conditional probabilities between the quality attributes are given in Tables 2, 3 and 4.

Table 1. Conditional probabilities of

(a) x'_s given x_s ,

x'_s	state of x_s				
	1	2	3	4	5
1	0.90	0.10	0	0	0
2	0.10	0.80	0.10	0	0
3	0	0.10	0.80	0.10	0
4	0	0	0.10	0.80	0.10
5	0	0	0	0.10	0.90

(b) x'_f given x_f .

x'_f	state of x_f		
	1	2	3
1	0.90	0.10	0
2	0.10	0.80	0.10
3	0	0.10	0.90

Table 2. Conditional probabilities of x_c given x_s .

x_c	state of x_s				
	1	2	3	4	5
1	0.90	0.70	0.15	0.10	0
2	0.10	0.20	0.70	0.25	0.10
3	0	0.10	0.15	0.65	0.90

Table 3. Conditional probabilities of

x_e given x_s and x_f .

	x_e	state of x_s				
		1	2	3	4	5
$x_f = 1$	1	0.80	0.70	0.50	0.40	0.30
	2	0.15	0.20	0.30	0.30	0.40
	3	0.05	0.10	0.20	0.30	0.30
$x_f = 2$	1	0.70	0.40	0.20	0.20	0.10
	2	0.20	0.50	0.60	0.50	0.30
	3	0.10	0.10	0.20	0.30	0.60
$x_f = 3$	1	0.30	0.30	0.15	0.10	0.05
	2	0.40	0.30	0.35	0.20	0.15
	3	0.30	0.40	0.50	0.70	0.80

Table 4. Conditional probabilities of

x_n given x_e and x_c .

	x_n	state of x_e		
		1	2	3
$x_c = 1$	1	0.80	0.60	0.30
	2	0.15	0.25	0.40
	3	0.05	0.15	0.30
$x_c = 2$	1	0.60	0.20	0.10
	2	0.25	0.60	0.30
	3	0.15	0.20	0.60
$x_c = 3$	1	0.30	0.10	0.05
	2	0.40	0.30	0.15
	3	0.30	0.60	0.80

The use of the model is exemplified in Table 5. First, in the upper part of Table 5, the measurements of paper smoothness and formation are thought to have provided the values $x'_s = 5$ and $x'_f = 2$. The probabilities of the actual states of smoothness and formation uniformity are then obtained from Table 1 and Eq. (22); by choosing uniform priors, i.e., $P(x_s = z) = 1/5$ for $z \in \{1, 2, 3, 4, 5\}$ and $P(x_f = z) = 1/3$ for $z \in \{1, 2, 3\}$, the distributions $p(x_s|x'_s)$ and $p(x_f|x'_f)$ are actually equal to those shown in Table 1. The distributions of the print quality attributes can be computed by Eq. (23) and marginalizing. The second and third columns of Table 5 show the distributions of print evenness and edge cleanness, respectively, and the fourth column shows the distribution of naturalness. All these distributions are conditional on the imperfect measurement values, x'_s and x'_f . For comparison, the last column of Table 5 shows the distribution of naturalness in case of perfect measurements, which means that $x_s = x'_s$ and $x_f = x'_f$. The effect of this on the distribution of naturalness is very small because of two reasons. Firstly, the uncertainty of the measurements, as described in Table 1, is reasonably small. Secondly, the conditional distributions $p(x_c|x_s)$, $p(x_e|x_s, x_f)$ and $p(x_n|x_e, x_c)$ flatten the originally sharp distributions $p(x_s|x'_s)$ and $p(x_f|x'_f)$. Table 5 does not demonstrate the effects of measurement uncertainty on the distributions of print evenness and edge cleanness, but they are only slightly more notable than those shown for naturalness. The computations described above are repeated for $x'_s = 2$ in the lower part of Table 5.

Table 5. Example of the propagation of probabilities in the BN model of Figure 7.

State	$p(x_e x'_s=5, x'_f=2)$	$p(x_c x'_s=5)$	$p(x_n x'_s=5, x'_f=2)$	$p(x_n x_s=5, x_f=2)$
1	0.12	0.01	0.11	0.10
2	0.31	0.11	0.25	0.24
3	0.57	0.88	0.64	0.66
State	$p(x_e x'_s=2, x'_f=2)$	$p(x_c x'_s=2)$	$p(x_n x'_s=2, x'_f=2)$	$p(x_n x_s=2, x_f=2)$
1	0.42	0.66	0.53	0.54
2	0.44	0.24	0.28	0.28
3	0.14	0.10	0.19	0.18

The results in Table 5 indicate that, for the smoother paper, with $x'_s = 5$, the most probable state of printed image naturalness according to this model is 3, i.e., the highest level. For the rougher ($x'_s = 2$) paper, the most probable state of naturalness is 1.

4 Methods applied to paper and print quality analysis

All analyses presented in this dissertation are based on image data. Two types of images are studied: paper surface topography maps and print reflectance maps. Both are obtained from a camera based arrangement that applies the photometric stereo principle presented in Section 2.2.2. The surface topography maps present local surface height values proportional to the pixel values; the mean plane is set to zero, positive values denote elevations, and negative values denote depressions. Print reflectance maps denote the presence or absence of printing ink by dark and light tones, respectively. Print reflectance values are always larger than zero. The same areas of the paper sheets are imaged before and after printing to be able to assess how much information about the printability of the paper can be obtained before it is printed. Image acquisition is followed by image registration and alignment, which enables the point-wise statistical analysis of the dependence between print reflectance and the surface topography of unprinted paper.

The quality of the raw data is defined by the quality of the image acquisition step. Section 4.1 discusses the distinctive features of the photometric stereo method and considers the sources of error related to the image acquisition. Image alignment is introduced in Section 4.2. The statistical analyses of the aligned image data are described in Section 4.3.

4.1 Image acquisition

The photometric stereo method is a favorable choice for data acquisition in this work. It provides surface topography and reflectance images from exactly the same area. It is contactless and requires no sample preparation. It is several orders of magnitude faster than an optical profilometer with a corresponding horizontal resolution in topography imaging. The field of view and pixel size can be selected suitable for small-scale print quality analysis. The images analyzed in this work contain 2268×1512 pixels and present an area of 22.5 mm by 15 mm. This results in a spatial resolution of approximately 10 μm . The images have been captured with a CCD camera in a laboratory-scale imaging setup with four lights: top, down, left and right (Ryynänen 2006). Using four instead of the originally proposed two light sources (Hansson and Johansson 2000; Johansson and Hansson 2004) compensates for the difficulty of detecting surface topography variations perpendicular to the illumination direction. In this sense, three-light photometric stereo arrangement (Hansson and Fransson 2004; Kuparinen 2008) would have been sufficient

as well. The commercial OptiTopo device has four light sources, and its topography reconstructions from paper surfaces have been found very similar to those produced by the current laboratory-scale setup (Ryynänen 2006).

The essential assumption made in the photometric stereo technique is the Lambertian surface reflection model (Born and Wolf 2006 (p. 195)). The Lambertian model states that the intensity of the light reflected diffusely from the surface is proportional to the cosine of the angle between the surface normal and the illumination direction, and does not depend on the viewing direction. Lambertian reflection is widely used as a model of diffuse reflection in computer vision. In photometric stereo it enables the determination of local surface normal vectors from the observed intensity of reflected light when the illumination angles are known. The normal vectors are converted to the gradient fields of the surface (Forsyth and Ponce 2003 (pp. 80-85)).

The deviation of paper surface from Lambertian behavior is the most severe source of error in determining the surface normals from photometric stereo images (Kuparinen 2008). Sharp elevations on a rough surface cast shadows, and specular reflection occurs at incidental points on the surface. Both problems can be alleviated by adjusting the illumination angle. Other sources of error lie in the imaging geometry, illumination and camera (Ray et al. 1983). To safely assume orthographic projection, the distance between the camera and the target should be much larger than any single dimension of the target. To arrange collimated incident light, the light sources should be placed further away from the target than the camera. The output of each light source should also be spatially and spectrally similar. The camera-related error sources include sensor noise, non-linearity of the camera response, optical aberrations and blur. Shot noise in the sensor follows Poisson distribution and thus deteriorates the signal-to-noise ratio more at low intensity than at high intensity pixels. Shot noise and the temperature dependent dark current noise are not considered severe problems in the laboratory device applied in this work, because the illumination and camera settings can be adjusted so that the pixel intensities are high but still not saturated. The camera response may also be assumed linear in this intensity range (Janesick 2001 (pp. 97-119)). Optical aberrations and blur slightly disturb the estimation of the surface normals.

Once the gradient fields have been estimated, they need to be integrated to obtain the topographic map of the 3D surface. However, the surface gradients are in practice non-integrable due to the violations of the reflection assumptions. Hansson and Johansson (2000) have approximated the surface topography by Wiener filtering the gradient directly in the Fourier domain and then computing the inverse Fourier transform. Given parametric estimates of image blur and noise, the Wiener filter aims to compensate for them. The four-light photometric stereo system employed in this work has applied Hansson's solution to both x-gradient and y-gradient. The resulting partial reconstructions have been averaged to form the final surface topography map. Kuparinen (2008) has recently investigated the optimal surface reconstruction schemes in photometric stereo in the presence of blur and noise. He has shown that the traditional non-parametric integration approaches, Frankot-Chellappa and Poisson integration, can be implemented

with Wiener filtering. Thus Wiener filtering of the gradient fields realizes the optimal surface reconstruction.

Each of the captured images exhibits a tilted intensity profile as a result of the directed illumination. Calibration images allow this effect to be removed from the images before gradient estimation. The reflectance map is practically a scaled average of the images from which the illumination pattern has been removed. The scaling step, which follows directly from the Lambertian reflection assumption, simultaneously converts the gray scale values of the topography map to millimeter units to describe surface height. Photometric stereo based surface topographies have been compared with reference measurements, made with mechanical and laser scanning devices, and the surface height estimates from the indirect but fast photometric stereo method have been found to correlate strongly with the reference measurements (Hansson and Johansson 2000; Kuparinen 2008; Publication I of this thesis). Correlation coefficients of 0.95 and higher have been reported by Hansson and Johansson (2000), using line profiles of LWC paper. On the other hand, the photometric stereo method has been shown to exhibit problems with rough grades such as base cardboard, where light cannot enter the deepest surface pores and hence the reconstructed surface seems smoother than indicated by the corresponding laser profilometer measurement (Kuparinen 2008). Similar dampening of the height values occurs at points where the paper surface absorbs light and redirects it internally (Barros and Johansson 2005). This problem is alleviated by the presence of small particles on the paper surface, e.g., coating and filler particles, and fines of mechanical pulp, that scatter the light sufficiently. The transparent fibers on the surface of SC paper violate the Lambertian reflection assumption (Kuparinen 2008), and it is also recognized in this thesis that they cause erroneous surface height estimates (Publications I and III). Finally, specular reflections from incidental points of the paper surface corrupt the local gradient estimation. Specular reflections have been eliminated in the two-light system of Hansson and Johansson (2000) by crossed polarizers. In the paper samples studied in this work, points of specular reflection are uncommon and they are not treated in any special way. It has been considered that the use of polarizers is unnecessarily complicated compared with the benefits when more than two light sources are employed.

The photometric stereo images have been acquired with a Foveon® X3 image sensor that detects RGB (red, green, blue) color data at each photosite. The topography maps have been computed from the mean of the color channels to minimize the noise in the topography map of unprinted paper. Print quality is assessed from one color channel of the reflectance map of the printed paper so that the selection of the color channel depends on the color of the printing ink. The red channel of the reflectance images is used with cyan ink, and the green channel is used with red ink, because these give the best contrast between white paper and inked areas.

4.2 Image alignment

Image registration refers to the process by which a suitable spatial mapping, or transformation, is estimated between the coordinates of two images: the reference and input image. The transformation parameters are used to align the images so that the pixels with the same coordinates in the two images correspond to the same physical part of the target. An automatic image registration procedure has been implemented in this work to align surface topography maps with subpixel accuracy. It has been first applied to surface topography maps acquired by scanning profilometers and photometric stereo, to compare the surface representations and to assess the suitability of the photometric stereo method for the topography measurement of paper and cardboard (Publication I). Later work, constituting a large majority of the analyses presented in this dissertation, relies on spatially aligned images of the reflectance of printed paper and the surface topography of unprinted paper. The alignment of these maps has been feasible for two reasons. First, the photometric stereo method inherently provides surface topography and reflectance maps that are exactly aligned with each other because they are based on the same photographs. Second, the surface topography maps acquired before and after printing contain similar texture by which they can be registered. The transformation is applied to the unprinted topography map to align it with the reflectance and topography maps of the printed paper. The unprinted topography map is thus the input image and the printed topography map is the reference image that is not altered in the alignment.

In general, the reference and input images may be shifted or rotated with respect to each other, the coordinate axes of one image may be oblique with respect to those of the other image (this is called shear), and the images may have scale differences or perspective view differences. The choice of the type of spatial image transformation depends on the presence of these misregistration factors. In the current application, the main causes of misregistration are translation (i.e., shift), rotation and scale changes. Slight shear of the coordinate axes are also possible within the different surface topography measurement devices. It is assumed that no perspective transformations are needed. Therefore a global affine transformation (Wolberg 1990 (pp. 47-51)) is the most suitable choice.

The registration method is based on point mapping which is the primary approach to register maps with random texture (Brown 1992). Before registration, the reference and input images are resampled to the same spatial resolution. In this work, resampling is only needed when comparing the profilometers and photometric stereo. The automatic registration procedure consists of two phases for accuracy and robustness. First the plain translation is identified and then the transformation estimate is refined iteratively. The first phase, illustrated in Figure 8, begins by placing a set of nine control points to the reference map. One of the points is in the center of the map and the remaining eight points are at distances of $-\delta$, 0, or $+\delta$ from the center in horizontal and vertical directions. The distance $\delta = \min(\frac{1}{5}\min(S_m, S_n), \frac{1}{10}\max(S_m, S_n))$, where S_m and S_n are the width and height of the image. Small areas, called templates, are selected around the control points and similar areas are searched from the input image to locate the matching points. The similarity

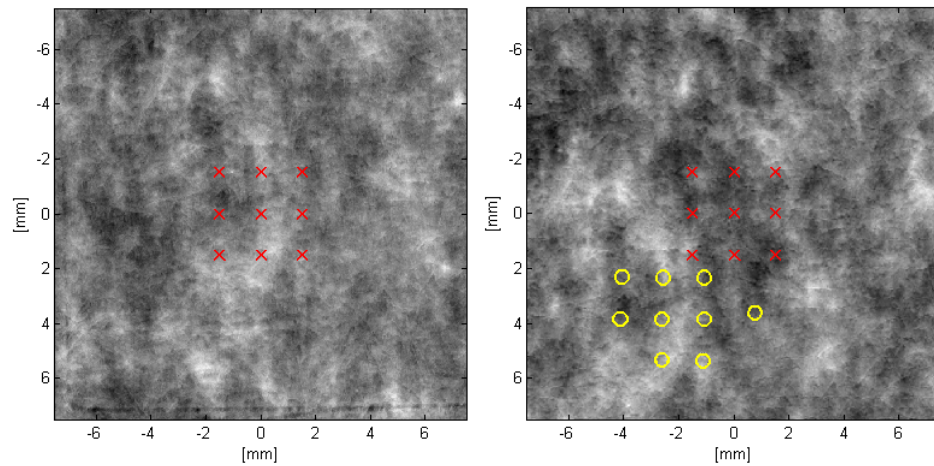


Figure 8. (Left): Reference topography map with nine control points. (Right): Input topography map with predicted matching points (red crosses) and found matching points (yellow circles). One of the nine points has not been found correctly.

measure is the 2D cross-correlation coefficient. The search result gives a coarse estimate of the translation between the images. Since not all the point pairs indicate exactly the similar translation, the true translation is assessed as a weighted median value of the nine translation estimates in horizontal and vertical directions.

In the second phase, the transformation estimate is iteratively refined with further control points. This phase generalizes the transformation estimate from plain translation to affine transformation. A user specified number of control points are positioned in a regularly spaced grid over the reference map and the points are then sorted into a list in ascending order according to their distance from the center of the map. At each iteration step, nine new control points are brought into play from the list in order, and the locations of these points in the input image are predicted with the transformation estimate from the previous iteration step. The transformation estimate is also used to warp the templates so that the potential rotation, shear and scale differences between the reference and input maps do not disturb the template matching. The exact locations of the matching points are again found by maximizing the 2D cross-correlation coefficients. Subpixel accuracy of each point is attained by fitting a second order 2D polynomial around the highest value in the cross-correlation function. Since an estimate of the required transformation exists, the search area size in the maximization in the second registration phase is considerably smaller than in the first phase. This makes the maximization computationally efficient. At the end of each iteration step, the point pairs found so far are used to form a new transformation estimate. A global affine transformation is fitted between the control points and matching points by weighted least squares in which the effect of false matches is minimized. The number of point pairs used for transformation fitting is approximately 100...300 on an image area of 330 mm^2 or smaller.

The matched point pairs gradually spread on the image as the iterations proceed, which improves the overall registration accuracy. When the sorted list of control points has been run through, the iterative procedure is terminated. The coordinates of the input image are warped by the estimated transformation, and pixel values are interpolated to the new non-

integer coordinates. When aligning images of different spatial resolution – as in the comparison of topography measurement devices – input image is chosen as the one with the higher resolution to minimize the amount of artificially interpolated data.

The uncertainty in image alignment originates from the uncertainty of matching point coordinates and from the assumptions made regarding the transformation type. Assuming that the selected transformation type is not a relevant source of error and thus describes the warping required to convert the images into the same coordinates, the uncertainty can be satisfactorily approximated by the transformation fitting error. It is the difference between the warped input image coordinates and the original reference image coordinates. The comparisons of the photometric stereo device against four scanning profilometers involve 89 pair-wise registrations of surface topography maps of paper and board. Affine transformation has been very suitable for that application. The transformation fitting errors are randomly oriented in the image plane and their root mean square value is below 0.1 pixels with a resolution of 20 pixels/mm (Publication I). The registration of 185 pairs of photometric stereo based surface topography maps, acquired before and after printing with a resolution of 100 pixels/mm, has revealed geometric distortions that cause occasionally larger than one pixel transformation errors in the corners of the images. To ensure accurate point-wise analysis of the data, only the parts of the images with less than half a pixel dislocation have been selected as the valid analysis area. The point-to-point correlation coefficient between the registered maps on the valid area is 0.8 or higher.

4.3 Statistical analysis methods

The main idea in the analysis is to utilize the large data set provided by image based measurement to estimate the marginal, conditional and joint probability density functions (pdfs; see Sections 3.1 and 3.2) of surface topography and print reflectance. The full joint pdfs reveal that the overall dependence between surface topography and print reflectance is weak; the observation of the local surface height in general gives only a weak indication of the reflectance of the printed surface at that point. The low probability tail areas of the pdfs are examined closer because they represent the abnormal regions of the paper and print. The objective is to offer answers to the question: How does the observation of an abnormal topography point on the paper surface change our information about whether the print quality attainable at that point will be abnormal or not?

This section introduces the methods applied to analyze the dependences between surface topography before printing and the reflectance of the same area after printing. First, the surface topography maps are preprocessed to emphasize the small-scale variations, and the analysis area is limited by two rules introduced in Subsection 4.3.1. The joint pdf of surface topography and print reflectance is estimated and its shape is assessed through conditional pdfs of print reflectance in Subsection 4.3.2. Subsection 4.3.3 describes how the tail areas of the pdfs are examined through binary maps of anomalous observations. In Subsection 4.3.4, the statistical dependences between surface topography and print reflectance are quantified by mutual information.

4.3.1 Preprocessing

The variation in surface topography maps is originally dominated by long wavelengths, i.e., cockling and waviness. The wavelength range is limited after image alignment to emphasize the roughness scale of individual fibers and fiber bundles that are relevant for printability analysis (Barros and Johansson 2005; Chinga et al. 2007; Kajanto et al. 1998; Preston et al. 2008). The surface topography maps are low-pass filtered with wavelength limit λ_{\max} using a Gaussian kernel, and the low-pass result is subtracted from the original image. The resulting image is referred to as the high-pass filtered topography map. Wavelength limits of 250 μm , 500 μm and 1000 μm have been tested.

The high-pass filtered surface topography maps are further processed into gradient and variance maps to examine whether these surface characteristics can help explaining missing printing ink. The gradient is evaluated in the direction of printing with a 3×3 Sobel-type gradient operator (Pratt 2001 (p. 456)). The convolution kernel for computing local variance has the shape of a circularly symmetrical 2D Gaussian or Gamma distribution (Bishop 2006 (p. 100)). The latter option enables a kernel shape with a hole in the center when the shape parameter of the Gamma distribution is 2 or larger. In practice, both options have produced rather similar local variance maps that give high values at the edges of pits and peaks on the surface. Figure 9 gives an example of the analyzed maps. It presents the print reflectance on a small solid print area printed with offset on a newsprint sheet, and shows the surface topography map, its local gradient and local variance from the same area before printing.

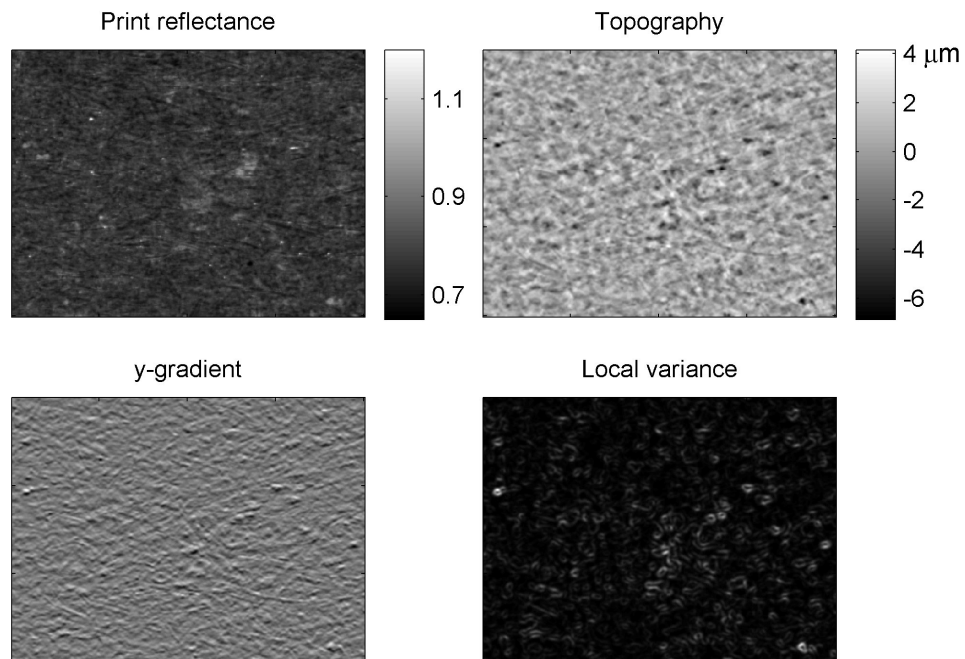


Figure 9. Print reflectance from a solid print area, high-pass filtered surface topography before printing, and the local gradient (in the printing direction) and local variance of the topography. The cut-off wavelength of the topography map is 250 μm . The presented image area is $4 \times 3 \text{ mm}^2$.

The analysis area is limited so that the geometrically distorted edges and corners of the images are discarded (see Section 4.2). The edge distortions induced by the filters are eliminated in the same process. Even after the limitation, the number of pixels available on an image area of 22.5 mm by 15 mm is more than two million. They are all utilized in the analysis of solid print areas. For print samples that contain screening, the raster dots are located from the print reflectance measurement to separate them from the white paper. The raster dot detection algorithm, described in Publication III and in (Lauri and Ihalainen 2010), first detects the regular dot pattern with 2D Fourier analysis. The exact dot positions are then refined by a cross-correlation based method in the spatial domain to account for the possible deviations from the regular pattern. Limiting the analysis to the raster dots reduces the number of pixels approximately by half.

4.3.2 Non-Gaussianity of probability densities

The joint probability densities of print reflectance and the topography-related properties are not Gaussian. This is demonstrated in Figure 10 by illustrations of the joint pdf estimates of print reflectance and surface topography measured from one of the newsprint samples examined in this work.

The non-Gaussianity of the pdfs can be verified by Kullback-Leibler distance, or relative entropy (Cover and Thomas 1991 (p. 22)). It is an information-theoretic measure of the “distance” between two probability distributions, $f_1(\mathbf{x})$ and $f_2(\mathbf{x})$:

$$D_{\text{KL}}(f_1(\mathbf{x})\|f_2(\mathbf{x})) = \int_{-\infty}^{\infty} f_1(\mathbf{x}) \log\left(\frac{f_1(\mathbf{x})}{f_2(\mathbf{x})}\right) d\mathbf{x} \quad (25)$$

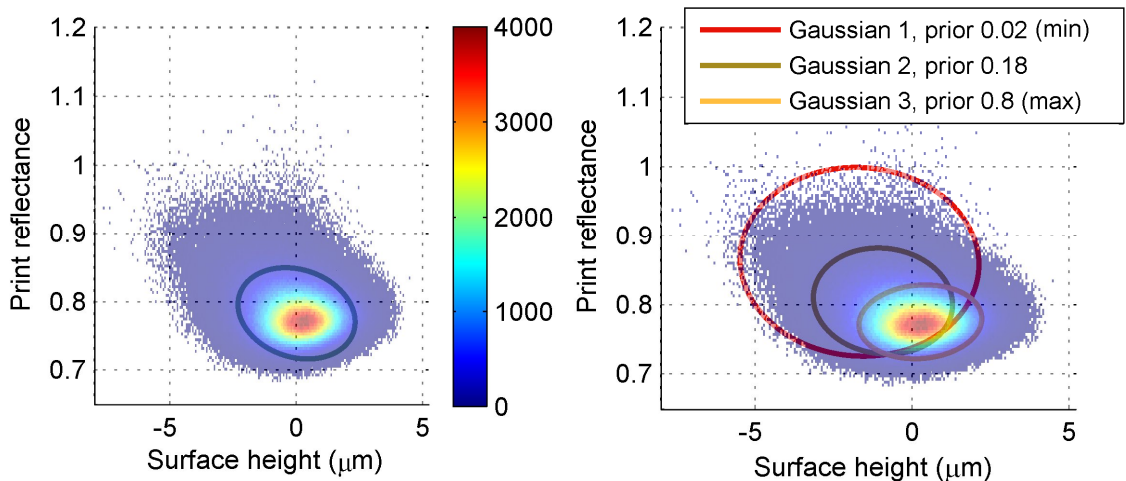


Figure 10. Gaussian (left) and 3-component GMM (right) estimates of the joint pdf of print reflectance and the surface topography of the unprinted paper. The 2D histogram is presented in the background and its color bar applies to both subfigures. The ellipses on top of the histogram are at the distance of two standard deviations from the centre of each Gaussian.

Kullback-Leibler (KL) distance is always non-negative and zero if and only if $f_1(\mathbf{x}) = f_2(\mathbf{x})$. If $f_1(\mathbf{x})$ is chosen as the histogram estimate or the GMM estimate of the pdf, and $f_2(\mathbf{x})$ is the Gaussian pdf estimate, the KL distance can be used to assess the appropriateness of Gaussian approximation to the pdf. The larger the KL distance the more the distribution ($f_1(\mathbf{x})$) deviates from a Gaussian distribution. Kullback-Leibler distance has been applied in Publication II to indicate the non-Gaussianity of the conditional pdfs of print reflectance given that surface height is below the average level (i.e., below zero). The skewness of the conditional pdfs has also been used for the same purpose.

The third method for assessing non-Gaussianity computes the percentage of print reflectance values that are exceptionally high in the subset of observations defined by a given topography limit. The exceptionality of the reflectance is defined by a large percentile of the overall distribution of reflectances in the imaged area, for instance 97.5 % or 99 % percentile; a reflectance value is exceptional if it exceeds the given percentile value. The method is referred to as tail analysis since it examines the high reflectance tail areas of the conditional pdfs, which themselves correspond to the low surface height tails of the joint pdf. The results can be tabulated or plotted as a function of the threshold set to the topography. Reference results are obtained by repeating the tail analysis to the Gaussian joint pdf model whose parameters have been estimated from the data. The method is demonstrated in Publication VI and results of the tail analysis are also exemplified in Chapter 5.

4.3.3 Anomaly maps

The tails of the pdfs are analyzed through maps of paper and print anomalies. These maps are of the same size as the measured property maps and they indicate the points and areas that show the most abnormal observations compared to the typical statistical behavior of the measured properties. The condition for an observation (vector) \mathbf{x} at location (m,n) to be abnormal to degree q is given as

$$f(\mathbf{x}) < C(q), \quad (26)$$

where $f(\mathbf{x})$ is the probability density function of the random variable \mathbf{X} and the relationship between C and q is determined through

$$q = q(C) = \int_{f(\mathbf{x}) < C} f(\mathbf{x}) \, d\mathbf{x} \quad (27)$$

In practice, the abnormality degree, q (e.g. 2.5 %), is first chosen. A suitable upper limit, C , is then determined for the probability density so that the integral in Eq. (27) equals q . The anomaly map is obtained by making a binary image where locations (m,n) that satisfy the condition (Eq. (26)) are given a value one (true) while all other locations assume value zero (false). In this work, anomaly maps are often referred to as masks since they determine the data points that are selected for further analysis. Mask percentage, i.e., the proportion of 1's in the binary map, equals the chosen abnormality degree, q .

A topography mask indicates the locations of the deepest depressions on the paper surface, i.e., the lowest intensity pixels of the topography map. A reflectance mask indicates the highest intensity pixels of the print reflectance image. Topography and reflectance masks are obtained by applying Equations (26) and (27) to the corresponding marginal pdfs. In addition, the joint pdf of the surface topography, its gradient and its local variance is used to make a map of the jointly anomalous points and areas of these three surface characteristics. The third topography based mask is aimed to find regions with low topography values that additionally have large local variation in topography. It is constructed by a two-step procedure in which topography depressions are first selected as anomalies, and the local anomalous areas are then increased if exceptionally high variance of surface height is found in the vicinity of the surface depression.

The abnormality degree, q , has a large impact on the analysis results. However, the value of q has to be set in the absence of a reference that would express the lower limit of print reflectance that disturbs the visual impression of the uniformity of print density. Various degrees of abnormality of print reflectance have therefore been tested from the range of 0.2 %...10 %. A wider range, from 0.2 % to 35 %, has been applied to the properties that describe surface topography. The locally adjusted topography mask is an exception, reaching a 0.5 % mask percentage at maximum. Table 6 presents a summary of the masks.

Table 6. Summary of masks.

Mask name	Points selected according to	Mask percentages
Topo	lowest values of unprinted topography	0.2 % ... 35 %
TGV	most unlikely combinations of topography, its gradient and its variance	0.2 % ... 35 %
LocalVar	a low percentage of the lowest topography spots with local refining to take into account the variance of surface topography values around the selected pits	0.2 % ...0.5 %
Refl.	highest values of print reflectance	0.2 % ... 10 %
Random	uniformly and randomly distributed points	0.2 % ... 35 %

Refl., Topo, and TGV masks with $q = 2\%$ are illustrated in Figure 11 for the solid print sample presented in Figure 9. The mask points are typically concentrated into various sizes of local areas. This is a practical indication of the mutual dependence of adjacent pixels. It has been studied in Publication IV and will be noticed also in Section 4.3.4 when generating simulated data. The size distribution of the concentrations of mask points will be returned to in the context of printing experiments in Chapter 5.

A straightforward way of gaining information about the origins of print defects is to quantify the conditional probability of finding abnormally high print reflectance from the points and areas that have been deemed abnormal based on topography, or vice versa. If the occurrence of an abnormality in the print reflectance does not depend on the classification (normal/abnormal) of the corresponding spot in the surface topography map, the expected coincidence of the reflectance mask with the abnormal topography spots equals the selected mask percentage. The coincidence analysis applies the same mask

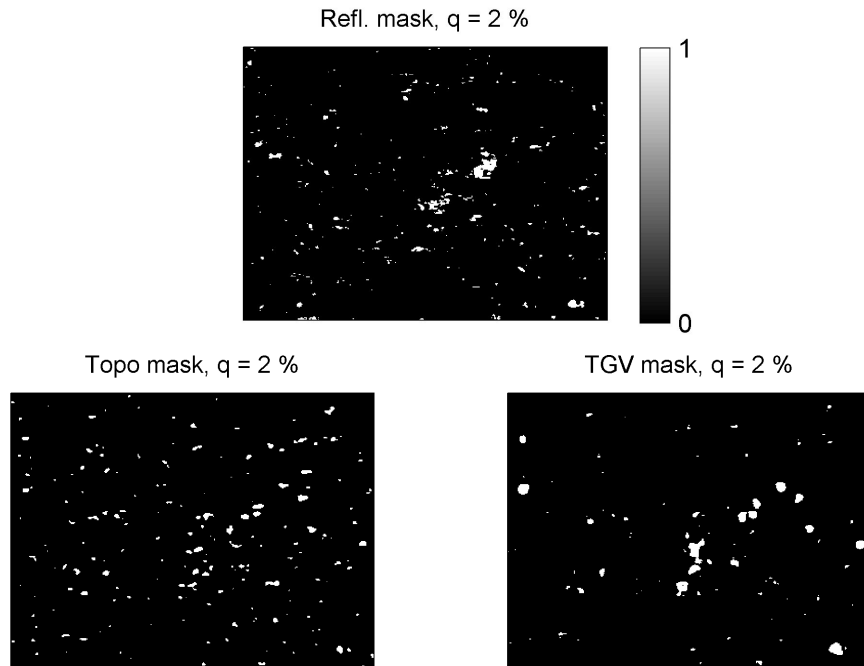


Figure 11. Reflectance mask and two topography based masks from the sample areas presented in Figure 9. The presented image area is $4 \times 3 \text{ mm}^2$.

percentage for both masks in the comparison to simplify the interpretation of the results. Increasing mask percentage increases the chance of accidental coincidence of the masks, which is taken into account in the results.

4.3.4 Mutual information and its significance

The joint pdf of print reflectance and surface topography deviates from Gaussian in the total imaged area, and even more so in the tails of the pdfs. The statistical dependences are therefore primarily quantified by mutual information. The two measured properties, print reflectance and surface topography, lend themselves to two analysis setups. The first setup starts with the anomalies in the print reflectance and examines whether the topography can be considered responsible for these print defects. The other alternative is to test how much information the various selections of surface property characteristics carry on print reflectance. In this approach the pixels are selected to the analysis according to the topography based masks.

The estimation of MI proceeds as follows. First, a mask is specified and the points indicated by the mask are collected from the maps of print reflectance (R), surface topography (T), the gradient (G) of topography and the variance (V) of topography. The joint pdf of these four variables is modeled by GMM. The marginalization of the 4-dimensional joint GMM provides the density estimates of lower dimensionality variables. For example, integrating over the value range of topography variance produces the joint pdf of print reflectance, surface topography and topography gradient.

The probability densities are modeled by GMMs. They are compact parametric models that make no assumptions about the form of the underlying pdf. The parameters of the GMM models are estimated by the component-wise EM algorithm proposed in (Figueiredo and Jain 2002). The user defines the minimum and maximum allowed number of Gaussian components and selects the covariance matrix type that is the same for all components. Full covariance matrices have been allowed in this work, and the number of components has been limited to the range from 1 to 10. The EM algorithm initializes the parameters of the components by K-means clustering. The initial covariance matrix of each component is calculated as the sample covariance matrix of the points associated with the corresponding cluster.

The determination of MI from the density estimate has been described in Section 3.2. The method is implemented numerically by drawing a large number ($10^5 \dots 10^6$) of samples from the joint pdf, evaluating their probabilities in the joint pdf and in the marginal pdfs, and summing the contributions of each sample to obtain the MI in bits.

Because MI is by definition larger or equal to zero, the MI estimate from a finite data set is always larger than zero even if the sampled variables were statistically independent. To assess the statistical significance of the MI between random variables \mathbf{X} and \mathbf{Y} , a simulation procedure is proposed, to test how the estimated MIs are distributed when the variables are statistically independent and the data set is of finite size. White noise is unsuitable as simulated data in this case, because it does not contain the spatial correlations present in the true data. A procedure is therefore needed to make the topography and print reflectance maps statistically independent while maintaining their internal spatial structure. This can be achieved by randomizing one of the maps. The topography map is chosen to be randomized.

The key idea in the randomization of the topography map is that the spectrum of the random map is kept identical to the spectrum of the original topography map, and hence the spatial autocorrelation of the data is kept identical as well. This is achieved through manipulation in the Fourier domain. The high-pass filtered surface topography map is first transformed into the Fourier domain by 2D discrete Fourier transform (DFT) (Sonka et al. 1999 (p. 602)):

$$\begin{aligned} \mathcal{F}(u, v) &= \frac{1}{S_m S_n} \sum_{m=0}^{S_m-1} \sum_{n=0}^{S_n-1} F(m, n) \exp \left\{ -i2\pi \left(\frac{mu}{S_m} + \frac{nv}{S_n} \right) \right\} \\ &= \mathcal{R}(u, v) + i\mathcal{J}(u, v), \end{aligned} \quad (28)$$

where $F(m, n)$ denotes the image intensity in spatial coordinates (m, n) , $i = \sqrt{-1}$, $\mathcal{R}(u, v)$ denotes the real part and $\mathcal{J}(u, v)$ the imaginary part of the Fourier coefficient $\mathcal{F}(u, v)$. The transform is presented in the amplitude and phase angle form as:

$$\mathcal{F}(u, v) = \mathcal{M}(u, v) \exp\{i\phi(u, v)\}, \quad (29)$$

where

$$\mathcal{M}(u, v) = [\mathcal{R}^2(u, v) + \mathcal{J}^2(u, v)]^{1/2} \quad (30)$$

is the amplitude and

$$\phi(u, v) = \tan^{-1} \left\{ \frac{\mathcal{J}(u, v)}{\mathcal{R}(u, v)} \right\} \quad (31)$$

is the phase of the Fourier coefficient. The phases at each frequency are then chosen as randomly and uniformly distributed values between 0 and 2π while keeping the amplitude unchanged. The modified phase is denoted as $\phi^{(\text{RP})}(u, v)$. Finally the 2D inverse DFT of the modified Fourier transform produces a simulated topography map whose variance and spectrum are identical to those of the original map but which is uncorrelated with the original map:

$$F^{(\text{RP})}(m, n) = \sum_{u=0}^{S_m-1} \sum_{v=0}^{S_n-1} \mathcal{M}(u, v) \exp\{i\phi^{(\text{RP})}(u, v)\} \exp\left\{i2\pi \left(\frac{mu}{s_m} + \frac{nv}{s_n}\right)\right\}. \quad (32)$$

The resulting image is referred to as random-phase topography. It replaces the original high-pass filtered topography map before the local gradient and local variance are computed, and before anomaly maps are made. The print reflectance map remains unaltered.

5 Experiments and results

The majority of the analyses and results in this dissertation deal with the characterization of the dependences between paper surface topography before printing and the reflectance of the same area after printing. This chapter thus concentrates on the printing experiments and summarizes the results that have been presented to a large degree in Publications II, III, IV and VI. The development of the image registration procedure and the evaluation of the feasibility of photometric stereo for surface topography measurement, reported in Publication I, are considered preparatory steps of the analysis, and have already been described in Sections 4.1 and 4.2. The treatment of print quality analysis in Publication V is a rather theoretical consideration of measurement information and its propagation in a Bayes network model, and as such does not provide results for this chapter.

The probabilistic analysis methods proposed in this work have been developed and tested with image data from two printing experiments. Section 5.1 describes the experiments and the preprocessing of the measurement data. Section 5.2 reviews Publications II and VI in assessing the non-Gaussianity of the conditional pdfs of print reflectance given that the surface height is within a specified range. The coincidence of abnormalities of print reflectance and surface topography is presented in Section 5.3, and the quantification of the dependences by mutual information is summarized in Section 5.4. Discussion of the analysis methods and results is presented in Section 5.5.

5.1 Measurement data

The largest data set analyzed in this work is from a pilot-scale sheet-fed offset (SFO) printing trial. It was conducted at Future Printing Center Oy (FPC, currently Forest Pilot Center Oy), Raisio, Finland, in 2006. Newsprint sheets were printed using a test layout from which two test areas of size $13.5 \times 5 \text{ cm}^2$ were selected for examination. Both test areas contain 100 % cyan printing but only one of them presents normal 4-color offset conditions. The other area was printed without water application and without back-trap conditions, i.e. only the cyan nip printing. The target density on both areas was 1.0. Mottling was measured by a scanner based system from the test areas, and print density variation was found consistently stronger in the non-back-trap area than in the normal printing area in the studied wavelength range, 0.35 mm to 20 mm. There were four groups of paper sheets, each representing different PPS roughness. Four paper sheets were randomly selected from each group and the specified test areas were imaged with the

photometric stereo device before and after printing. The images cover an area of $22.5 \times 15 \text{ mm}^2$. They were aligned as described in Section 4.2, and the valid analysis area was defined as described in Section 4.3.1. All image analyses are restricted to the valid areas.

One of the test sheets wrinkled in printing so that the normal 100 % cyan area became unusable. Consequently, 15 normal cyan areas and 16 non-back-trap areas were available for analysis. Table 7 summarizes the paper samples and test areas of the SFO experiment and reports the point-wise correlation coefficient between print reflectance and unprinted topography. The correlation coefficients have been computed on the total valid image areas and averaged over the three or four parallel samples of each roughness level and test area type.

Table 7. Summary of the material in the SFO experiment. PPS roughness of the sheets, number of test areas of each type, and point-wise correlation coefficient (ρ) between print reflectance and the high-pass filtered topography of the unprinted paper. The cut-off wavelength of the topography map is $250 \text{ }\mu\text{m}$.

PPS10	Normal cyan		Non-back-trap cyan	
	number of test areas	ρ	number of test areas	ρ
2.61 μm	4	-0.07	4	-0.14
2.77 μm	3	-0.11	4	-0.11
3.16 μm	4	-0.14	4	-0.22
3.63 μm	4	-0.15	4	-0.22

Another data set was obtained from a laboratory-scale gravure printing experiment at UPM Research Center, Lappeenranta, Finland, in 2007. In this experiment, the IGT printability tester equipped with the Heliotest printing disc (IGT Testing Systems 2003) was used to print supercalendered (SC) paper. The test material included three paper sheets of different PPS roughness, each of which was cut into eight strips of width 25 mm and length 300 mm. The strips were divided into groups so that three printing force levels could be tested: 250 N, 350 N and 600 N. While a large portion of the Heliotest layout is reserved by the variable halftone screen area that is usually examined for the 20th missing dot, the test area selected for the analyses of this work is from the 6 cm long conventional screening area that resembles visually fulltone printing. Informal subjective rankings of the printed paper strips were gathered independently from six persons, and the results showed unanimously that the most satisfying density and evenness of the test area was achieved by the printing with the highest printing force. The roughness of the papers had a secondary but logical effect on the quality rankings.

The same $22.5 \times 15 \text{ mm}^2$ test area of each SC paper strip was imaged before and after printing. The photometric stereo device was equipped with a bright light source at the reverse side of the paper so that a light transmittance image was obtained from exactly the same area as the topography and reflectance maps. The maps acquired before and after printing were aligned based on the texture of the topography maps. The screening was detected from print reflectance as described in Section 4.3.1 to restrict the valid analysis area to the locations of the raster points that are supposed to be covered by ink. The valid

analysis area was further decreased by omitting the fibers darkened by the supercalendering. They appear in the surface topography map as depressions rather than elevations, and give low reflectance values both in unprinted and in printed paper. The light transmittance map shows these fibers clearly as transparent patterns. The darkened fiber areas were detected based on the reflectance and transmittance maps of the unprinted paper, as described in Publication III, and discarded from the analysis area. All image analyses operate on the remaining valid area that contains approximately 0.85 million pixels per paper strip. Table 8 summarizes the material of the IGT experiment.

Table 8. Summary of the material in the IGT gravure printing experiment. PPS roughness, number of paper strips, and point-wise correlation coefficient (ρ) between print reflectance and the high-pass filtered topography map of the unprinted paper. The cut-off wavelength of the topography map is 250 μm .

PPS10	250 N		350 N		600 N	
	number of paper strips	ρ	number of paper strips	ρ	number of paper strips	ρ
1.11 μm	3	-0.14	3	-0.15	2	-0.13
1.15 μm	3	-0.17	3	-0.20	2	-0.19
1.24 μm	3	-0.26	3	-0.28	2	-0.25

The topography maps have been filtered before analysis to set an upper limit to the wavelengths of surface height variations. Wavelength limits of 250 μm , 500 μm and 1000 μm have been tested. The results indicate that the increasing cut-off wavelength slightly increases the point-wise correlation between print reflectance and the filtered surface topography of both newsprint and SC paper. On the other hand, the 250 μm limit conforms to a recommendation of ISO (NIST⁷ 2009). It allows the fine details of the measured topography maps to be discernible and it also matches the size of the raster dots in IGT gravure printing quite well. Most of the results reported in this thesis are based on topography data that has been filtered with the 250 μm wavelength limit. When other wavelength limits apply, it will be remarked in this chapter. Local gradient and local variance maps have been computed from the filtered surface topography maps. The reflectance and light transmittance images have not been filtered.

5.2 Non-Gaussianity

Due to the local deficiencies in ink coverage, the values of print reflectance scatter towards the high values. The distribution of surface topography values does not seem completely Gaussian either. The joint pdf of print reflectance and surface topography, as illustrated in Figure 10, is thus non-Gaussian. This has been quantified in Publication II by KL distance and skewness as described in Section 4.3.2. The results indicate that the conditional pdfs of print reflectance, given that surface height is below zero, are more skewed towards the high reflectance values in the non-back-trap samples of the SFO experiment than in the normally printed samples. This is related to the occurrence of missing ink and conforms to the mottling results.

⁷ National Institute of Standards and Technology

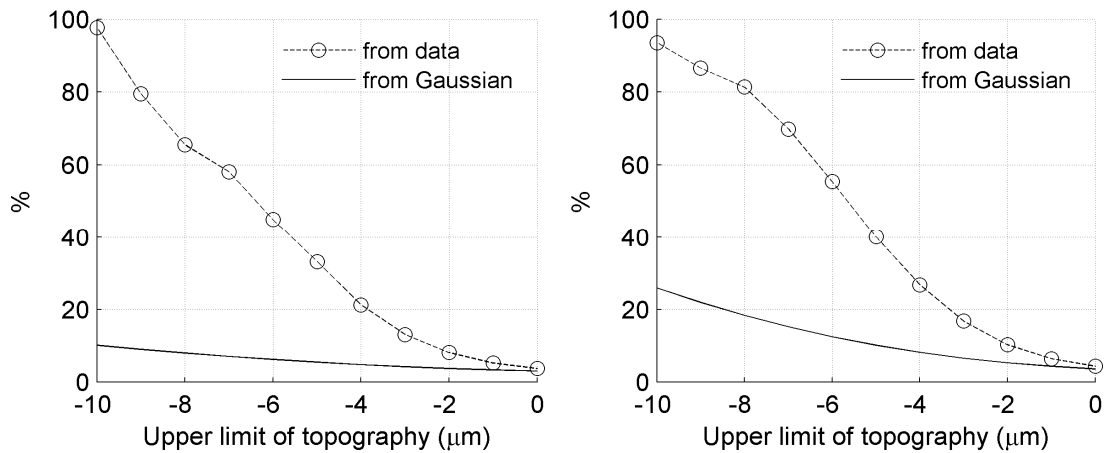


Figure 12. Tail analysis of the conditional pdfs of print reflectance on a 100 % cyan area in normal SFO printing (left) and on a 100 % cyan area printed without back-trap (right). The paper sample is a newsprint sheet of PPS roughness $2.61 \mu\text{m}$ and the topography map has been high-pass filtered with a cut-off wavelength of $500 \mu\text{m}$. The value on the horizontal axis is the upper limit of surface height: all data points that have surface height below this limit have contributed to the conditional pdf of print reflectance. The value on the vertical axis shows how many percent of these points have print reflectance value higher than the 97.5 % limit computed from all the print reflectance values in the image.

The tail analysis has been applied in Publication VI to SFO samples and to IGT samples. Figure 12 gives an example from a newsprint sheet. It shows that, for instance, selecting from the non-back-trap cyan area all the data points at which surface height is lower than $-5 \mu\text{m}$ results in a data set in which 40 % of the points have print reflectance value higher than the 97.5 % limit of all reflectance values in that test area (0.86 in this case). If the data were normally distributed, the corresponding portion of high reflectance values would be only 10 %, as indicated by the solid curve. The conclusion from both the SFO and IGT experiments is that depressions on the paper surface are associated with significantly increased probability of exceptionally high print reflectance.

5.3 Coincidence of anomalies

As described in Section 4.3, the analysis of the dependence between print reflectance and surface topography has been concentrated on the low probability tail areas of the pdfs. Binary masks have been made, as described in Section 4.3.3, to indicate the points and areas that exhibit anomalous values of print reflectance (R), surface topography (T), or the combination of surface topography, its local variance (V) and its local gradient (G). The spatial coincidence of paper and print anomalies has been quantified with various mask percentages. The results are expressed in this section as the conditional probabilities of finding abnormal print reflectance values from abnormal surface topography points.

The reflectance based mask is abbreviated as ‘Refl. mask’ and the two different topography based masks applied in the coincidence analysis are ‘Topo mask’ and ‘TGV mask’, as described in Section 4.3.3. The coincidence of reflectance based and topography

Table 9. Conditional probability of abnormally high print reflectance in the SFO case, given that surface topography has been found abnormal. Each entry in the table is the average of three or four parallel samples as listed in Table 7.

PPS10	q	Normal cyan		Non-back-trap cyan	
		Refl.-Topo	Refl.-TGV	Refl.-Topo	Refl.-TGV
2.61 μm	1.0 %	10.5 %	11.4 %	17.7 %	16.5 %
	2.5 %	13.0 %	14.3 %	20.3 %	19.9 %
	4.0 %	14.5 %	16.2 %	21.6 %	21.9 %
2.77 μm	1.0 %	13.7 %	14.8 %	16.2 %	15.9 %
	2.5 %	15.9 %	17.5 %	18.4 %	19.0 %
	4.0 %	17.0 %	19.2 %	19.8 %	21.2 %
3.16 μm	1.0 %	13.7 %	13.3 %	18.9 %	14.7 %
	2.5 %	16.6 %	16.5 %	22.2 %	18.1 %
	4.0 %	18.2 %	18.5 %	24.0 %	20.3 %
3.63 μm	1.0 %	12.5 %	12.5 %	19.2 %	15.8 %
	2.5 %	15.8 %	16.0 %	22.5 %	19.5 %
	4.0 %	17.8 %	18.3 %	24.3 %	21.6 %

based masks are reported for the SFO case in Table 9 with three mask percentages, q , that are the same for both masks that are being compared.

It must be noted in the table that the probability of accidental coincidence of the reflectance mask with the Topo mask or TGV mask equals q . This can be compensated for by subtracting the mask percentage from the conditional probabilities on each row of the table. Such subtraction has been done in Publications IV and VI which have reported mask coincidence results for the SFO case, and in Publication III for the IGT case. However, the subtraction has been omitted in Tables 9 and 10. The results in Table 9 show that when the mask percentage is increased from 1 % to 2.5 % (that is, 1.5 percentage units), the probability of finding abnormally high print reflectance in the points of abnormal surface topography always increases by more than 1.5 percentage units. A similar comparison between mask percentages of 2.5 % and 4 % shows that the coincidence of reflectance mask with the Topo mask does not usually increase further at higher mask percentages. In comparison, the coincidence of Refl. mask with the TGV mask has been found to favor large mask percentages, even up to 8 %. However, it is not meaningful to deem more than 3 %...4 % of the print reflectance values as abnormally high in the SFO case because missing printing ink is not that common (cf. Figures 9 and 11 in Chapter 4). The conclusion from Table 9 is that the probability of missing ink in points where surface topography is abnormal to degree 2.5 % or less is from 11 % to 18 % in the normally printed area and from 15 % to 23 % in the non-back-trap area. Selecting the abnormal topography points based on the bare surface height (Topo mask) seems justified from the viewpoint of the mask coincidence results.

Conditional probabilities of missing ink have also been evaluated in several size categories of the anomalous topography areas, selected by the Topo, TGV or LocalVar masks. The results have been reported in Publication IV. The maximum mask percentage in those experiments is 1.5 %. Similar results have been demonstrated with mask percentage of 2.5 % and topography cut-off wavelength of 500 μm in Publication VI for one of the smoothest newsprint sheets. It has been observed that while the TGV mask

tends to mark larger anomalous areas than the Topo mask, the latter coincides with the missing ink (Refl. mask) better than the former. The size categorization of Refl. masks up to $q = 3\%$ has shown that small anomalous areas in the print reflectance of the newsprint sheets are the most frequent. The measured area of $22.5 \times 15 \text{ mm}^2$ typically contains less than 60 anomalous spots whose size is 120 pixels or larger. If the anomaly concentrations had round shape, 120 pixels would correspond to an equivalent diameter of approximately $125 \mu\text{m}$.

Due to the raster pattern, the print reflectance maps of the gravure printed samples are very fragmented compared to the solid print samples examined in the SFO case. The anomalous areas marked by the reflectance mask in the IGT case are therefore small – very rarely larger than $80 \mu\text{m}$ in equivalent diameter. Missing ink in the gravure printed samples is thus related mostly with incompletely printed rather than totally absent raster dots. Applying similar practices as in Table 9, the coincidence of reflectance based and topography based masks are reported for the IGT case in Table 10.

Table 10. Conditional probability of abnormally high print reflectance in the IGT case, given that surface topography has been found abnormal. Each entry in the table is the average of two or three parallel samples as listed in Table 8. R denotes ‘Refl. mask’ and T denotes ‘Topo mask’ in this table.

PPS10	q	250 N		350 N		600 N	
		R-T	R-TGV	R-T	R-TGV	R-T	R-TGV
1.11 μm	1.0 %	4.9 %	3.9 %	4.5 %	3.4 %	6.8 %	5.4 %
	2.5 %	6.7 %	4.9 %	6.7 %	4.6 %	8.9 %	7.0 %
	4.0 %	8.6 %	6.0 %	8.6 %	6.0 %	10.4 %	8.0 %
1.15 μm	1.0 %	5.5 %	4.7 %	9.2 %	7.6 %	10.5 %	8.2 %
	2.5 %	7.5 %	5.9 %	11.1 %	8.5 %	12.5 %	9.5 %
	4.0 %	9.5 %	7.2 %	13.1 %	9.7 %	14.1 %	10.6 %
1.24 μm	1.0 %	9.9 %	8.4 %	12.7 %	9.8 %	13.9 %	10.2 %
	2.5 %	13.4 %	10.5 %	15.5 %	11.7 %	16.5 %	11.9 %
	4.0 %	16.0 %	12.0 %	17.6 %	13.4 %	18.6 %	13.6 %

It is seen that Topo mask outperforms TGV mask in selecting points that exhibit missing ink with higher than accidental probability. Figure 3 of Publication III illustrates that the probability of finding high print reflectance values from the Topo mask points improves up to mask percentages of 8 % or even higher in the roughest SC samples and also in the smoother SC papers when the printing force is less than 600 N. The maximum conditional probability of very high print reflectance is obtained from the roughest SC paper sample with the highest printing force. This maximum probability is approximately 20 % given that the surface height is within the lowest 5 % portion of all surface height values measured from the specified sample. Results that were not presented in Publication III have shown that if the same number of topography anomalies were selected from the same sample based on the jointly anomalous values of topography, its gradient and its variance (TGV mask), the conditional probability of very high print reflectance values would be approximately 15 %. Both the Topo mask and TGV mask have an increasing probability of coinciding with the print reflectance mask as the roughness of the paper or the printing force increases. Thus, while high pressure in the printing nip improves the visual print quality in the test paper strips, it also brings out the deep and incompressible surface

depressions that are not reached by the printing ink. A measurement of the compressibility of the paper would most likely improve the possibilities of predicting missing ink in gravure printing.

As expected, the roughness of the paper clearly affects the print quality in gravure printing. The rougher the paper, the more likely it is to find missing ink in the locations of paper surface depressions. In the SFO case, the amount of missing ink is not so clearly related to paper roughness, but the non-back-trap printing conditions induce missing ink more frequently than the normal printing conditions. In both the gravure and SFO printing experiments, the maximum probability of abnormally high print reflectance values in the abnormal surface topography points is approximately 20 % when the abnormality degree is 2.5 %...5 %. If the print abnormality degree is kept at this level while allowing the topography based masks to increase considerably, the latter can capture up to 65 % of the points of abnormally high print reflectance. However, this is hardly meaningful since the topography based mask would then have to pick every third point of the image. In conclusion, approximately 80 % of the points that exhibit exceptionally high print reflectance are such that the high reflectance is associated with other reasons than deep pits on the paper surface. While this result seems weak compared to the 50 % coincidence found by Barros and Johansson (2006) between UCA and topography depressions, there are various differences in the applied methods as well. The most plausible reasons for the different results are the low printing pressure applied by Barros and Johansson in their flexographic experiments, the relatively rough printing substrates (PPS10 up to 7.6 μm), and the fact that they allowed the number of points selected from the surface topography map to be larger than the number of UCA points (Barros and Johansson 2006).

5.4 Mutual information

The 4-dimensional joint pdfs of print reflectance and the three topography based variables have been estimated in various subsets of the multivariate data points. The subsets have been determined by the masks, as described in Chapter 4. The pdfs have been modeled by GMMs with a maximum of ten components. The pdf estimates have been utilized to evaluate mutual information (MI) between selected variables.

Publication IV reports the results of the MI analysis for the samples of the SFO experiment. The examined combinations of variables are denoted as RT, RTG, RTV and RTGV, which refer to the variables as described in the beginning of Section 5.3. These four combinations make it possible to assess how the local surface height, local surface gradient and local variance of surface heights contribute in explaining the variation of print reflectance. Each of the masks listed in Table 6 has been applied to select subsets of points, using mask percentages from 0.2 % to 1.5 %. The comparison of MI results obtained from different masks reveals the ability of each masking strategy to select points and regions in which the paper surface properties and print reflectance have significant statistical interdependence. According to the results in Publication IV, LocalVar masks and TGV masks are the best for this purpose. Topo masks give moderate MI results,

whereas the data subsets selected by Refl. masks show rather modest MI between print reflectance and surface topography. The random-phase simulations described in Section 4.3.4 have been applied to the SFO case in Publication IV to verify that the MI results estimated from the data denote true dependences between the measured variables even though the MI figures may seem rather small. The simulations have provided valuable reference MIs particularly for the larger combinations of variables, namely RTG, RTV and RTGV. They have led to the conclusion that print reflectance depends slightly more on the local variance of surface heights than on the local gradient. Random masks have been included in the tests to describe the overall statistical dependences of the variables, which are weaker than those computed with non-random masks.

The mutual information between print reflectance and surface topography is 0.27 bit at best when averaged over the 16 non-back-trap cyan test areas and 0.20 bit in the 15 normal cyan areas (Publication IV). These results have been obtained with extremely small mask percentage, $q = 0.2\%$, and it has been recognized that the LocalVar masks and TGV masks select data sets in which the MI results decrease when the mask percentage is increased. Later experiments (Publication VI) have shown that the Topo mask should also be made with a small mask percentage to maximize the MI within the masked points. In data subsets selected by the reflectance mask, the MI is weak but starts to increase when the mask percentage is increased beyond 1.5%. Comments on these findings will be presented in Section 5.5.

The statistical dependences found from the SFO data are summarized in Table 11 that enables the comparison of three types of results: the conditional probability of abnormal print reflectance given either the Topo or TGV mask, and the linear correlation (ρ) and mutual information (MI) within the data points selected by various masks. Both ρ and MI have been transformed to coefficient of determination, R^2 , which expresses how large portion of the variance of the target variable is explained by the explanatory variable(s). The target variable in this case is the print reflectance and the only explanatory variable is the unprinted surface topography. The R^2 results in Table 11 are expressed in percent. The conversion of MI to R^2 follows from Eq. (20).

Table 11. Summary of the results of the SFO case, with mask percentage $q = 1.5\%$. The R^2 results have been scaled to percents.

PPS (μm)	Cond. prob.		$100 \cdot R^2 = 100 \cdot \rho^2$				$100 \cdot R^2 = 100 \cdot (1 - 2^{-2MI})$			
	R-T	R-TGV	Rand. mask	T mask	TGV mask	R mask	Rand. mask	T mask	TGV mask	R mask
Normal cyan										
2.61	11.4 %	12.4 %	0.6	7.1	6.9	0.0	1.6	9.0	10.3	2.6
2.77	14.5 %	15.7 %	1.3	11.7	9.6	0.3	2.7	12.4	12.3	2.5
3.16	14.8 %	14.5 %	2.5	9.2	13.1	0.2	3.5	10.7	16.5	2.6
3.63	13.8 %	13.8 %	2.4	8.7	11.3	0.0	3.0	10.1	14.8	2.3
Non-back-trap cyan										
2.61	18.7 %	17.8 %	2.0	10.7	14.5	0.9	3.9	11.7	17.8	5.1
2.77	17.0 %	17.0 %	1.4	10.6	12.6	0.5	3.2	12.1	15.2	3.7
3.16	20.1 %	16.0 %	4.3	9.6	22.2	1.4	5.6	10.9	26.0	6.2
3.63	20.4 %	17.2 %	4.7	9.4	20.6	2.0	6.0	11.3	24.0	7.0

Table 11 shows that the R^2 computed from MI is slightly higher than that computed from the linear correlation coefficient. This implies that the dependence between surface topography and print reflectance cannot be entirely captured by a linear model, particularly within the data points selected by the TGV mask or by the reflectance mask. It is also observed that while the points of missing ink typically coincide less frequently with TGV mask points than with Topo mask points, the mutual dependence of the topography-reflectance pairs is maximized when the point pairs are selected by the TGV mask.

All masks except the LocalVar mask have also been tested in the analysis of the IGT data. Mask percentages from 0.5 % to 4 % have been tested in the MI computation. For the sake of completeness, the results are presented in Table 12 using the same notations as in Table 11. The mask percentage applied in Table 12 is $q = 1\%$. All the MI figures have been found to decrease when the mask percentages increase.

Table 12. Summary of the results of the IGT case, with mask percentage $q = 1.0\%$. The R^2 results have been scaled to percents.

PPS (μm)	Cond. prob.		$100 * R^2 = 100 * \rho^2$				$100 * R^2 = 100 * (1 - 2^{-2MI})$			
	R-T	R-TGV	Rand. mask	T mask	TGV mask	R mask	Rand. mask	T mask	TGV mask	R mask
250 N										
1.11	4.9 %	3.9 %	2.1	1.6	5.5	1.1	2.6	4.6	9.7	3.3
1.15	5.5 %	4.7 %	2.9	1.4	7.0	0.7	3.5	4.7	9.9	2.4
1.24	9.9 %	8.4 %	7.9	5.8	24.9	0.4	7.9	9.9	29.1	2.7
350 N										
1.11	4.5 %	3.4 %	2.1	1.3	4.6	0.7	2.6	3.6	9.5	2.9
1.15	9.2 %	7.6 %	3.8	4.9	17.0	2.9	5.2	7.4	22.6	4.6
1.24	12.7 %	9.8 %	7.9	8.2	31.9	1.9	8.5	10.6	34.3	5.8
600 N										
1.11	6.8 %	5.4 %	1.6	2.8	5.4	0.8	2.2	6.0	8.8	3.3
1.15	10.5 %	8.2 %	3.9	5.3	14.7	3.0	4.5	8.2	21.7	5.5
1.24	13.9 %	10.2 %	6.4	9.7	32.3	1.1	7.1	11.3	32.6	6.1

The results from the IGT experiment are very similar to those from the SFO experiment in that clearly the strongest statistical dependence between print reflectance and surface topography is found in the subset of data selected by the TGV mask. Comparing the linear correlation based and mutual information based R^2 values computed in the random mask implies that the overall dependence between print reflectance and surface topography is practically linear but very weak.

5.5 Discussion

The paper samples analyzed in this work have shown weak overall dependence between print reflectance and paper surface topography. This is in line with the results of other studies in which pixel-to-pixel correlation has been computed between topography and print unevenness in offset printing (Dickson 2006; Kajanto 1989) and in gravure printing (Hirn et al. 2009). Print density is known to depend on various paper properties, such as formation and porosity, not to mention the variables related to the press operation and ink

(Fetsko and Zettlemoyer 1962; Mangin and Geoffroy 1989; Parker 1973). While local surface height is a poor predictor of local print density in general, a closer examination of the low probability tail areas of the pdfs has indicated that deep depressions on the paper surface cause increased probability of missing ink both in sheet-fed offset and in gravure printing. The capability of surface topography values to explain the variation in print reflectance has also been found better in the neighborhood of surface depressions than overall on the paper surface. Deriving the results through probability density estimates and mutual information ensures that potential non-linear dependences between the variables are also taken into account.

Topo masks and Refl. masks made with an identical mask percentage from the images of the SFO printed newsprint coincide most frequently when the mask percentage is 1 %...3 %. In addition, the mutual information between print reflectance and surface topography in the topography based masks (Topo, TGV, LocalVar) decreases when the mask percentage is increased. These findings support small mask percentages, which feel reasonable also from the viewpoint of print reflectance that quite rarely shows missing ink in the newsprint samples. In the gravure printed SC samples, missing ink is more common. The clustering of the raster dots, presented in Publication III, has shown that even in the highest quality gravure sample the portion of successfully printed dots is approximately 80 %. The rest of the dots suffer from different degrees of missing ink. The mask coincidence tests suggest that the optimal mask percentage is higher for the SC samples than for the newsprint samples. However, the decline of MI at increasing mask percentages support small masks also for the SC data. Finally, the areas of abnormally high print reflectance (i.e., areas denoted by the Refl. mask) show only modest mutual information between the reflectance and surface topography. This must be due to the fact that a majority of the missing ink is induced by other factors than surface topography, as pointed out at the end of Section 5.3. The increase in MI with increasing reflectance mask percentage in the SFO case is explained by the mask starting to select also points of less severe print abnormality.

The local areas detected as print defects in the studied SC and newsprint samples are small, even though the wavelengths of the print reflectance map are not limited by filtering. However, several spots of missing ink have been found close to each other, and this micro scale noise is believed to cause uneven appearance of the print and thus deteriorate the visual print quality (Saarelma and Oittinen 1993 (p. 357)). In the gravure printed samples, the size and shape of the raster dots varies due to occasional missing ink, which causes visually detectable unevenness. It is possible that a small proportion of the detected abnormally high reflectance points are due to specular reflections, but their effect on the results can be considered negligible.

The printing experiment with SC paper and gravure printing is more relevant for commercial printing than sheet-fed offset with newsprint. The gravure technique introduces the need to detect the screen pattern that is inherent in practically all printed products. The gravure experiment has also demonstrated the dependence of print quality on paper roughness. However, the conclusion from both printing experiments is that the

prediction of missing ink based on surface topography anomalies involves considerable uncertainties. Missing ink can be caused by various reasons related to paper properties and to the interaction of paper and the printing process. For instance, a measurement of the dynamic contact pattern of paper with the printing nip (e.g., (Preston et al. 2008)) would very likely yield more accurate predictions of missing ink in gravure. It must be noted that the analysis methods proposed in this thesis are not limited to surface topography and local print reflectance measurements. A map of the local variations of print gloss is also relevant for print quality analysis (MacGregor et al. 1994), and the measurements of paper properties could include, for instance, local compressibility (Mangin et al. 1993), apparent density (Sung et al. 2005), local mass density (Kajanto 1991) or light transmittance (MacGregor and Johansson 1990 and 1991). It is expected that the simulation procedure presented in Section 4.3.4 is a feasible tool for verifying the statistical significance of the dependences found from aligned images also when other properties than surface topography and print reflectance are measured.

The introduction of the Bayes network to the analysis of print quality has so far been merely theoretical in this work. The review of the aspects of perceived print quality presented in Section 2.1 has offered some perspectives to the essential components of the model. The probabilistic approach to analyzing the dependences, applied to print reflectance variations and surface topography in this thesis, naturally connects with the principles of Bayes network. However, given the weak dependence between surface topography and missing ink, it will be necessary to consider, based on the use case at hand, whether the detection of the surface depressions of paper is a relevant input to the model aimed at predicting print quality.

6 Conclusions

This thesis has presented methods for studying the dependences between small-scale print unevenness and the local characteristics of paper surface using image based measurements. The presented analyses have been concentrated on missing ink and its predictability given the surface topography measurement before printing.

Accurate alignment of the measurements is a prerequisite for the statistical analyses. A robust method for registering and aligning the images acquired before and after printing has been developed. It is capable of subpixel registration and it requires no marking of the samples. The method has been developed using various surface topography maps that have also enabled the comparison between scanning profilometers and a photometric stereo method. The analyses have thereafter concentrated on the joint analysis of paper surface topography and print reflectance. Both have been acquired with the photometric stereo device. The print reflectance maps have been aligned with the topography maps of the unprinted paper by utilizing the similar texture features of the unprinted and printed topography maps.

Image data from two printing experiments has been analyzed. The first experiment is a pilot-scale offset printing trial with newsprint sheets, and the second consists of SC papers printed with a gravure printability tester in laboratory conditions. In the proposed analysis procedure, the aligned images are used to estimate the joint pdfs of print reflectance and the surface topography characteristics – the topography, its local gradient and its local variance. Pdf describes the probabilistic dependences between its constituent variables and it is efficiently parameterized by GMM. In addition to evaluating the dependences within the total imaged area, anomaly maps are derived to signify the points and areas that deviate most strongly from the typical statistical behavior of the measured variables. The coincidence of print reflectance anomalies with the anomalous points of surface topography characteristics expresses the conditional probability of finding missing ink in points and areas that show exceptional behavior of surface topography. This probability has been found to be approximately 20 % in both the data sets examined. The large number of independent data points in the aligned images enables also probability densities to be estimated within the points denoted by the anomaly maps.

The dependences expressed by the pdf estimates are quantified by mutual information which is a generalized measure of statistical dependence. It enables the assessment of the linearity of the dependences found between print reflectance and the topography

characteristics. The results imply that linear correlation is in many cases a feasible approximation of the dependence in this type of print quality analysis, but the mechanism by which the extreme topography values cause missing printing ink includes non-linear effects as well. The dependences between local surface height and local print reflectance are weak but statistically significant in the two data sets examined in this work. The non-Gaussian statistical models between surface topography and print reflectance show a maximum coefficient of determination of approximately 25 % in the SFO experiment and 34 % in the gravure experiment. These figures have been obtained among selected points of abnormal surface topography. Using all the points in the image area produces considerably lower coefficients of determination. All results are based on thousands of data points. The fact that neighboring pixel values in the images typically depend on each other, which reduces the effective number of independent observations, has been taken into account in the simulation that verifies that the mutual information assessed from the measurement data is significantly larger than zero.

While the absence of print defects and the even appearance of the image area affect positively on print quality, they are not the only factors that determine the quality. The possibility to connect several technical measurements and subjective quality perception into a quality model with the Bayes network principle will therefore be an interesting area to investigate in the future. The potential of the fast camera based measurement device in the characterization of the reflectance and surface topography of paper will also be utilized in future research. Even though the surface topography maps acquired by photometric stereo contain erroneous surface height estimates in certain circumstances, the results obtained in this work indicate that the maps carry information about the printability of the paper. This encourages the application of the photometric stereo method for topography and reflectance imaging both in laboratory and on-line.

Bibliography

- Barros, G.G. (2006): *Influence of substrate topography on ink distribution in flexography*. PhD thesis, Karlstad University, Karlstad, Sweden.
- Barros, G.G., Fahlerantz, C.-M. and Johansson, P.-Å. (2005): Topographic distribution of UnCovered Areas (UCA) in full tone flexographic prints. *TAGA J.*, Vol. 2, No. 1, pp. 43-57.
- Barros, G.G. and Johansson, P.-Å. (2005): The OptiTopo technique for fast assessment of paper topography – Limitations, applications and improvements. *J. Imaging Science and Technology*, Vol. 49, No. 2, pp. 170-178.
- Barros, G.G. and Johansson, P.-Å. (2006): Prediction of UnCovered Area occurrence in flexography based on topography – A feasibility study. *Nordic Pulp & Paper Research J.*, Vol. 21, No. 2, pp. 172-179.
- Bichard, W. (1992): The inter-relationship among air-leak roughness/smoothness methods: A Canadian newsprint study. *Pulp & Paper Canada*, Vol. 93, No. 6, pp. 43-48.
- Bishop, C.M. (2006): *Pattern recognition and machine learning*. Springer, Singapore.
- Bliesner, W.C. (1964): A study of the porous structure of fibrous sheets using permeability techniques. *Tappi*, Vol. 47, No. 7, pp. 392-400.
- Bliesner, W.C. (1970): Dynamic smoothness and compressibility measurements on coated papers. *Tappi*, Vol. 53, No. 10, pp. 1871-1879.
- Bloch, J.-F. and Rolland du Roscoat, S. (2009): Three-dimensional structural analysis. In: *Trans. 14th Fund. Res. Symp.*, Oxford, 2009, (I'Anson, S.J., ed.), FRC, Bury, UK, 2009, pp. 599-664.
- Blokhuis, G. and Kalff, P.J. (1976): Dynamic smoothness measurements of papers and print unevenness. *Tappi*, Vol. 59, No. 8, pp. 107-110.
- Born, M. and Wolf, E. (2006): *Principles of optics* (7th expanded ed.). Cambridge University Press, Cambridge, UK.
- Bristow, J.A. and Ekman, H. (1981): Paper properties affecting gravure print quality. *Tappi*, Vol. 64, No. 10, pp. 115-118.

Brown, L.G. (1992): A survey of image registration techniques. *ACM Computing Surveys*, Vol. 24, No. 4, pp. 325-376.

Bruning, J.H., Herriott, D.R., Gallagher, J.E., Rosenfeld, D.P., White, A.D. and Brangaccio, D.J. (1974): Digital wavefront measuring interferometer for testing optical surfaces and lenses. *Applied Optics*, Vol. 13, No. 11, pp. 2693-2703.

Chase, L.M. and Goss, J. (1997): A surface properties sensor for the paper industry. *Proc. XIV IMEKO World Congress*, Tampere, Finland, 1997, Vol. XA, pp. 37-47.

Chinga-Carrasco, G. (2009): Exploring the multi-scale structure of printing paper - a review of modern technology. *J. Microscopy*, Vol. 234, No. 3, pp. 211-242.

Chinga, G., Johnsen, P.O., Dougherty, R., Berli, E.L. and Walter, J. (2007): Quantification of the 3D microstructure of SC surfaces. *J. Microscopy*, Vol. 277, No. 3, pp. 254-265.

Corte, H. and Kallmes, O. (1961a): Statistical geometry of a fibrous network. In: *Trans. 2nd Fund. Res. Symp.*, Oxford, 1961, (Bolam, F., ed.), BPBMA, London, UK, 1962, pp. 13-46.

Corte, H. and Kallmes, O. (1961b): The interpretation of paper properties in terms of structure. In: *Trans. 2nd Fund. Res. Symp.*, Oxford, 1961, (Bolam, F., ed.), BPBMA, London, UK, 1962, pp. 351-368.

Corte, H.K. and Lloyd, E.H. (1965): Fluid flow through paper and sheet structure. In: *Trans. 3rd Fund. Res. Symp.*, Cambridge, 1965, (Bolam, F., ed.), BPBMA, London, UK, 1966, pp. 981-1009.

Cover, T. and Thomas, J. (1991): *Elements of information theory*. John Wiley & Sons, New York, USA.

de Freitas Zampolo, R. and Seara, R. (2004): Perceptual image quality assessment based on Bayesian networks. *Proc. IEEE Int. Conf. Image Processing (ICIP)*, Singapore, 2004. pp. 329-332.

Dempster, A.P., Laird, N.M. and Rubin, D.B. (1977): Maximum likelihood from incomplete data via the EM algorithm. *J. Royal Statistical Society, Series B*, Vol. 39, No. 1, pp. 1-38.

Dickson, A.R. (2006): Evaluating the relationship between grammage, topography and print properties in newsprint. *Proc. 60th Appita Annual Conf.*, Melbourne, Australia, 2006, pp. 19-23.

Diesen, M. (1998): *Papermaking Science and Technology, Book 1, Economics of the pulp and paper industry*. Fapet Oy, Jyväskylä, Finland. p. 23.

Dodson, C.T.J. (2001): On the distribution of pore heights in random layered fibre networks. In: *Trans. 12th Fund. Res. Symp.*, Oxford, 2001, (Baker, C.F., ed.), FRC, Bury, UK, 2002, pp. 1037-1042.

Dodson, C.T.J. and Sampson, W.W. (1996): The effect of paper formation and grammage on its pore size distribution. *J. Pulp and Paper Science*, Vol. 22, No. 5, pp. 165-169.

- Dodson, C.T.J. and Sampson, W.W. (2005): Effect of correlated free fibre lengths on pore size distribution in fibrous mats. In: *Trans. 13th Fund. Res. Symp.*, Cambridge, 2005, (I'Anson, S.J., ed.), FRC, Bury, UK, 2005, pp. 943-960.
- Draper, N.R. and Smith, H. (1998): *Applied regression analysis* (3rd ed.). John Wiley & Sons, New York, USA.
- Eckert, M.P. and Bradley, A.P. (1998): Perceptual quality metrics applied to still image compression. *Signal Processing*, Vol. 70, No. 3, pp. 177-200.
- Eerola, T., Kämäräinen, J.-K., Leisti, T., Halonen, R., Lensu, L., Kälviäinen, H., Nyman, G. and Oittinen, P. (2008a): Is there hope for predicting human visual quality experience? *Proc. IEEE Int. Conf. Systems, Man, and Cybernetics (SMC)*, Singapore, 2008, pp. 725-732.
- Eerola, T., Kämäräinen, J.-K., Leisti, T., Halonen, R., Lensu, L., Kälviäinen, H., Oittinen, P. and Nyman, G. (2008b): Finding best measurable quantities for predicting human visual quality experience. *Proc. IEEE Int. Conf. Systems, Man, and Cybernetics (SMC)*, Singapore, 2008, pp. 733-738.
- Eerola, T., Kämäräinen, J.-K., Lensu, L. and Kälviäinen, H. (2007): Visual print quality evaluation using computational features. *Proc. 3rd Int. Symp. Visual Computing (ISVC)*, Lake Tahoe, NV/CA, USA, 2007, pp. 403-413.
- Eerola, T., Lensu, L., Kämäräinen, J.-K., Leisti, T., Ritala, R., Nyman, G. and Kälviäinen, H. (2010): Bayesian network model of overall print quality: construction and structural optimisation. Submitted to *Pattern Recognition Letters*.
- Engström, G. (1994): Formation and consolidation of a coating layer and the effect on offset-print mottle. *Tappi J.*, Vol. 77, No. 4, pp. 160-172.
- Ferris, T.L.J. (2004): A new definition of measurement. *Measurement*, Vol. 36, No. 1, pp. 101-109.
- Fetsko, J.M. and Zettlemoyer, A.C. (1962): Factors affecting print gloss and uniformity. *Tappi*, Vol. 45, No. 8, pp. 667-681.
- Figueiredo, M.A.T. and Jain, A.K. (2002): Unsupervised learning of finite mixture models. *IEEE Trans. Pattern Analysis and Machine Intelligence*, Vol. 24, No. 3, pp. 381-396.
- Figueiredo, M.A.T., Leitão, J.M.N. and Jain, A.K. (1999): On fitting mixture models. *Lecture Notes in Computer Science: Energy Minimization Methods in Computer Vision and Pattern Recognition (EMMCVPR)*, Vol. 1654, pp. 54-69.
- Finnish Forest Association (2010): www.forest.fi (visited June 14, 2010).
- Finnish Forest Industries Federation (2010): www.forestindustries.fi (visited June 14, 2010).
- Forsyth, D.A. and Ponce, J. (2003): *Computer vision: A modern approach*. Prentice Hall, Upper Saddle River, NJ, USA.

Gate, L., Windle, W. and Hine, M. (1973): The relationship between gloss and surface microtexture of coatings. *Tappi*, Vol. 56, No. 3, pp. 61-65.

Haigh, J. (2002): *Probability models*. Springer-Verlag, London, UK.

Hansson, P. and Fransson, J. (2004): Color and shape measurement with a three-color photometric stereo system. *Applied Optics*, Vol. 43, No. 20, pp. 3971-3977.

Hansson, P. and Johansson, P.-Å. (2000): Topography and reflectance analysis of paper surfaces using a photometric stereo method. *Optical Engineering*, Vol. 39, No. 9, pp. 2555-2561.

Heikkilä, I. (1997): Viscoelastic model of paper surface compressibility. *Paperi ja Puu*, Vol. 79, No. 3, pp. 186-192.

Heikkilä, I., Oittinen, P., Saarelma, H. and Tuovinen, P. (1994): Dynaamisen kontaktisileyden mittausmenetelmä. *Paperi ja Puu*, Vol. 76, No. 6-7, pp. 399-402 (in Finnish).

Heintze, H.U. (1982): Press operation and gravure print quality. *Tappi*, Vol. 65, No. 6, pp. 109-112.

Heintze, H.U. and Gordon, R.W. (1979): Tuning of the GRI proof press as a predictor of rotonews print quality in the pressroom. *Tappi*, Vol. 62, No. 11, pp. 97-101.

Hendry, I.F. (1961): Some techniques for the assessment of coated art papers. *Tappi*, Vol. 44, No. 10, pp. 725-731.

Hirn, U., Lechthaler, M., Wind, E. and Bauer, W. (2009): Linear regression modelling of local print density in gravure printed SC paper. *Proc. Papermaking Research Symposium*, Kuopio, Finland, June 2009.

Hsu, B.-S. (1962): Distribution of depression in paper surface: a method of determination. *Brit. J. Applied Physics*, Vol. 13, pp. 155-158.

Härdle, W. and Simar, L. (2007): *Applied multivariate statistical analysis* (2nd ed.). Springer-Verlag, Berlin, Germany.

I3A (2007): CPIQ Initiative Phase 1 White Paper. Available at: http://www.i3a.org/wp-content/uploads/2008/03/cpiq_white_paper.pdf (visited April 9, 2010).

Ichikawa, I., Sato, K. and Ito, Y. (1962): A new concept of ink transfer equation. *Research Bulletin of the Government Printing Bureau, Japan*, No. 1, pp. 1-11.

IGT Testing Systems (2003): IGT Information leaflet W41. Available at: <http://www.igt.nl/GB/testmethods.asp> (visited April 14, 2010).

Ionides, G.N. (1984): The linting tendency of newsprint – a general review. *Paperi ja Puu*, Vol. 66, No.4, pp 298-306.

Janesick, J.R. (2001): *Scientific charge-coupled devices*. SPIE Press, Bellingham, WA, USA.

- Janssen, T.J.W.M. and Blommaert, F.J.J. (1997): Image quality semantics. *J. Imaging Science and Technology*, Vol. 41, No. 5, pp. 555-560.
- Johansson, P.-Å. and Hansson, P. (2004): Method of determining an illuminated surface. United States Patent No. 6,757,065 B1, June 2004. (Patent 511985, Sweden).
- Järnström, J., Ihalainen, P., Backfolk, K. and Peltonen, J. (2008): Roughness of pigment coatings and its influence on gloss. *Applied Surface Science*, Vol. 254, No. 18, pp. 5741-5749.
- Kajanto, I. (1989): The effect of formation on print quality with woodfree offset papers. *Nordic Pulp & Paper Research J.*, Vol. 4, No. 1, pp. 8-15.
- Kajanto, I. (1990): The effect of formation on absolute print unevenness in offset printing. *Paperi ja Puu*, Vol. 72, No. 6, pp. 600-610.
- Kajanto, I. (1991): *Effect of formation on print unevenness with uncoated woodfree papers*. PhD thesis, Helsinki University of Technology, Espoo, Finland.
- Kajanto, I., Laamanen, J. and Kainulainen, M. (1998): Paper bulk and surface. In: *Papermaking Science and Technology, Book 16, Paper Physics* (Niskanen, K., ed.), Fapet Oy, Jyväskylä, Finland. pp. 89-115.
- Kallmes, O. and Corte, H. (1960): The structure of paper – Part I: The statistical geometry of an ideal two dimensional fiber network. *Tappi*, Vol. 43, No. 9, pp. 737-752. – Errata: *Tappi*, Vol. 44, No. 6, 1961, p. 448.
- Kallmes, O., Corte, H. and Bernier, G. (1961): The structure of paper – Part II: The statistical geometry of a multiplanar fiber network. *Tappi*, Vol. 44, No. 7, pp. 519-528.
- Kapoor, S.G., Wu, S.M. and Pandit, S.M. (1978): A new method for evaluating printing smoothness of coated papers. *Tappi*, Vol. 61, No. 6, pp. 71-74.
- Karttunen, S.T.P. (1973): Structure and behaviour of a paper's surface in printing. In: *Trans. 5th Fund. Res. Symp.*, Cambridge, 1973, (Bolam, F., ed.), BPBIF, London, UK, 1976, pp. 544-560.
- Kay, S.M. (1993): *Fundamentals of statistical signal processing: Estimation theory*. Prentice Hall, Upper Saddle River, NJ, USA.
- Keelan, B.W. (2002): *Handbook of image quality*. Marcel Dekker, Inc., New York, USA.
- Kendall, M.G. (1938): A new measure of rank correlation. *Biometrika*, Vol. 30, No. 1/2, pp. 81-93.
- Kipphan, H. (ed.) (2001): *Handbook of print media*. Springer-Verlag, Berlin, Germany.
- Kraskov, A., Stögbauer, H. and Grassberger, P. (2004): Estimating mutual information. *Physical Review E*, Vol. 69, No. 6, pp. 066138-1-066138-16.

Kuparinen, T. (2008): *Reconstruction and analysis of surface variation using photometric stereo*. PhD thesis, Lappeenranta University of Technology, Lappeenranta, Finland.

Lauri, M. and Ihalainen, H. (2010): Measuring periodic patterns in noisy spatial data. *Proc. ENBIS – IMEKO TC21 Workshop on Measurement Systems and Process Improvement*, Teddington, UK, April 2010.

Leisti, T., Radun, J., Virtanen, T., Halonen, R. and Nyman, G. (2009): Subjective experience of image quality: Attributes, definitions and decision making of subjective image quality. *Proc. SPIE/IS&T Electronic Imaging, Image Quality and System Performance V*, San Jose, CA, USA, 2009, pp. 72420D-1-72420D-9.

Leskelä, M. (1998): Optical properties. In: *Papermaking Science and Technology, Book 16, Paper Physics* (Niskanen, K., ed.), Fapet Oy, Jyväskylä, Finland. pp. 117-137.

Levlin, J.-E. (1999): General physical properties of paper and board. In: *Papermaking Science and Technology, Book 17, Pulp and Paper Testing* (Levlin, J.-E. and Söderhjelm, L., eds.), Fapet Oy, Jyväskylä, Finland. pp. 137-161.

Lipshitz, H., Bridger, M. and Derman, G. (1990): On the relationships between topography and gloss. *Tappi J.*, Vol. 73, No. 10, pp. 237-245.

Lyne, B. (1976a): Measurement of the distribution of surface void sizes in paper. *Tappi*, Vol. 59, No. 7, pp.102-105.

Lyne, B. (1976b): Machine-calendering: implications for surface structure and printing properties. *Tappi*, Vol. 59, No. 8, pp.101-106.

Lyne, M.B. (1979): Multidimensional scaling of print quality. *Tappi*, Vol. 62, No. 11, pp. 103-107.

MacGregor, M.A. and Conners, T.E. (1987): Image analysis of an LWC paper reveals wire mark in the print density variations. *Tappi J.*, Vol. 70, No. 9, pp. 95-99.

MacGregor, M.A. and Johansson, P.-Å. (1990): Submillimeter gloss variations in coated paper – Part 1: The gloss imaging equipment and analytical techniques. *Tappi J.*, Vol. 73, No. 12, pp. 161-168.

MacGregor, M.A. and Johansson, P.-Å. (1991): Submillimeter gloss variations in coated paper. – Part 2: Studying “orange peel” gloss effects in a lightweight coated paper. *Tappi J.*, Vol. 74, No. 1, pp. 187-194.

MacGregor, M.A., Johansson, P.-Å. and Béland, M.-C. (1994): Measurement of small-scale gloss variation in printed paper – Topography explains much of the variation for one paper. *Proc. TAPPI Int. Printing and Graphic Arts Conf.*, Halifax, Canada, 1994, Tappi Press, Atlanta, GA, 1994, pp. 33-43.

McLachlan, G. and Peel, D. (2000): *Finite mixture models*. John Wiley & Sons, New York, USA.

- Mangin, P.J., Béland, M.-C. and Cormier, L.M. (1993): A structural approach to paper surface compressibility – Relationship with printing characteristics. In: *Trans. 10th Fund. Res. Symp.*, Oxford, 1993, (Baker, C.F., ed.), FRC/Pira International, Leatherhead, UK, 1993, pp. 1397-1427.
- Mangin, P.J. and Dubé, M. (2006): Fundamental questions on print quality. *Proc. SPIE/IS&T Electronic Imaging, Image Quality and System Performance III*, San Jose, CA, USA, 2006, (Cui, L.C. and Miyake, Y., eds.), pp. 605901-1-605901-12.
- Mangin, P.J. and Geoffroy, P. (1989): Printing roughness and compressibility: A novel approach based on ink transfer. In: *Trans. 9th Fund. Res. Symp.*, Cambridge, 1989, (Baker, C.F. and Punton, V.W., eds.), Mechanical Engineering Publications, London, UK, 1989, pp. 951-975.
- Mangin, P.J., Lyne, M.B., Page, D.H. and De Grâce, J.H. (1982): Ink transfer equations – Parameter estimation and interpretation. In: *Advances in Printing Science and Technology*, Vol. 16, (16th Int. Conf. of Printing Research Institutes), Miami, FL, 1981, (Banks, W.H., ed.), Pentech Press, London, UK, 1982, pp. 180-205.
- Martinez, W.L. and Martinez, A.R. (2008): *Computational statistics handbook with MATLAB* (2nd ed.). Chapman & Hall/CRC, Boca Raton, FL, USA.
- Mesic, B., Lestelius, M. and Engström, G. (2006): Occurrence and causes of uncovered areas in water-borne flexographic print on PE-extrusion-coated packaging papers. *Proc. TAPPI Printing and Graphic Arts Conf. (IPGAC)*, Cincinnati, OH, USA, 2006.
- Moss, P.A., Retulainen, E., Paulapuro, H. and Aaltonen, P. (1993): Taking a new look at pulp and paper: Applications of confocal laser scanning microscopy (CLSM) to pulp and paper research. *Paperi ja Puu*, Vol. 75, No. 1-2, pp. 74-79.
- Nabney, I.T. (2002): *Netlab: Algorithms for pattern recognition*. Springer-Verlag, London, UK, pp. 79-101.
- National Institute of Standards and Technology (2009): <http://syseng.nist.gov/VSC/jsp/index.jsp> (visited October 1, 2009).
- Nguyen, N.G. and Jordan, B.D. (1989): Overview of texture analysis of print and paper. *Paperi ja Puu*, Vol. 71, No. 8, pp. 933-944.
- Niskanen, K. (ed.) (1998): *Papermaking Science and Technology, Book 16, Paper Physics*. Fapet Oy, Jyväskylä, Finland.
- Niskanen, K. and Rajatora, H. (2002): Statistical geometry of paper cross-sections. *J. Pulp and Paper Science*, Vol. 28, No. 7, pp. 228-233.
- Nutbeem, C., Preston, J., Hiorns, A. and Husband, J. (2010): The influence of kaolin aspect ratio on offset printability. *Proc. TAPPI PaperCon*, Atlanta, USA, May 2010.

- Nyman, G., Radun, J., Leisti, T., Oja, J., Ojanen, H., Olives, J.-L., Vuori, T. and Häkkinen, J. (2006): What do users really perceive – probing the subjective image quality. *Proc. SPIE/IS&T Electronic Imaging, Image Quality and System Performance III*, San Jose, CA, USA, 2006, (Cui, L.C. and Miyake, Y., eds.), pp. 605902-1-605902-7.
- Oittinen, P., Halonen, R., Kokkonen, A., Leisti, T., Nyman, G., Eerola, T., Lensu, L., Kälviäinen, H., Ritala, R., Pulla, J. and Mettänen, M. (2008): Framework for modeling visual printed image quality from the paper perspective. *Proc. SPIE/IS&T Electronic Imaging 2008, Image Quality and System Performance V*, San Jose, CA, USA, 2008, pp. 68080L-1-68080L-12.
- Oittinen, P. and Saarelma, H.J. (1991): Application of information theory to characterize print quality. *Tappi J.*, Vol. 74, No. 8, pp. 197-203.
- Oittinen, P. and Saarelma, H. (1998): *Papermaking Science and Technology, Book 13, Printing*. Fapet Oy, Jyväskylä, Finland.
- O'Neill, G., Preston, J. and Charnock, J. (2010): Paper – the end of the road, or dawn of a new era. *Proc. TAPPI PaperCon*, Atlanta, USA, May 2010.
- Papoulis, A. (1990): *Probability & Statistics*. Prentice-Hall, Englewood Cliffs, NJ, USA.
- Parker, J.R. (1965): Effects of dry pressing on printing properties of uncoated paper webs. In: *Trans. 3rd Fund. Res. Symp.*, Cambridge, 1965, (Bolam, F., ed.), BPBMA, London, UK, 1966, pp. 959-976.
- Parker, J.R. (1971): Development and applications of a novel roughness tester. *Tappi*, Vol. 54, No. 6, pp. 943-949.
- Parker, J.R. (1973): Fundamental paper properties in relation to printability. In: *Trans. 5th Fund. Res. Symp.*, Cambridge, 1973, (Bolam, F., ed.), BPBIF, London, UK, 1976, pp. 517-543.
- Phillips, P.J., Moon, H., Rizvi, S.A. and Rauss, P.J. (2000): The FERET evaluation methodology for face-recognition algorithms. *IEEE Trans. Pattern Analysis and Machine Intelligence*, Vol. 22, No. 10, pp. 1090-1104.
- Pratt, W.K. (2001): *Digital image processing* (3rd ed.). John Wiley & Sons, New York, USA.
- Preston, J. (2009): The surface analysis of paper. In: *Trans. 14th Fund. Res. Symp.*, Oxford, 2009, (I'Anson, S.J., ed.), FRC, Bury, UK, 2009, pp. 749-838.
- Preston, J., Bollström, R., Nylander, K., Toivakka, M. and Peltonen, J. (2008): A new test method to measure dynamic contact in a printing nip for rotogravure papers. *Proc. 35th Int. Research Conf. IARIGAI*, Valencia, Spain, 2008, pp. 147-153.
- Pulla, J. (2007): *Jury assessment as reference for technical measurements of image quality*. Master's thesis, Tampere University of Technology, Tampere, Finland.
- Ray, R., Birk, J. and Kelley, R.B. (1983): Error analysis of surface normals determined by radiometry. *IEEE Trans. Pattern Analysis and Machine Intelligence*, Vol. 5, No. 6, pp. 631-645.

- Richardson, S. and Green, P.J. (1997): On Bayesian analysis of mixtures with an unknown number of components. *J. Royal Statistical Society, Series B*, Vol. 59, No. 4, pp. 731-792.
- Roberts, S.J., Husmeier, D., Rezek, I. and Penny, W. (1998): Bayesian approaches to Gaussian mixture modelling. *IEEE Trans. Pattern Analysis and Machine Intelligence*, Vol. 20, No. 11, pp. 1133-1142.
- Roehr, W.W. (1955): Effect of smoothness and compressibility on the printing quality of coated paper. *Tappi*, Vol. 38, No. 11, pp. 660-664.
- Rycobel Group (2010): Print simulation tester. Brochure available at: <http://www.rycobel.be/pdf/lab0/PST.pdf> (visited April 9, 2010).
- Ryynänen, K. (2006): *Measurement of paper surface roughness with imaging*. Master's thesis, Tampere University of Technology, Tampere, Finland.
- Saarelma, H.J. and Oittinen, P.T. (1993): Paper and print noise as limiting factors of information capacity. In: *Trans. 10th Fund. Res. Symp.*, Oxford, 1993, (Baker, C.F., ed.), FRC/Pira International, Leatherhead, UK, 1993, pp. 351-365.
- Safadi, T. (1992): The Pira printing smoothness tester. *Paper Technology*, Vol. 33, No. 1, pp. 28-31.
- Sampson, W.W. (2001a): The structural characterisation of fibre networks in papermaking processes – a review. In: *Trans. 12th Fund. Res. Symp.*, Oxford, 2001, (Baker, C.F., ed.), FRC, Bury, UK, 2002, pp. 1205-1288.
- Sampson, W.W. (2001b): Comments on the pore radius distribution in near-planar stochastic fibre networks. *J. Materials Science*, Vol. 36, No. 21, pp. 5131-5135.
- Sampson, W.W. and Urquhart, S.J. (2008): The contribution of out-of-plane pore dimensions to the pore size distribution of paper and stochastic fibrous materials. *J. Porous Materials*, Vol. 15, No. 4, pp. 411-417.
- Scott, D.W. (1992): *Multivariate density estimation: Theory, practice and visualization*. John Wiley & Sons, New York, USA.
- Seber, G.A.F. (1984): *Multivariate observations*. John Wiley & Sons, New York, USA.
- Sonka, M., Hlavac, V. and Boyle, R. (1999): *Image processing, analysis, and machine vision* (2nd ed.). PWS Publishing, Pacific Grove, CA, USA.
- Stout, K.J. and Blunt, L. (1995): Nanometers to micrometers: three-dimensional surface measurement in bio-engineering. *Surface and Coatings Technology*, Vol. 71, No. 2, pp. 69-81.
- Stout, K.J. and Blunt, L. (2000): *Three-dimensional surface topography* (2nd ed.). Penton Press, London, UK.

Stuart, A., Ord, K. and Arnold, S. (1999): *Kendall's advanced theory of statistics, Vol. 2A: Classical inference & the linear model* (6th ed.). Arnold, London, UK.

Sung, Y.J., Ham, C.H., Kwon, O., Lee, H.L. and Keller, D.S. (2005): Applications of thickness and apparent density mapping by laser profilometry. In: *Trans. 13th Fund. Res. Symp.*, Cambridge, 2005, (I'Anson, S.J., ed.), FRC, Bury, UK, 2005, pp. 961-1007.

Suontausta, O. (1999): End-use properties of printing papers. In: *Papermaking Science and Technology, Book 17, Pulp and Paper Testing* (Levlin, J.-E. and Söderhjelm, L., eds.), Fapet Oy, Jyväskylä, Finland. pp. 183-216.

Thévenaz, P. and Unser, M. (1998): An efficient mutual information optimizer for multiresolution image registration. *Proc. IEEE Int. Conf. Image Processing (ICIP)*, Chicago, IL, USA, 1998. pp. 833-837.

Thomas, T.R. (ed.) (1982): *Rough Surfaces*. Longman, London, UK.

To, M., Lovell, P.G., Troscianko, T. and Tolhurst, D.J. (2008): Summation of perceptual cues in natural visual scenes. *Proc. of the Royal Society B*, Vol. 275, pp. 2299-2308.

Tollenaar, D. and Ernst, P.A.H. (1969): Uneven ink transfer on smooth surfaces. In: *Advances in Printing Science and Technology*, Vol. 6, (10th IARIGAI Conf.), Krems, Austria, 1969, (Banks, W.H., ed.), Pergamon Press, Oxford, NY, USA, 1971, pp. 139-149.

Vaarasalo, J. (1999): Optical properties of paper. In: *Papermaking Science and Technology, Book 17, Pulp and Paper Testing* (Levlin, J.-E. and Söderhjelm, L., eds.), Fapet Oy, Jyväskylä, Finland. pp. 163-181.

Vartiainen, J. (2007): *Measuring irregularities and surface defects from printed patterns*. PhD thesis, Lappeenranta University of Technology, Lappeenranta, Finland.

Viola, P. and Wells, W. M. (1997): Alignment by maximization of mutual information. *Int. J. Computer Vision*, Vol. 24, No. 2, pp. 137-154.

Walker, W.C. and Fetsko, J.M. (1955): A concept of ink transfer in printing. *American Ink Maker*, Vol. 33, No. 12, pp. 38-44 and 69-71.

Wolberg, G. (1990): *Digital image warping*. IEEE Computer Society Press, Los Alamitos, CA, USA.

Wågberg, P. and Johansson, P.-A. (1993): Surface profilometry – a comparison between optical and mechanical sensing on printing papers. *Tappi J.*, Vol. 76, No. 12, pp. 115-121.

Publications

Publication I

Lähdekorpi, M., Ihalainen, H. and Ritala, R. (2006): Using image registration and alignment to compare alternative 2D measurements. *Proc. XVIII IMEKO World Congress*, Rio de Janeiro, Brazil, September 2006.

© 2006 IMEKO. Reprinted, with permission, from Proceedings of the IMEKO XVIII World Congress. Publication available at www.imeko.org.

USING IMAGE REGISTRATION AND ALIGNMENT TO COMPARE ALTERNATIVE 2D MEASUREMENTS

Marja Lähdekorpi, Heimo Ihalainen and Risto Ritala

Institute of Measurement and Information Technology, Tampere University of Technology, Tampere, Finland
marja.lahdekorpi@tut.fi heimo.ihalainen@tut.fi risto.ritala@tut.fi

Abstract: We present in this paper a novel method for comparing alternative 2D measurements. The method is based on a new image registration algorithm developed for the automatic registration and alignment of randomly textured image data. Our aim in the algorithm development has been to enable fast registration of the measured 2D property maps without the need for special registration marks. To improve robustness, the maps are registered in two steps; the first step exhibits plain translation and the second phase iteratively refines the transformation estimate. Sub-pixel registration accuracy is achieved. Several experiments have been conducted showing that the algorithm is able to register various 2D property maps successfully. After the registration we align the alternative 2D measurements. This enables the comparison and statistical joint analysis of several 2D property maps measured from the same target area. The high amount of independently measured data points in the property maps provides a firm statistical ground for conclusions. We have used the new registration algorithm to align various 2D surface profile measurements of paper and board. The analysis of the aligned measurements has confirmed the feasibility of our registration method and revealed fundamental differences between the measurement devices.

Keywords: image registration, 2D profile measurement

1. INTRODUCTION TO PROPOSED METHOD

An increasing number of applications today make use of photographic imaging, laser scanning, and other measurements that produce 2D property maps (images). For example, 2D maps of surface topography offer promising ways to characterize surface structure and smoothness. Some of the topography measurements are probing directly the surface height but are slow whereas other methods are less direct but fast. In this paper we address the problem of analyzing the correspondence and accuracy of indirect 2D measurement methods when direct measurements are available as a reference. Our interest is in cases when the image resolution varies between the measurement methods and when the measurement devices do not automatically provide aligned images but alignment must be achieved based on the content of the measured images.

Image registration and alignment means that a set of 2D measurements of a sample are overlaid so that the pixels

with the same coordinates in the measured images correspond to the same point in the sample. Image registration has had applications in cartography already when the work was performed by hand and eye. In last years, computational methods for automatic registration and alignment have been developed in several application areas; stereo vision, stereo cartography, close-range photogrammetry, medical imaging, image fusion and super-resolution [1, 2]. The computational load is quite suitable for modern personal computers.

We have developed a new image registration procedure that enables the alignment of textured 2D property maps with sub-pixel accuracy. The idea of using separate pixel clusters is similar to that presented in [3]. The main advantage of the new method is its robust automatic operation, even in cases when the maps have been acquired by different devices. Special registration marks are not needed because the method makes use of the texture contained in the data. The similarity measure used in the procedure is the 2D cross-correlation function.

The possibility to use aligned images provides considerable added value to image based measurement applications. It is practical to compare several alternative measurements of the same quantity. The comparison provides valuable information about the differences and similarities between the measurement devices and enables calibration. Sometimes it is useful to measure the same area several times with the same instrument to analyze noise. It is also possible to align multiple measurement arrays of different quantities measured from the same area to get information about the interactions of the variables.

We have applied image registration and alignment to compare alternative surface topography measurement methods. In our approach the same target area is first measured with all the methods. Next the data matrices are aligned together at sub-pixel accuracy using the new registration method introduced in this work. The dependencies between the aligned maps and their quality parameters can then be analyzed by multivariate statistical methods [4, 5]. Property maps – including surface topography maps – typically have a large number of independently measured data points, which provides a firm statistical ground for conclusions. Even low correlations and relationships are of significant statistical confidence.

This paper is organized as follows. Our new automatic image registration and alignment procedure will be described in Section 2. The measurement data analyzed in this work will be introduced in Section 3. Section 4 will present the methods used to analyze the aligned 2D measurements and introduce the results of the analysis. Section 5 will conclude the presentation.

2. AUTOMATIC IMAGE REGISTRATION AND ALIGNMENT

Transforming two images – the reference image and the input image – into the same coordinates consists of registration and alignment. Registration is the phase where a set of corresponding points (or features) are found from the two images and a transformation is estimated based on these points. At the alignment phase the transformation is applied to all the coordinates of the input image in order to overlay them with those of the reference image. Alignment involves interpolation to compute the input image values in the new, non-integer, coordinates. Accurate alignment of measured images is a pre-requisite for reliable joint analysis.

We have created a new image registration and alignment procedure for 2D measurements that contain random texture. The registration phase will be described in subsection 2.1 and alignment in subsection 2.2. Our method has the following three requirements: a) the areas measured with different instruments must overlap; b) the measurements have to correlate sufficiently with each other to facilitate the registration; c) the 2D sampling frequency of at least one of the measurements must be high enough to enable the interpolation of the measured values between the grid points.

2.1. Image Registration

The primary approach to register maps with random texture uses point mapping [1] which is also the basis of our method. In point mapping, control points are first selected from the reference map. Small areas around the control points are then selected and similar areas are searched in the input image(s). We have used 2D cross-correlation function as the similarity measure in the point search. The exact points of maximum similarity are interpolated from the 2D cross-correlation surface to achieve sub-pixel accuracy.

We have concentrated on making all the registration operations automatic. A priori knowledge about the nature of misregistration between the reference and input images has been essential in this work. The images acquired from the different measurement devices are known to be translated and moderately rotated with respect to each other. There may also be minor scale differences and slight errors in the orientation of the coordinate axes of the devices, which causes obliqueness. Hence affine transformation [6] has been chosen to map the input to the reference image.

Robustness is necessary for an image registration algorithm to be automated. Therefore each pair of images is registered in two phases: a coarse translation estimation phase and an iterative refinement of the transformation

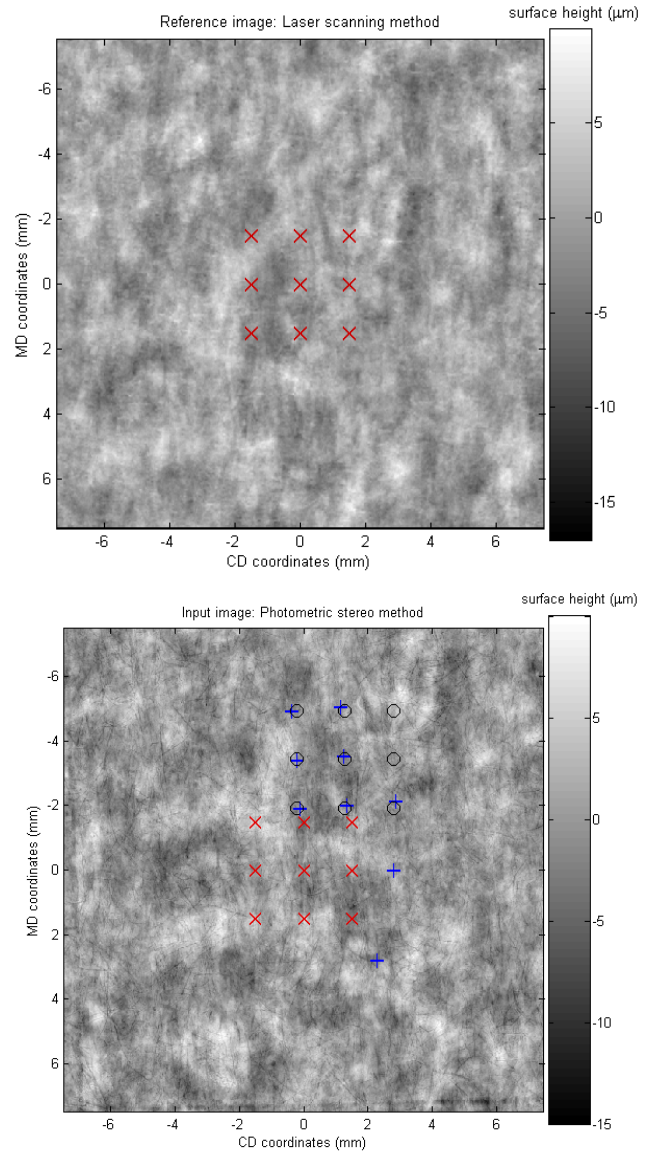


Fig. 1. First phase of image registration. Upper: reference topography image and search points (x). Lower: input image with predicted (x), found (+) and chosen (o) matching points.

estimate. In order to estimate the required translation within a moderate delay, the first phase employs a small number of control points. They are placed around the center of the reference image, as illustrated in the upper part of Fig. 1. Small areas around the control points are selected and similar areas are located automatically in the input image as the matching points. The lower part of Fig. 1 shows the matching points located by the algorithm as blue plus marks on the input image. It can be seen that not all of the points indicate a similar translation. An approximation for the translation in horizontal and vertical directions is computed as a weighted median value of the nine translation estimates. It is indicated in the lower part of Fig. 1 by the black circles.

The use of a large search area, which is necessary in the beginning, often causes false matches. However, the success of the registration depends critically on the reliability of the initial transformation estimate. It is therefore verified by cluster analysis that more than half of the points found indicate, within a small deviation, the same amount of

translation between the reference and input images. In Fig. 1, seven of the nine search points show coherent results. The translations indicated by these seven points thus form a dense cluster around the weighted median based translation estimate when plotted in coordinate axes. If the matching points located by the algorithm are very much scattered around the map, no such cluster can be found and the registration is attempted again a few times with slightly adjusted search parameters.

Provided the first phase of the registration algorithm completes successfully, the latter phase then iteratively refines the transformation estimate according to further control points. At each iteration step, a set of new control points is automatically selected from the reference image. The locations of these points in the input image are predicted based on the latest transformation estimate. The exact locations are determined by the search procedure similar to that of phase one, but with a very small search area size. This efficiently constricts the computation time.

The grid of control points selected on the latter registration phase expands towards the corners of the reference image, which improves the overall registration accuracy. When the control point set finally spans the whole joint area of the reference and input images, the point search is terminated. A global affine transformation is fitted between the matching control points by a weighted least squares method in which the effect of abnormal control point pairs is minimized. The alignment accuracy achieved depends both on the accuracy of image registration and on the accuracy of transformation fitting [7]. If the transformation is correct and thus describes the warping required to convert the images into the same coordinates, the error can be satisfactorily approximated by the transformation fitting error. Our experiments, covering 89 pair-wise registrations of multimodal surface topography measurements of paper and board, imply that affine transformation is very suitable for our application. The transformation fitting error has remained below 0.1 pixels in the experiments.

2.2. Image Alignment

The transformation estimated at the registration phase is finally applied to the input image. This provides the geometrical alignment of the reference and input images. The coordinates of the input image are first warped to overlay them with those of the reference image. The input image must then be interpolated to evaluate the pixel values at the warped non-integer coordinates. Fig. 2 shows examples of the aligned surface topography maps of a cardboard sample. They have been selected from three different measurements that will be described in Section 3.

When the images to be aligned have different spatial resolutions, interpolation requires particular attention. When possible, it is advisable to select the reference image to be the one with the lower resolution. This minimizes the amount of artificial interpolated data in the result. We will analyze the effects of interpolation in Section 4.

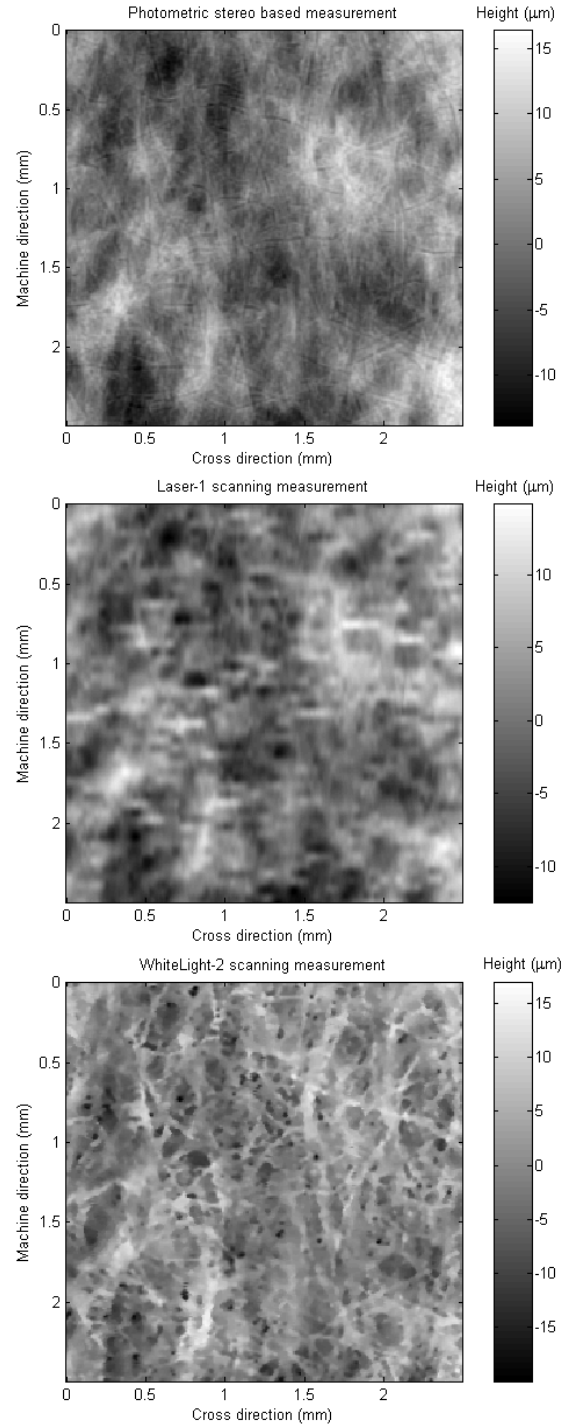


Fig. 2. Examples of aligned surface topography maps measured with different devices: Photometric stereo based device (top), Laser-1 scanner (middle) and WhiteLight-2 scanner (bottom). A small area has been selected from the total aligned map to show fine details.

3. MEASUREMENT DATA

The image data analyzed in this presentation is from five surface topography measurement devices. One of them, the photometric stereo based device, produces the topography map a couple of orders of magnitude faster than the other devices. It is also the only indirect method applied since it recovers the surface topography map from digital photographic images. The other four measurement devices

are optical profilometers that produce the surface height values by direct scanning, using either red laser light or white light. The two laser scanners (Laser-1 and Laser-2) differ from each other in the z-directional resolution and measuring range. The two scanners that apply white light are equipped with different scanning sensors: the z-directional measuring range of the first sensor (later referred to as WhiteLight-1) is ten times larger than that of the second (WhiteLight-2). Table 1 summarizes the main properties of the images acquired by each device.

Table 1. Properties of surface topography images acquired by each measurement method.

Measurement device	Image size, x by y (mm)	Resolution, [x, y] (points / mm)
Photometric stereo	15 by 15	[137, 137]
Laser-1 scanning	15 by 15	[100, 20]
Laser-2 scanning	16 by 16	[100, 20]
WhiteLight-1 scanning	16 by 16	[100, 100]
WhiteLight-2 scanning	16 by 16	[100, 100]

The different devices have been used to measure the surface topography of coated and uncoated paper and cardboard samples. This article presents the analysis results for an uncoated cardboard sample.

4. ANALYSIS AND RESULTS

A multivariate image is constructed by stacking the aligned maps on top of each other. Each measured map thus becomes a variable in the three-way array. In this section, statistical analysis tools will be applied to the multivariate surface topography image to infer about the inter-relationships between the measurements. Subsection 4.1 will analyze the information obtained by combining all the five different topography measurements of the same surface. Principal component regression will be applied to reveal the specific features of each measurement device. In subsection 4.2, the differences and similarities of the measurement devices will be examined through comparing their frequency responses.

4.1. Principal Component Regression

Principal component analysis (PCA) is a multivariate statistical analysis method that decomposes the original set of variables into orthogonal and – when normally distributed – statistically independent linear combinations [4]. These linear combinations, i.e., principal components, are organized so that the first component explains the largest part of the total variability of the original data, the second component explains the second largest part, and so on.

We have evaluated the principal components of the multivariate image consisting of the five aligned surface topography maps of an uncoated cardboard sample. Prior to PCA each measurement (i.e. variable) has been normalized to have zero mean and a standard deviation equal to unity. This gives all variables equal opportunities to contribute to

the model. To see the small-scale specialties of each measurement, we have chosen a 2.5 mm by 2.5 mm area from the multivariate image for the analysis. The resulting loading vectors, \mathbf{p} , of each principal component are shown in Table 2. These values express the weight of each variable in the principal component scores.

Table 2. Principal component loading values for the five measurements.

Variable	p1	p2	p3	p4	p5
Photometric stereo	0.45	0.59	-0.12	-0.10	-0.65
Laser-1 scanning	0.46	0.42	-0.25	-0.02	0.74
Laser-2 scanning	0.43	-0.10	0.87	-0.19	0.08
WhiteLight-1 scanning	0.43	-0.59	-0.40	-0.55	-0.08
WhiteLight-2 scanning	0.46	-0.34	-0.09	0.81	-0.10

The first principal component is interpreted as the noise-free estimate of the measured quantity given all the measurements. As shown in Table 2, the loading values for the first principal component are almost equal. The first loading vector, $\mathbf{p1}$, has also been calculated for the total common area (13 mm by 12 mm) of the aligned measurements and the result is practically equal to that presented in Table 2. This is a very significant result. It means that the true surface topography of the cardboard sample can be best estimated by computing the point-wise mean of the measured topography maps. The mean image on the small observation area is presented in Fig. 3. The result also implies that all the measurement devices applied in this research are equally accurate. Based on the eigenvalues of the correlation matrix of the original variables, the first principal component explains approximately 80 % of the total variability of the multivariate data.

Although certain deductions about principal components 2-5 can be made from the loading values presented in Table 2, the interpretation is not as straightforward as that of the first component. Instead of PCA, we have concentrated on regression analysis to examine the differences between the measurement devices. The basis of our regression analysis is the result obtained above by PCA: the mean of

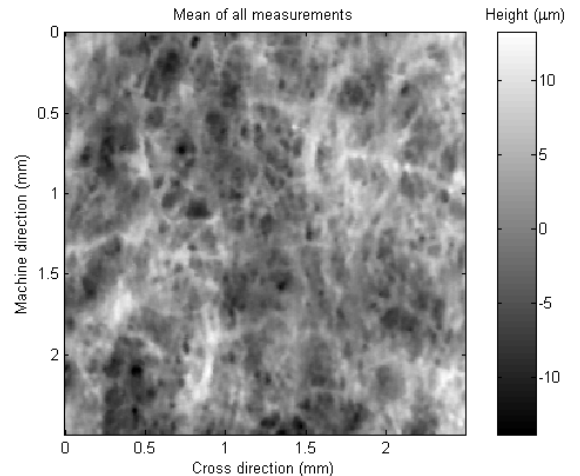


Fig. 3. Mean of all surface topography measurements of the cardboard sample on the selected 2.5 mm by 2.5 mm area.

the five measurements presents the surface topography variations detected by the five devices together. It can thus be expected that the mean of four measurements also describes the true surface topography, but less accurately. By evaluating the difference between the latter mean and the measurement that is left out of the mean calculation, we can reveal the errors and peculiarities characteristic of that measurement.

In the principal component regression analysis we have taken one surface topography map at a time and computed the least-squares regression coefficient to predict this map with the mean of the four remaining maps. Since the only explanatory variable in this regression problem is the mean value, the predictions of the different maps are very similar to each other. The correlation coefficients between the measurements and their predictions vary from 0.76 to 0.84. The most informative results of the regression analysis are the difference images calculated by subtracting the prediction from the original 2D measurement. Fig. 4 shows this image for the photometric stereo based measurement device. This example has been selected because it reveals the most significant detail among all the devices when compared to the original measurement images. The photometric stereo based system is also the only indirect method applied to the surface topography measurement.

The photometric stereo method seems to discern the fibrous structure of the sample surface with a higher precision than the other methods. However, it has been observed that the measurements acquired by the photometric stereo device tend to present the fibers as impressions rather than elevations, as also depicted by Fig. 2. The locations and orientations of the fibers can thus be deduced from this measurement but the surface height values at these locations are misleading. The WhiteLight-2 profilometer seems to locate the pores on the sample surface particularly well (see Fig. 2). The other white light based profilometer applies a coarser scanning sensor and hence detects less detail than WhiteLight-2. The laser profilometer measurements produce the least structured difference images when compared to the mean of the other measurements. The most discernible features in these images are the slight cross-directional errors of Laser-1 measurement which are also shown in the middle part of Fig. 2

4.2. Spectral Analysis

The spectra of the surface topography measurements provide information about the bandwidths of the signal and of the measurement devices. We have concluded, by looking at the large scale samples of the measured topography maps, that the WhiteLight-2 device has the widest bandwidth of the compared methods. It can thus be used as a reference to assess the loss of information at the interpolation that is applied in image alignment. We have computed the 2D spectra [8] with the fast Fourier transform (FFT) based 2D Welch method for the original and aligned surface topography measurements. Fig. 5 presents the 2D spectra for the case where the WhiteLight-2 measurement has been aligned with the photometric stereo based measurement. The corresponding cross-directional 1D spectra are presented in

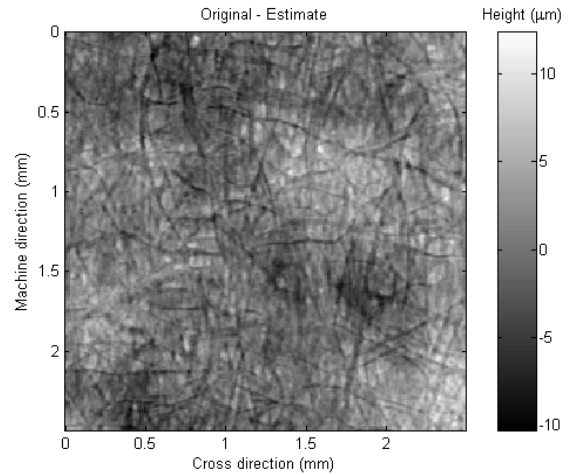


Fig. 4. Difference between the original topography measurement and its regression-based estimate for the photometric stereo method on the same area as the images presented in Figures 2 and 3.

Fig. 6. These pictures clearly show that the alignment affects the spectrum only slightly in comparison to the difference of the spectra of the measurement methods. It is also obvious from the spectra that the photometric stereo based measurement does not contain the high-frequency components of the surface topography features. This will affect the parameters calculated based on this measurement.

Spectral analysis is important because most parameters describing surface roughness are related to the spectrum and can in fact be computed from the spectrum. Multivariate spectral analysis can be performed on the spectra of the aligned maps to further infer about the differences of the measurement methods. This will be one of the subjects of our future work.

5. CONCLUSIONS

In this work we have introduced a new image registration procedure and indicated its feasibility in multivariate image analysis. The focus in our work has not been on inventing completely new image registration methods but to build a robust automatic registration procedure for randomly textured data using the methods that best suit the application. The developed image registration method has proved itself quite robust in several practical examples. It tends to achieve a satisfactory registration result whenever the initial search parameters entered to the algorithm are reasonable enough.

We have applied multivariate statistical analysis to the aligned surface topography maps measured from paper and cardboard and shown some of the results for an uncoated cardboard sample. The objectives of the analysis have been two-fold.

Firstly, the comparison of surface topography measurements has aimed at evaluating the information captured by the alternative measurement methods. Principal component analysis has indicated that, given the multivariate 2D measurement, the best estimate of the true surface topography map is obtained by computing the mean

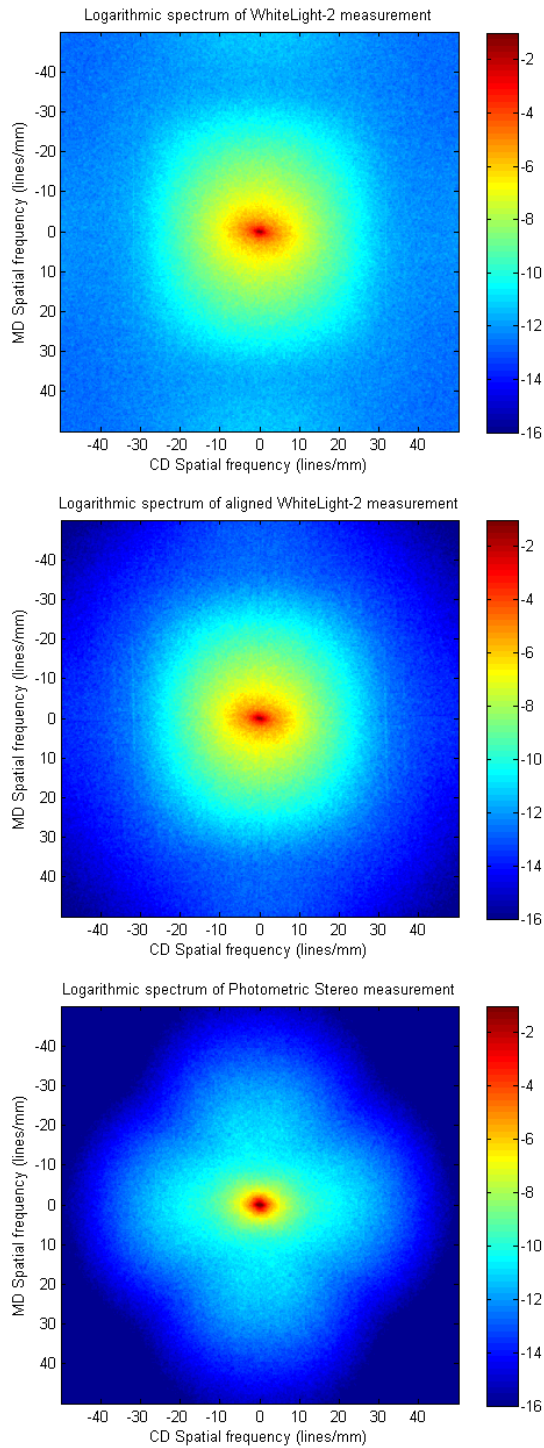


Fig. 5. Logarithmic 2D power spectra of the original WhiteLight-2 (top) and photometric stereo based measurement (bottom). The middle spectrum is from the WhiteLight-2 measurement aligned with the photometric stereo measurement.

of the aligned measurements at each point. This result is also a strong indication of the success of our image registration procedure. Regression analysis has revealed the specific information captured by each individual measurement system. Spectral analysis has also been used to examine the differences and similarities of the measurements.

Secondly, we have analyzed the correspondence between a fast but indirect 2D profile measurement method and slow scanning methods that are available as reference. The

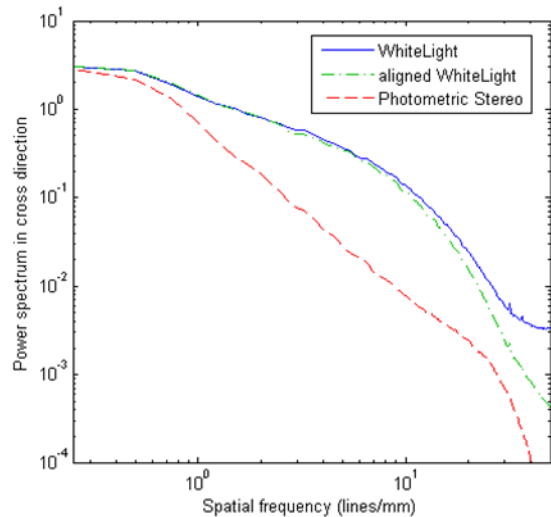


Fig. 6. Comparison of the cross-directional spectra of original and aligned WhiteLight-2 and photometric stereo based measurements.

objective has been to assess the accuracy of the surface topography measurement produced by the fast method and to compare it with the information gathered by the reference devices. The analysis has shown that the bandwidth of the fast measurement does not compare to that of the highest resolution reference measurement. However, the fast device has been found to expose the fibrous structure of the sample surface with considerably higher accuracy than the other devices.

REFERENCES

- [1] L. Brown, "A survey of image registration techniques," *ACM Computing Surveys*, Vol. 24, No. 4, pp. 325-376, Dec. 1992.
- [2] J. P. W. Pluim, and J. M. Fitzpatrick, "Image registration," (special number of image registration), *IEEE Transactions on Medical Imaging*, Vol. 22, No. 11, pp. 1341-1343, Nov. 2003.
- [3] R. J. Althof, M. G. J. Wind, and J. T. Dobbins, "A rapid and automatic image registration algorithm with subpixel accuracy," *IEEE Transactions on Medical Imaging*, Vol. 16, No. 3, pp. 308-316, June 1997.
- [4] P. Geladi, and H. Grahn. *Multivariate Image Analysis*. John Wiley & Sons, 1996.
- [5] M. Bharati, and J. F. MacGregor, "Texture analysis of images using principal component analysis," *Proceedings of the SPIE - Process Imaging for Automatic Control*, Boston, MA, Nov. 2000.
- [6] G. Wolberg, *Digital Image Warping*. IEEE Computer Society Press, 1990.
- [7] D. Robinson, and P. Milanfar, "Fundamental performance limits in image registration," *IEEE Transactions on Image Processing*, Vol. 13, No. 9, pp. 1185-1199, Sep. 2004.
- [8] W. K. Pratt. *Digital Image Processing*. John Wiley & Sons, 1991.

Publication II

Mettänen, M., Ihalainen, H. and Ritala, R. (2008): Alignment and statistical analysis of 2D small-scale paper property maps. *Appita Journal*, Vol. 61, No. 4, pp. 323-330.

© 2008 Appita. Reprinted, with permission, from Appita Journal.

Alignment and statistical analysis of 2D small-scale paper property maps

MARJA R. METTÄNEN¹, HEIMO A.T. IHALAINEN² AND RISTO K. RITALA³

SUMMARY

The relationship between printability and paper structure based on registration, alignment and analysis of 2D property maps of unprinted and printed paper has been studied. Surface topography, optical formation and intensity of the print were all measured and the point-by-point probabilistic interdependencies of these properties statistically characterised. The 2D measurements of the paper properties and the print quality were aligned with a point-mapping based registration procedure. This alignment provides a large amount of multivariate pointwise data and thus permits reliable estimates of the joint probability density functions (pdfs) that are efficiently parameterized through Gaussian mixtures. Assuming the interdependency to be only probabilistic and non-Gaussian, it is possible to derive full conditional pdfs instead of regression models and to investigate how the shape of the conditional pdfs – e.g. tails – depends on the conditioning variable. These pdfs were used to form anomaly maps that locate defects (for example, print defects) and their causes. The methods and the usefulness of the analyses were demonstrated with results on newsprint samples.

KEYWORDS

Image registration, multivariate statistical analysis, paper properties, printability, joint probability distributions

INTRODUCTION

Small-scale 2D measurements of paper produce considerable amount of useful information about the physical parameters of the fibre network and paper surface properties (1-3). The measurements are

made with various devices and sensor matrices and thus the sets of property maps obtained typically have neither the same size nor the same resolution. To take full advantage of the 2D measurements acquired from the same area of a paper sheet, methods for image registration and alignment are required in order to overlay the measured images so that the pixels with the same physical coordinates in the different images, corresponding to the same part of the sample, can be compared. This is a pre-requisite for reliable joint analysis of the maps. The idea of aligned image analysis has been used in paper physics recently by, e.g. Sung et al. (4) who computed maps of apparent density of paper from aligned 2D measurements of thickness and formation. A wide range of material characterization and analysis applications could possibly benefit from aligned multi-channel maps that typically contain a large number of independently measured data points, as this would set up a firm basis for statistical analysis of the measured properties. Analyzing the microstructure of paper through the aligned measurement maps is further motivated by the fact that the physical characteristics of paper are associated with printability and with the quality of the final printed product (5-7). Previous studies utilizing aligned images have shown this using correlation and regression analysis (8-10). There is no questioning of the significance of these results, but it can be expected that traditional statistical analysis methods, such as regression analysis, do not provide full information about the dependencies between measured print quality and the structural parameters because the dependencies are statistical and non-Gaussian. Regression provides the expected value of the target variable given the values of the explanatory variables but neglects prediction uncertainty that tends to be large due to the effects of the printing process and unmeasured properties of paper. The key idea in the current work is to approach the dependencies through the full joint probability densities of the measured properties, as these provide not only regression

but full parametric descriptions of the statistical relationships. The long-term goal in this research is to gain understanding and to generate models of the relationships between the statistical properties of print quality and the measurable physical structure of unprinted paper so that paper quality can be effectively monitored.

The intense development of image acquisition and analysis techniques has led to a wide variety of registration and alignment tools in application areas such as remote sensing, image fusion, stereo vision, super-resolution, close-range photogrammetry, and medical imaging (11). Various image registration methods have been reported to assist in automatic image registration, e.g. (12,13), however none of the methods published so far have been readily applicable to the automatic registration of randomly textured image data sets (such as the 2D small-scale maps of paper structure) that contain no special registration marks. The authors have previously developed a new method for that purpose and verified its usability by several registration experiments with multimodal 2D measurement data (14).

A methodology for the multivariate statistical analysis of aligned 2D property maps of paper measured before and after printing is proposed. A block diagram of the analysis procedure is presented in Figure 1. After aligning the measured small-scale maps accurately it is possible to compare the measured properties point-by-point and gain fundamental information about the physical mechanisms determining the quality of paper and print. It can be expected that, however accurate the measurements, there are no deterministic point-to-point relationships between print quality and the structural properties. Instead, the relationships are probabilistic and thus they are appropriately described with the full joint probability distributions of the measured properties (15). The joint distributions are typically clearly different from multivariate Gaussian and thus cannot be summarized with one expectation vector and covariance matrix. On the other hand, distribution models that assume the third, fourth or higher

¹Research Scientist, PhD Student and corresponding author (marja.mettanen@tut.fi), ²Laboratory Engineer, ³Professor

Department of Automation Science and Engineering
Tampere University of Technology
P.O. Box 692, FI-33101 Tampere, Finland

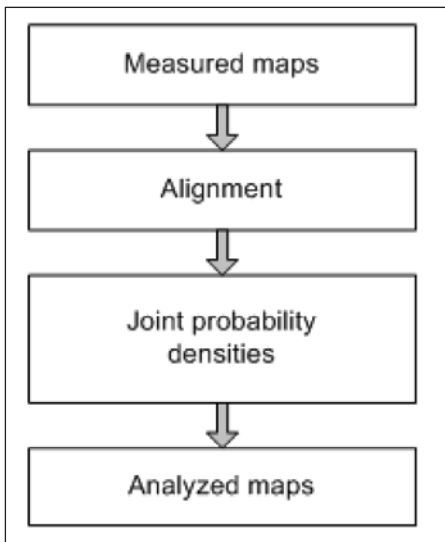


Fig. 1 Multivariate analysis procedure.

moments fixed would be only numerically solvable. An alternative description of the distributions with histograms or Gaussian mixture models (GMM) (16) can be adopted. The GMM approach is particularly attractive for two main reasons. Firstly, GMM can condense the huge amount of data into a fairly small set of parameters. Secondly, this parametric representation generally enables the analytical calculation of conditional probability density functions (pdfs) of individual quality properties. It should be noted however, that in some cases the very fine details in the tails of the pdfs can be effectively analyzed only with histograms, as is shown later. The large number of independently measured data points in the multivariate images provides a strong basis for pdf estimation and statistical inference. It is possible to examine the shape of the distributions and use the joint pdf models to derive anomaly maps of the measured properties. Anomaly maps reveal the points and areas that deviate most strongly from the typical statistical behavior, thus providing essential information of, for example, print defects and their origins.

The authors have previously examined the correspondence of different paper surface topography measurement devices (14) through multivariate image analysis. The research described here goes further in the analysis of paper structure and reports experiments with 2D measurements of surface topography, optical formation and print quality. Similar research has been conducted before but with only 1 mm resolution (17). The resolution in the property maps analysed here is 0.01 mm. The example cases present the analysis of

newsprint samples that have been printed with a sheet-fed offset press.

The body of the paper is organized as follows. First a description of the new automatic image registration method is given and its requirements and accuracy discussed. The property maps measured from the samples both before and after printing are then introduced. The multivariate statistical analysis method employing joint probability densities and the application of the tools to the aligned maps is then described. Finally, results from the analysis are presented and the information provided by these analytical methods discussed.

ALIGNMENT OF MEASURED MAPS

The registration and alignment of two images, one a reference and the other referred to as input, describes the process whereby the input image is spatially transformed to overlay it with the reference image. The image registration procedure consists of two phases. They are both based on point mapping which is the primary approach used to register images with random textures (11). The similarity of the images is measured by normalized cross-correlation (15). Furthermore, it is assumed that a global affine transformation (18) is sufficient to bring the corresponding coordinates of the reference and input images together. This assumption is simply based on earlier experience with misregistration between the measured property maps. The major causes of misregistration in the 2D measurements are known to be due to different resolution of the measurements and minor error in orientation between the sample and the measuring device. It is also possible that there is a slight obliqueness, for example due to optical imperfections. Affine transformation can model and correct all these effects with six parameters.

The registration is in two phases for accuracy, computational efficiency, and robustness. A coarse approximation for plain translation is first identified and then refined iteratively. The first phase begins by placing a set of nine control points close to the center of the reference map, as illustrated in Figure 2. Small areas around the control points are selected and similar areas are searched from the input image to locate the matching points. At each control point, the estimate of the translation between the images is determined by the position of the maximum of the 2D cross-correlation function. Since

not all the control points require exactly the same translation between the reference and input images, the weighted median value of the nine translation estimates, in both horizontal and vertical directions is chosen as the first phase estimate. Choosing median rather than mean is for robustness.

The second registration phase generalizes the transformation estimate from plain translation to affine transformation. It is an iterative process that gradually refines the transformation estimate. At each iteration step, a set of new control points is automatically positioned on the reference image, and the locations of these points in the input image are predicted with the transformation estimate from the previous iteration step. The exact locations of the matching points are again chosen at the maxima of the 2D cross-correlation function. Since an estimate of the required transformation exists, the search area size in the similarity maximization is considerably smaller than in the first stage. This makes the point search computationally efficient. The locations of the matching points are determined at sub-pixel accuracy by fitting a second order 2D polynomial around the maximum of the cross-correlation function. At the end of each iteration step, the matching control points found so far are used to form a new transformation estimate. A global affine transformation is fitted between the matching control points using a weighted least squares approach so that the effect of abnormal control point pairs is minimized.

The control points selected during the iteration gradually cover the image all the way to the corners of the reference image, thus improving the overall registration accuracy. When the grid of control points finally covers the joint area of the reference and input images, the iterative procedure is terminated and the final affine transformation is fitted between the matching control points. This automatic registration procedure has been tested with many 2D quality maps of both paper and board and affine transformations were found to be appropriate in all cases and the alignment method was accurate and robust. The transformation fitting error is normally less than 0.3 pixels. Obviously, when the two maps to be aligned do not have common forms of variation, the method fails.

The final part of the registration is image alignment in which the estimated transformation is applied to the coordinates of the input image. Pixel values are then interpolated to the new non-integer

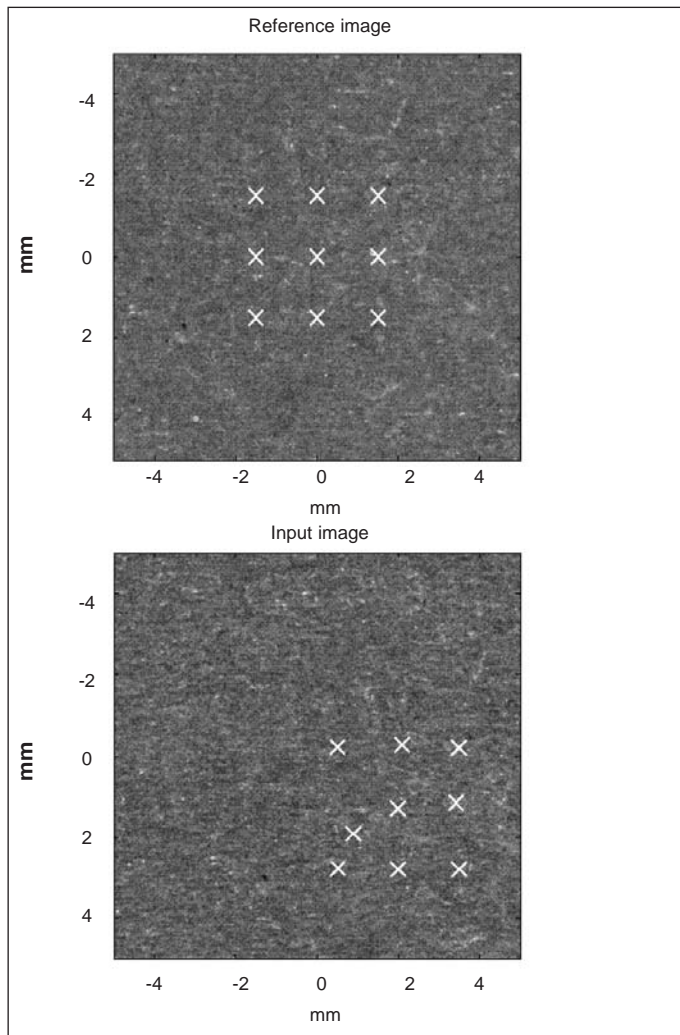


Fig. 2 Estimation of translation at the first phase of image registration. Reference image with search points (top) and input image with found points (bottom). The true translation is $[2.0 \ 1.3]$ mm $(x \ y)$.

coordinates. It is therefore important that the spatial resolution of the input image is high enough to enable the interpolation to the reference image resolution.

MEASUREMENT DATA

Newsprint paper samples that were printed with sheet-fed offset in a pilot press were examined. The printing layout contained various halftone and compact colour areas of which five were selected as test areas to be measured. The size of each test area was 22 by 15 mm. Exactly the same paper properties were measured from the test areas before and after printing. Firstly, optical formation/transmittance was measured with a scanner with illumination from the reverse side of the sheet. Secondly, the samples were scanned with reflective light so that images of paper brightness and print quality were obtained before and after printing, respectively. Thirdly, surface topography was

measured with a photometric stereo device that recovers the topography map from digital photographic images taken with different illumination directions (2). This device also provides photographic images of paper brightness and print quality, to be compared with the corresponding images acquired by scanner. The pixel size in all the measurements is approximately $10 \mu\text{m}$ in x and y directions.

Scanners and cameras were used to record the intensity values of red, green and blue light in separate channels. In case of unprinted white paper the colour channels contain almost equal planar variation. With printed samples the printing colour affects the variation captured by each channel. For instance cyan colour reflects blue and green light but blocks red wave lengths. Therefore the red channel best reveals the variation in print quality on cyan areas, whereas the blue and green channels mostly carry information about the paper, especially in transparent

scanning. Understanding and combining the information on the colour channels is essential in the multivariate analysis of the aligned maps, but also in image registration because the reference and input images should contain maximally common forms of variation to provide accurate registration results.

The image registration procedure described previously has proven to be capable of successfully registering this diverse set of 2D measurements acquired from halftone and compact colour areas. The registration results even revealed the slight geometric distortions in the camera images caused by the optics. It is possible to implement camera calibration to maximize the usable measurement area, but for the current measurements, only the parts of the images with less than a half pixel dislocation were selected for the analysis. Even though this reduced the analyzed area from the original size of 22 by 15 mm, extensive amounts of multivariate image data were obtained; on each test area the number of observations was always more than two million. So far statistical analysis has been restricted to the 2D measurements collected from two different types of compact cyan areas that will be described later in more detail.

In addition to camera calibration, these registration and alignment methods rapidly revealed a subtle twitching of the read head of the scanner that was not discernible by naked eye during the measurement. They also revealed that the target often was slightly out of focus in the scanner measurements. Due to these imperfections, optical formation measurements were not analyzed further. To replace the suboptimal scanner measurement in the future, a camera-based device for the measurement of optical formation has already been constructed, that is expected to give sharper images and better dynamics in particular with the unprinted paper that has been problematic for the scanner.

MULTIVARIATE STATISTICAL ANALYSIS THROUGH JOINT PROBABILITY DISTRIBUTIONS

In what follows, random variables are denoted with upper case letters and the values they take with corresponding lower case letters.

The general form of the joint probability density function of random variables (vectors) \mathbf{X} and \mathbf{Y} is (15)

$$f(\mathbf{x}, \mathbf{y})d\mathbf{x}d\mathbf{y} = P(\mathbf{x} \leq \mathbf{X} \leq \mathbf{x} + d\mathbf{x}, \mathbf{y} \leq \mathbf{Y} \leq \mathbf{y} + d\mathbf{y}) \quad [1]$$

where P denotes probability. Correspondingly, the conditional pdf of random variable \mathbf{y} given \mathbf{x} is (15)

$$f(\mathbf{y}|\mathbf{x})d\mathbf{y} = P(\mathbf{y} \leq \mathbf{Y} \leq \mathbf{y} + d\mathbf{y} | \mathbf{x} \leq \mathbf{X} \leq \mathbf{x} + d\mathbf{x}) \quad [2]$$

The regression of \mathbf{Y} describes the expected value of this conditional density, thus it is a function of \mathbf{x} (15):

$$E\{\mathbf{Y}|\mathbf{x}\} = \mu_y(\mathbf{x}) = \int_{-\infty}^{\infty} \mathbf{y}f(\mathbf{y}|\mathbf{x})d\mathbf{y} \quad [3]$$

If the joint probability density of \mathbf{X} and \mathbf{Y} is a multivariate Gaussian distribution, and if \mathbf{X} and \mathbf{Y} are correlated, the regression of \mathbf{Y} is a linear function of \mathbf{x} . However, the joint probability densities of the property maps measured from paper are not Gaussian. This can be easily verified by the information-theoretic Kullback-Leibler distance, or relative entropy (19). This measures the distance between two probability distributions, $f_1(\mathbf{x})$ and $f_2(\mathbf{x})$:

$$D(f_1(\mathbf{x})||f_2(\mathbf{x})) = \int_{-\infty}^{\infty} f_1(\mathbf{x}) \log \left[\frac{f_1(\mathbf{x})}{f_2(\mathbf{x})} \right] d\mathbf{x} \quad [4]$$

The Kullback-Leibler (KL) distance, D , is always non-negative and zero only if and only if $f_1(\mathbf{x}) = f_2(\mathbf{x})$. If $f_2(\mathbf{x})$ is chosen as the Gaussian distribution estimate based on the data, then $f_2(\mathbf{x})$ is parameterized by one mean vector and one covariance matrix calculated from the data. Then choosing $f_1(\mathbf{x})$ as the histogram estimate or the GMM estimate of the pdf, permits the assessment of the appropriateness of Gaussian approximation to the pdf. The larger the KL distances, the more the distribution ($f_1(\mathbf{x})$) deviates from a Gaussian distribution. The Kullback-Leibler distances computed from the experimental data are reported in the following section.

Another statistical measure found useful in this work is the skewness of the conditional pdfs. The traditional measure of skewness is based on the third moment of the probability density. A skewness parameter based on the more robust order statistics has been used here for comparison. The values of percentiles, $b_{2.5}$, b_{50} and $b_{97.5}$, which are standard tabulated values in statistical literature (e.g. (15)), have been applied. In this case, percentiles were computed numerically from the estimated distributions as inverse values of the cumulative distribution function. The 50 %

percentile, b_{50} , is the median value. The skewness parameter used in this work depends on the relation of the 2.5 %, 50 % and 97.5 % percentiles as follows:

$$skewness = \frac{b_{97.5} - b_{50}}{b_{50} - b_{2.5}} \quad [5]$$

According to this definition, the distribution is symmetric when skewness equals one. As shown in the following section, the probability distributions computed from the property maps measured from paper are typically strongly skewed.

As the joint distributions are not Gaussian, there are more appropriate methods to analyze the dependencies than linear regression. Principal component analysis (PCA) (20) and independent component analysis (ICA) (21) can give an insight into the sources of variation in the data by revealing statistically significant dimensions in the multivariate data space. However, the most complete description of the statistical dependencies between the measured variables is provided by the joint probability density functions.

There are two ways to proceed with the non-Gaussian joint pdfs: by describing the interrelationship of the variables by their joint histogram, or by choosing a parametric model for the joint pdf and identifying the model parameters. In the latter case, the Gaussian mixture model (GMM) (16) is a very attractive choice due to its simple and efficient formulation. GMM approximates the probability density function of a d -dimensional random variable \mathbf{X} as a weighted sum of N Gaussian distributions:

$$f(\mathbf{x}) = \sum_{i=1}^N c_i (2\pi)^{-d/2} (\det(\mathbf{C}_i))^{-1/2} \exp \left[-\frac{1}{2} (\mathbf{x} - \boldsymbol{\mu}_i)^T \mathbf{C}_i^{-1} (\mathbf{x} - \boldsymbol{\mu}_i) \right] \quad [6]$$

Each Gaussian component is parameterized by its mean, $\boldsymbol{\mu}_i$, and covariance matrix, \mathbf{C}_i . The weights, c_i , of the Gaussians components are called the priors. With sufficiently high number of component distributions, GMM is capable of describing practically any continuous distribution (22). The parameters of GMM model are typically estimated by the expectation maximization (EM) algorithm (23).

The joint pdf estimation – either through histogram, GMM or any other method – provides several possibilities for further analysis. Firstly, nonlinear regression can be computed from the joint density by applying Equation 3. Secondly, the different levels of probability in the

joint pdf can be examined to form anomaly maps. They reveal the points and areas of the multivariate image that most extremely deviate from the typical statistical behavior of the data. The condition for an observation vector \mathbf{x} at location i to be abnormal to degree p is given as

$$f(\mathbf{x}) < C(p) \quad [7]$$

where $f(\mathbf{x})$ is the probability density function of \mathbf{x} and the relationship between C and p is determined through

$$p = p(C) = \int_{f(\mathbf{x}) < C} f(\mathbf{x}) d\mathbf{x} \quad [8]$$

In practice, the abnormality degree, p (e.g. 2.5 %), is first chosen. A suitable upper limit, C , is then determined for the probability density so that the integral in Equation 8 equals p . The anomaly map is obtained by making a mask where locations i that satisfy the condition 7 are given a value one whereas all other locations of the mask assume value zero.

Thirdly, the tails of the conditional probability densities can be examined to detect exceptional values on the (print quality) maps. As anomaly maps are based on joint pdfs and tail analysis on conditional pdfs, not all of these latter exceptional values are in the anomaly maps. Finally, the tail areas and the points indicated by the anomaly maps can be overlaid with the original 2D measurement maps. Now it is easy to visualize the points and local areas that show exceptional behavior. The possible concentration of the anomalies on the measured maps indicates disturbances in the process that produced the data.

RESULTS OF MULTIVARIATE STATISTICAL ANALYSIS

The objective of this work is to find and describe the probabilistic dependencies between print quality and the physical structure of unprinted paper. The results presented here concentrate on the joint probability distributions of surface topography and print quality on two different types of test areas. The print quality is described by the photographic image of the test area, taken after printing. The common size of the analyzed 2D maps on each test area (after discarding the geometrically distorted parts) is typically around 20 by 13 mm but a smaller area has been chosen here to show more details. The illustrations present a 5 by 5 mm

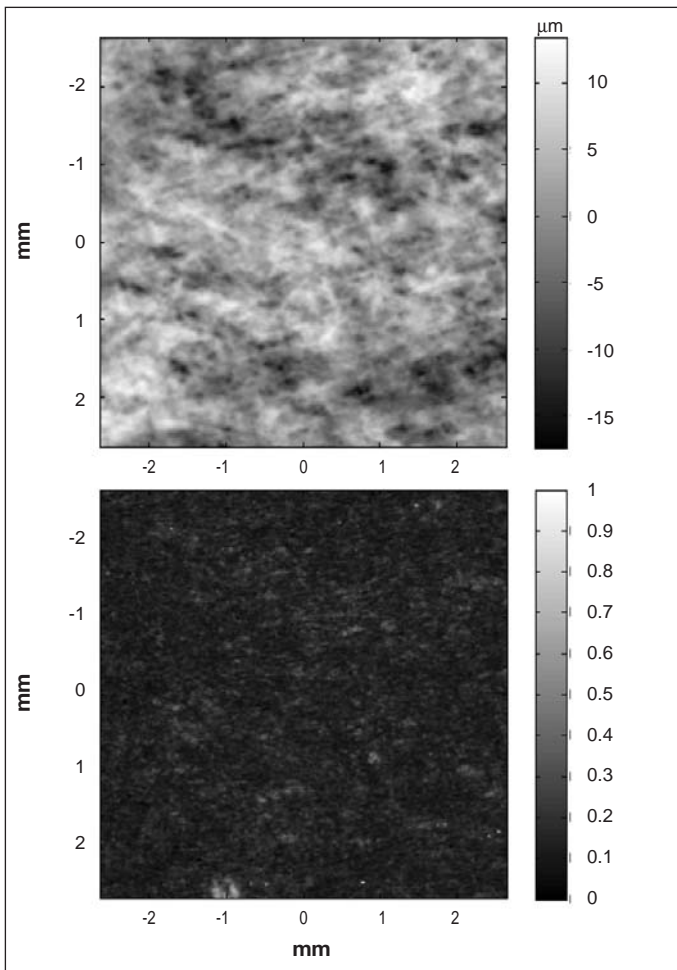


Fig. 3 Surface topography (top) and aligned photographic reflectance image of print quality (bottom) on a 5 by 5 mm area.

selection of a test area that was printed with compact cyan so that only the cyan printing roll pressed the test area. There was neither water application nor back-trap conditions present on this test area. The other type of test area examined in this work was printed with compact cyan in normal 4-colour offset conditions with water and back-trap. Eight newsprint paper sheets were examined, each sheet containing one test area of each type of cyan printing.

In the analysis, both joint histograms and GMM-based pdfs are used to describe the data. By comparing the GMM-based distribution models with histograms it is possible to ensure that all the essential details of the data have been taken into account in GMM. As GMM can describe very complicated distributions with a moderate number of parameters, it is the main tool used in the analysis. Furthermore, GMM enables the analytical calculation of conditional probability densities and statistical parameters such as cumulants and moments.

An example is given of the analysis of

two 2D maps, surface topography and photographic reflectance image of print quality, measured from exactly the same area. The aligned maps are shown in Figure 3. There are light spots in the reflectance (print quality) map due to low local density or missing printing ink. These spots cause the scattering on the upper edge of the joint histogram shown in Figure 4. The three-dimensional histogram is shown from above and the heights of the bins are presented by the different colours. In Figure 4 it is notable that the joint pdf is skewed towards the higher values of reflectance. A closer look at the skewness and the shape of the tails of the conditional distributions is presented in Figure 5. It shows selected vertical 'slices' of the joint pdf estimated by both the histogram (slightly smoothed with a sliding Gaussian kernel) and a 10-component GMM. In Figure 5 the conditional pdfs are presented on logarithmic scale to emphasize the tails of the conditional distributions.

The regression of print quality according to Equation 3, using the maps in Figure 3, is non-linear due to the non-

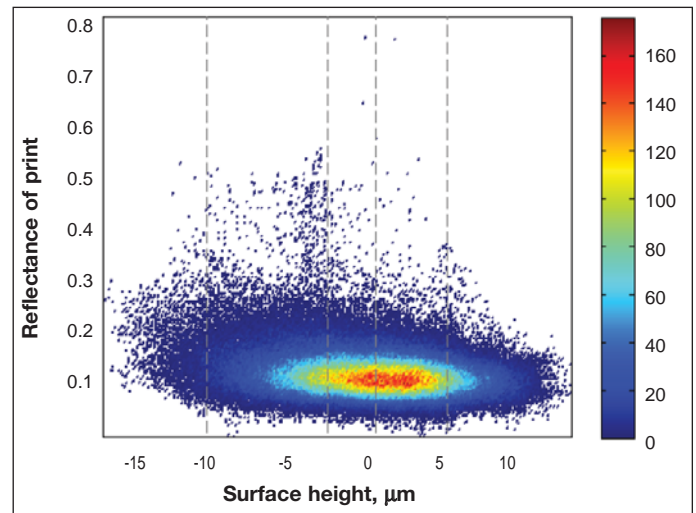


Fig 4 Joint histogram of surface topography and print quality measurements. The vertical dashed lines indicate the sampling points of the conditional pdfs shown in Figure 5.

Gaussian shape of the joint pdf. The regression curves as conditional expected values and their uncertainties are presented in Figure 6 for both the GMM and histogram approach. Notable increase in the reflectance value is expected as the pits in the paper surface get deeper. Instead of a least-squares linear fit over the total data set, the nonlinear regression is computed at each value of surface height from the conditional pdf of reflectance. GMM provides a particularly easy access to the regression estimate that can be calculated analytically from the model parameters. Furthermore, the unstable behavior of regression estimate at the edges of the data value range, resulting from the relatively low number of observations, is avoided in the GMM approach. However, it should be noted that 99 % of the surface height values in this case lie between -11 μm and +10 μm . As there are hardly any data points beyond this range, the regression estimates as well as the Kullback-Leibler distances and skewness values presented in the following are unreliable at the extreme values of surface height.

Figure 7 presents the Kullback-Leibler (KL) distances between the GMM-based conditional pdfs of print quality and the corresponding single Gaussian models. Throughout the surface height range, the KL distance is higher than zero, which was expected from the non-Gaussian shape of the conditional pdfs. It can also be seen that the KL distance decreases as the surface height values increase until the height value reaches 10 μm . Beyond this height the results are unreliable due to the low number of observations. The decrease in KL distance corresponds to

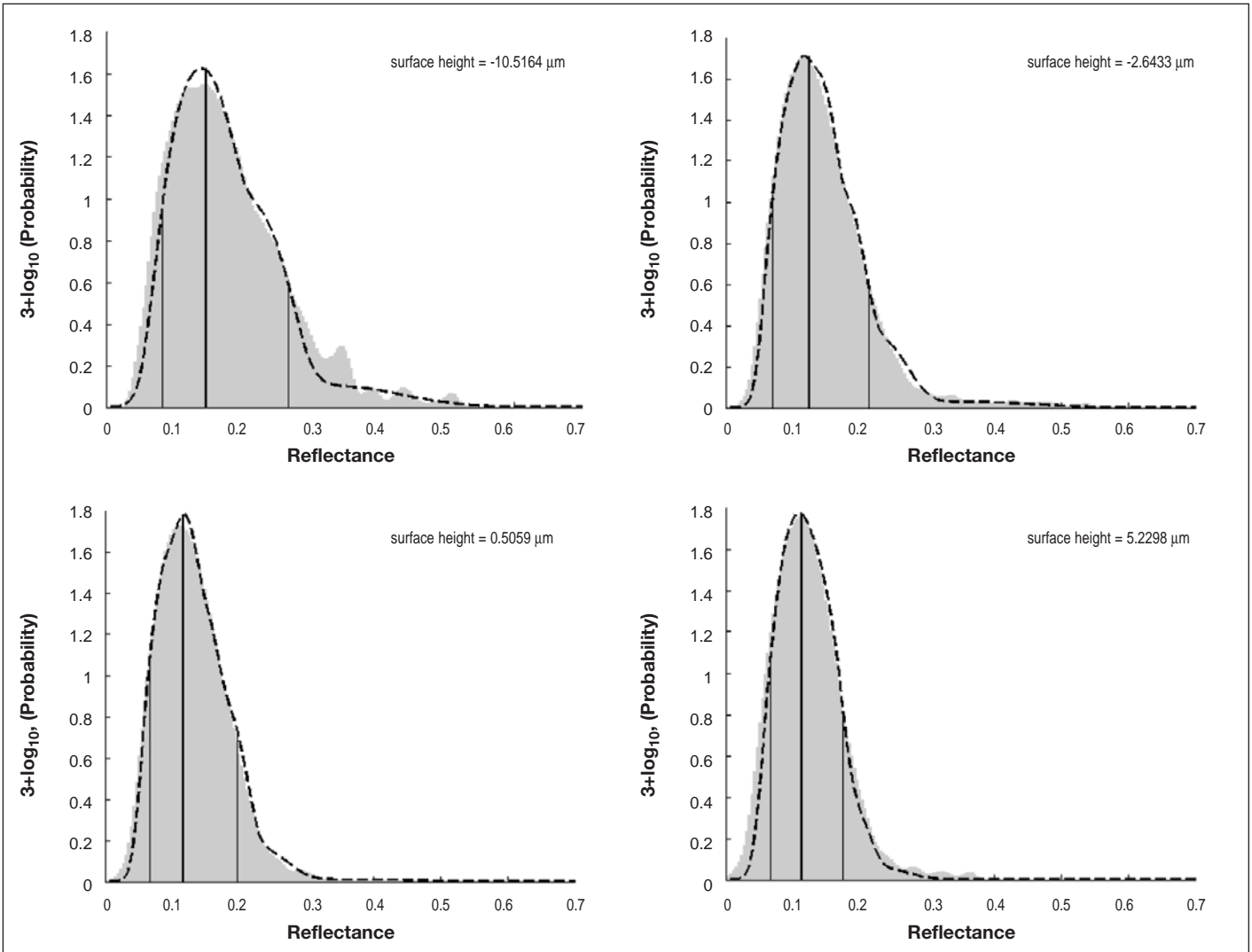


Fig. 5 Histogram-based (gray bars) and GMM-based (dashed black line) conditional pdfs of print quality at the values of surface height shown in Figure 4. The vertical lines indicate 2.5 %, 50 % and 97.5 % percentiles computed from GMM.

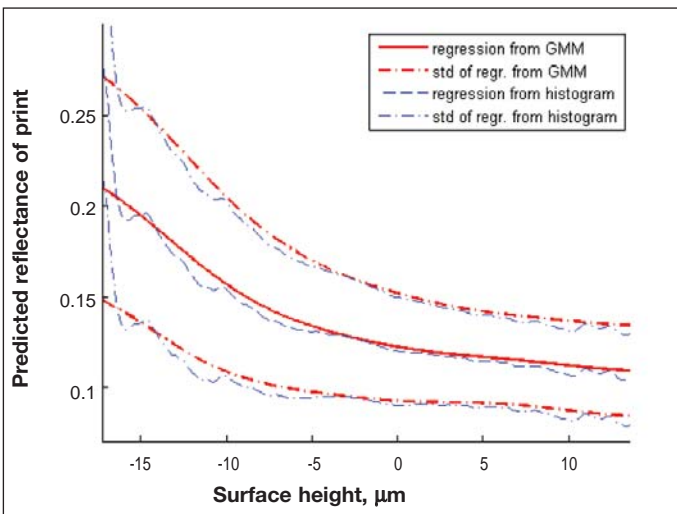


Fig. 6 Regression curves plus/minus their standard deviations computed from GMM (red) and from histogram (blue).

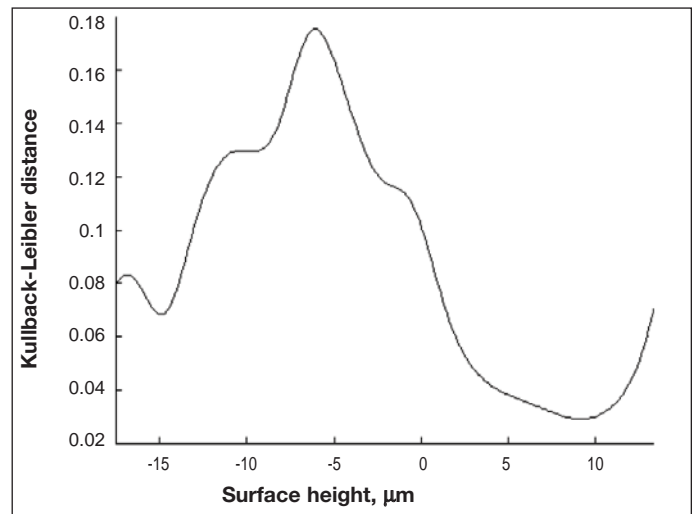


Fig. 7 Kullback-Leibler distance of conditional pdfs of print quality, computed through GMM.

the narrowing of the joint histogram in Figure 4 towards a more Gaussian shape. A similar shape to that of the KL curve can be seen in Figure 8 that presents the skewness of the conditional pdfs of print

quality computed according to Equation 5. The visual analysis of all the 16 cyan test areas (eight with normal printing conditions and eight without back-trap) has suggested that the skewness parameters

and KL distances are related to the amount of print defects. Based on visual inspection, the areas printed without back-trap typically contain clearly visible print defects whereas the normal cyan

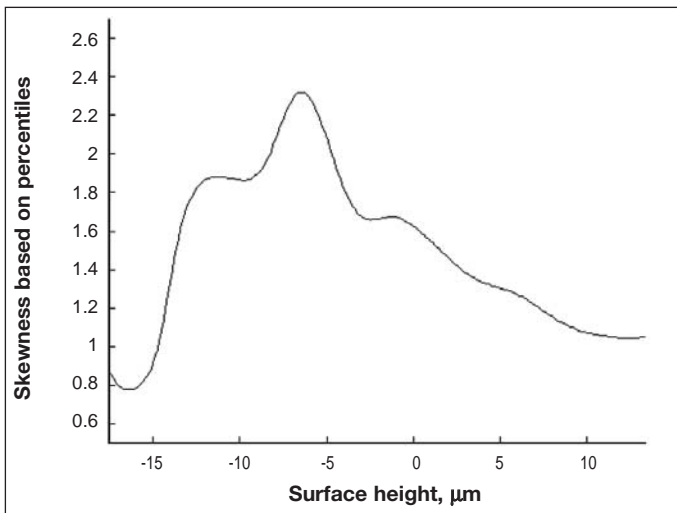


Fig. 8 Skewness of conditional pdfs of print quality, based on the percentiles computed from GMM.

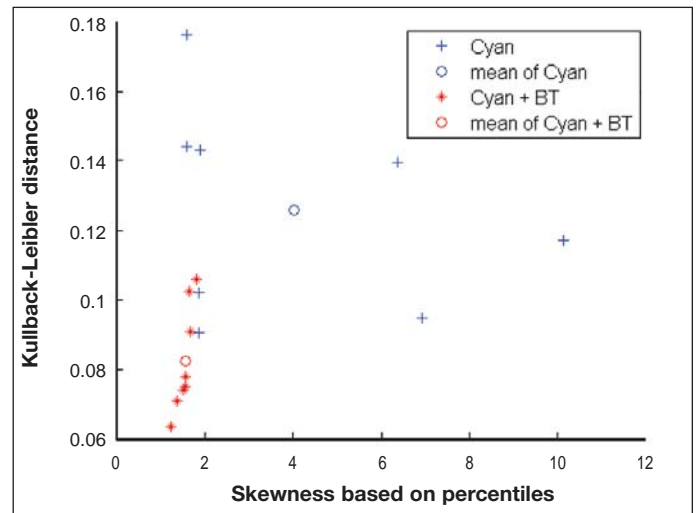


Fig. 9 Skewness parameters and KL distances of the 16 test areas. The blue marks denote the non-back-trap cyan samples and red marks denote the normal cyan areas.

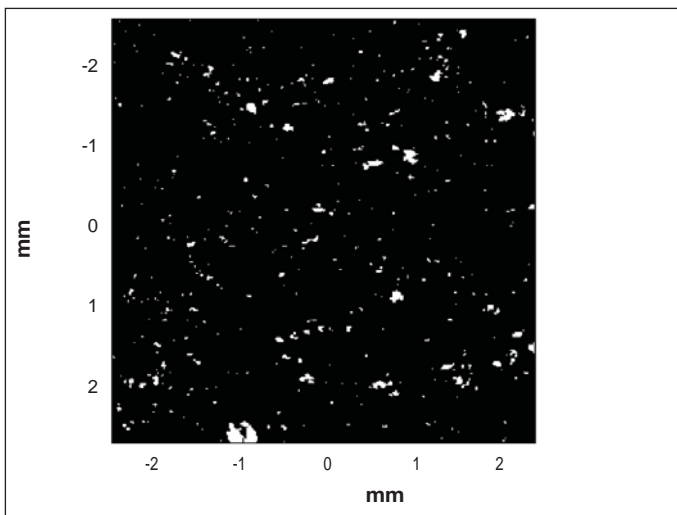


Fig. 10 Joint pdf based anomaly map indicating (by white) the points in Figure 3 that occur with less than 2.5 % probability.

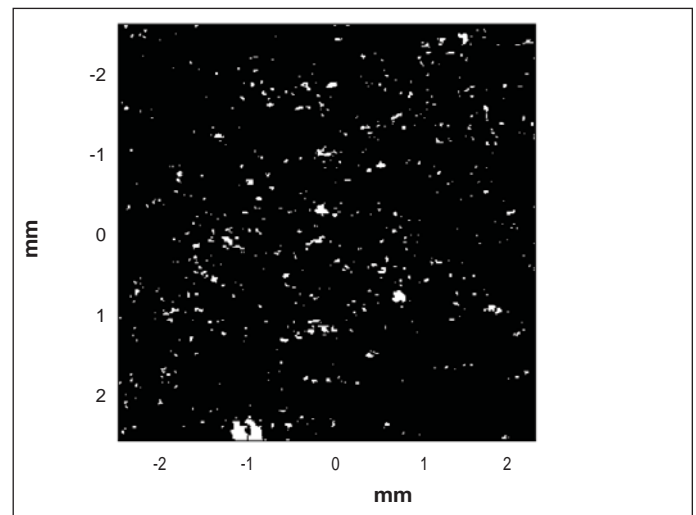


Fig. 11 Mask indicating (by white) the points in the print quality map that are exceptionally bright based on the 2.5 % percentile tails of the conditional pdfs of print quality.

areas have only very small and few light spots, if any. The print defects skew the joint histogram towards the high values of reflectance and thus increase the skewness measure and Kullback-Leibler distance. To summarize the behavior of these parameters in the different printing settings, the shape of the conditional pdf of print quality, subject to the condition that the surface height value is below zero, was examined. This limits the inspection to the areas where valleys or pits in the surface may have caused print defects. The skewness parameter and KL distance have been computed from the conditional pdf of print quality of each of the 16 test areas. The results are illustrated in Figure 9. When the eight non-back-trap cyan areas are compared to the eight normal cyan areas, the average KL distance increases

approximately 50 % and the average skewness more than doubles.

Anomaly maps can be derived from the joint pdf by thresholding according to a chosen level of probability. Figure 10 presents an anomaly map that reveals those points from the surface topography and print quality maps of Figure 3 that occur with less than 2.5 % probability according to their joint probability distribution. As the likelihood of these observations is very small, they cannot be expected to be explained by the regression model. For comparison, Figure 11 shows a mask that detects exceptional points in the print quality map based on the low probability tail areas of the conditional pdfs. While the mask in Figure 11 efficiently detects the points where the reflectance measured from the print is

exceptionally high, the mask in Figure 10 introduces the effect of the combined exceptionality of surface height value and print quality. The comparison of these masks provides information about the role of surface topography in the occurrence of print defects.

DISCUSSION

This study has been limited to printing newsprint paper with sheet-fed offset even though this is not commercially relevant. Newsprint was chosen for the experiments because a relatively clear view of the effect of surface topography on print quality was wanted, without the additional complexity caused by coating. Sheet-fed offset was chosen because it was the only production-scale printing

method that enabled controlled measurements before and after printing.

The unusual printing conditions may partly explain the large variance of the skewness and Kullback-Leibler results seen in Figure 9. This is particularly likely for the non-back-trap test areas where neither water application nor back-trap conditions were present. Various factors other than surface topography, for instance surface strength, have obviously affected the print quality in this experiment. It will be possible to further verify the feasibility of the probabilistic analysis framework as new printing data sets become available from, e.g., gravure printing experiments.

CONCLUSIONS

A two-phase image registration procedure for robust and accurate automatic registration and alignment of randomly textured images has been developed and implemented. Successful sub-pixel alignment of the 2D measurements has enabled the probabilistic joint analysis of print quality and surface topography maps measured from exactly the same area. The large amount of multivariate pointwise data in the aligned property maps provides a strong basis for statistical inference.

The objective of the work is to find and describe the dependencies between print quality and the physical structure of unprinted paper. These dependencies are probabilistic rather than deterministic, and therefore the joint probability distributions of the measured variables are needed to reveal the essential information. The joint pdfs have been described by histograms and Gaussian mixture models. The skewness and Kullback-Leibler distance parameters have been computed from the

pdfs, and the usefulness of these parameters in the characterization of the probability densities and, finally, print quality has been illustrated. Anomaly maps have also been formed from the joint pdfs to reveal the low probability, high importance, print defects and to evaluate their origins.

As indicated in this work, multivariate analysis in terms of joint pdfs is an important link between the combined effect of unprinted paper properties, processing conditions and the quality of print – directly measurable as a map of colour variation. It is expected that these methods will find wide application in analyzing the structural dependencies of paper and board quality.

REFERENCES

- (1) Norman, B. and Wahren, D. – Mass distribution and sheet properties of paper, *Trans. 5th Fund. Res. Symp.*, (ed. F. Bolam), Cambridge, p. 7 (1973).
- (2) Hansson, P. and Johansson, P.-Å. – Topography and reflectance analysis of paper surfaces using a photometric stereo method, *Optical Engineering* **39**(9):2555 (2000).
- (3) Chinga, G., Johnsen, P.O., Dougherty, R., Lunden-Berli, E. and Walters, J. – Quantification of the 3D microstructure of SC surfaces, *J. Microscopy* **227**(3):254 (2007).
- (4) Sung, Y. J., Ham, C. H., Kwon, O., Lee, H. L. and Keller, D. S. – “Application of thickness and apparent density mapping by laser profilometry,” *Trans. 13th Fund. Res. Symp.*, (ed. S.J. I’Anson), Cambridge, p. 961 (2005).
- (5) Fetsko, J. M. and Zettlemoyer, A. C. – Factors affecting print gloss and uniformity, *Tappi* **45**(8):667 (1962).
- (6) Lyne, B. – Machine-calendering: implications for surface structure and printing properties, *Tappi* **59**(8):101 (1976).
- (7) Oittinen, P. and Saarelma, H. – **Printing**, Fapet, Finland, p. 214 (1998).
- (8) Kajanto, I. M. – Pointwise dependence between local grammage and local print density, *Paper and Timber* **73**(4):338 (1991).
- (9) Mangin, P. J., Béland, M.-C. and Cormier, L. M. – A structural approach to paper surface compressibility – Relationship with printing characteristics, *Trans. 10th Fund. Res. Symp.*, (ed. C.F. Baker), Oxford, p. 1397 (1993).
- (10) MacGregor, M. A., Johansson, P.-Å. and Béland, M.-C. – Measurement of small-scale gloss variation in printed paper, *Proc. 1994 Int. Printing and Graphics Arts Conf.*, Halifax, p. 33 (1994).
- (11) Brown, L. – A Survey of image registration techniques, *ACM Computing Surveys* **24**(4):325 (1992).
- (12) Althof, R.J., Wind, M.G.J. and Dobbins, J.T. – A rapid and automatic image registration algorithm with subpixel accuracy, *IEEE Trans. Medical Imaging* **16**(3):308 (1997).
- (13) Liu, J., Vemuri, B. C. and Marroquin, J. L. – Local frequency representations for robust multimodal image registration, *IEEE Trans. Medical Imaging* **21**(5):462 (2002).
- (14) Lähdekorpi, M., Ihalainen, H. and Ritala, R. – Using image registration and alignment to compare alternative 2D measurements, *Proc. XVIII IMEKO World Congress*, Rio de Janeiro (2006).
- (15) Papoulis, A. – **Probability & Statistics**, Prentice-Hall, USA, p. 98-239 (1990).
- (16) Nabney, I. T. – **Netlab: Algorithms for pattern recognition**, Springer-Verlag, UK, p. 79-113 (2002).
- (17) Heiskanen, I. – **Two-dimensional small-scale mapping methods in predicting flexographic printability of board**, Licentiate thesis: Lappeenranta University of Technology, Finland (2005).
- (18) Wolberg, G. – **Digital image warping**, IEEE Computer Society Press, USA, p. 47 (1990).
- (19) Cover, T. and Thomas, J. – **Elements of information theory**, John Wiley & Sons, USA, p. 18 (1991).
- (20) Geladi, P. and Grahn, H. – **Multivariate image analysis**, John Wiley & Sons, UK, p. 87 (1996).
- (21) Hyvärinen, A., Karhunen, J. and Oja, E. – **Independent component analysis**, John Wiley & Sons, USA (2001).
- (22) Bishop, C. M. – **Pattern recognition and machine learning**, Springer-Verlag, USA, p. 110 (2006).
- (23) Figueiredo, M. A. T. and Jain, A. K. – Unsupervised learning of finite mixture models, *IEEE Trans. Pattern Analysis and Machine Intelligence* **24**(3):381 (2002).

Original manuscript received 2 August 2007, revision accepted 3 November 2007.

Publication III

Mettänen, M., Lauri, M., Ihalainen, H., Kumpulainen, P. and Ritala, R. (2009): Aligned analysis of surface topography and printed dot pattern maps. *Proc. Papermaking Research Symposium*, Kuopio, Finland, June 2009.

© 2009 PRS. Reprinted, with permission, from Proceedings of the Papermaking Research Symposium.

ALIGNED ANALYSIS OF SURFACE TOPOGRAPHY AND PRINTED DOT PATTERN MAPS

M. Mettänen¹, M. Lauri², H. Ihalainen³, P. Kumpulainen⁴, R. Ritala⁵

¹ Corresponding author. E-mail: marja.mettanen@tut.fi,

² mikko.lauri@tut.fi, ³ heimo.ihalainen@tut.fi, ⁴ pekka.kumpulainen@tut.fi, ⁵ risto.ritala@tut.fi.

Tampere University of Technology, Department of Automation Science and Engineering, P.O. Box 692, FI-33101 Tampere, Finland.

Abstract. We examine the relationship between printed dot patterns and the surface topography of unprinted paper. We acquire small-scale 2D measurements of reflectance and surface topography by a camera based method and align the measurement maps obtained before and after printing. We introduce a robust two-step procedure for locating the regularly spaced raster dots from the print reflectance measurement. The first step detects the regular dot pattern with 2D Fourier analysis. The second step locates the exact dot positions by a method based on cross-correlation in the spatial domain, thus taking into account the possible deviations from the regular pattern. With the high-resolution measurements, the accurate image alignment and the detection of the dot pattern, the dependence between unprinted paper surface topography and the halftone print properties can be analyzed statistically. In this work we analyze SC paper strips of three roughness levels printed by an IGT gravure test printer under various nip pressures. Our results imply that the deep depressions in the surface topography can explain up to 15 percent of the missing or partly missing dots.

Keywords: Halftone printing, Print quality, Surface topography, 2D Fourier analysis

1 Introduction

Paper surface structure and its inhomogeneities are associated with the attainable print quality. Research on this relationship in halftone printing is particularly important because most printed matter is produced by printing dot patterns. Long before the introduction of the efficient digital image processing facilities of today, the surface profile of paper has been shown to contribute to halftone printability in letterpress [7]. Further studies on halftone prints, e.g., by Heintze et al. [6] and Bristow et al. [2], have shown the importance of the surface roughness, measured as PPS, and compressibility measurement in predicting the quality of gravure print. Later, the roughness measurements that characterize the measurement area by a single value, such as PPS, have been accompanied by 2D surface topography maps. For instance, Lipshitz et al. [12] have evaluated the distributions of various characteristics computed from high-resolution topography maps, and examined their relation to gloss. Topography maps have been acquired from paper samples before and after the application of pressure and then aligned, so that the compressibility of paper and the dependence of the number of missing gravure dots on the nip pressure in gravure printing could be studied [14]. Employing pointwise aligned 2D measurements of surface topography and fulltone print reflectance, topography has been confirmed to correlate with the small-scale gloss variation [13] and with the occurrence of missing printing ink [1, 15]. While these results clearly indicate the

statistical dependence between surface topography and print quality, the presented methods are not directly applicable to images of halftone printing that consist of ink dots instead of (intended) full coverage with the ink. The missing link is the separation of the dot areas from the void areas that lie between the dots.

In this paper we present a set of robust image analysis methods for detecting raster dot patterns from print automatically, and for studying the dependence of print defects on the surface topography of unprinted paper. To exemplify the methodology, we examine supercalendered (SC) paper samples printed by an IGT gravure test printer [8]. The area under examination is the conventional screening area of the Heliotest strip that consists of a dense regular raster dot pattern due to the engraved cells on the printing cylinder. In the printed paper some dots are partly or totally missing because of the imperfect contact between the paper and the printing cylinder. Our objective is to detect the regularity from the print reflectance image and to locate with subpixel accuracy all the coordinates where raster dots are supposed to be situated. As will be shown in Section 3, the methods developed are suitable for a wide range of prints, varying from actual halftone printing (e.g. 50 % raster) to the gravure screening that is visually very close to fulltone printing. We refer to the printed elements as raster dots in all the cases.

The problem of finding the exact dot locations falls to the area of regular pattern detection in which Fourier analysis methods are widely applied. The Fourier magnitude spectra have been recently used in [17] and [3] to extract the regular part from images of halftone printing. Vartiainen [17] has applied the method to estimate the irregular part of the image in order to detect missing dots, while Eerola et al. [3] have thresholded the synthesized regular image to locate the centroid of each dot. Our method for locating the dot coordinates also determines the average scale and the direction of the regularity from the Fourier magnitude spectrum, but each coordinate of the resulting raster point grid is refined by template matching in the spatial domain. This method is very accurate and robust against slight geometrical distortions in the image. We obtain an estimate of the expected reflectance at each pixel of the print reflectance image that would be realized if the print was perfect. We detect the pixels where printing ink is missing although they belong to the raster point area. Furthermore, we evaluate the coincidence of these defect points with the depressions in the surface topography. We also extract the raster dots from the print reflectance image and visualize their quality distribution using self-organizing maps (SOM) [11] and clustering [18].

This paper is organized as follows. We will first briefly introduce the printing experiment and the data acquisition procedure in Section 2. The search of the raster dot locations will be described in Section 3. In Section 4, we will introduce the analysis methods applied to the raster data and to the surface topography, and Section 5 will present the results. Conclusions will be drawn in Section 6.

2 Measurement data

In this work we study SC paper samples of three roughness values; in terms of PPS10 the roughness levels are 1.24 μm , 1.15 μm and 1.11 μm . For the printing experiment, the paper sheets of each roughness were cut into eight strips of width 25 mm and length 300 mm for IGT gravure test printing [8]. Three printing nip pressure levels were applied. They are presented by the printing force in Table 1 that summarizes the number of paper strips in each roughness-pressure combination. The samples were handled and printed

under standard laboratory conditions in which the temperature is 23 °C and the relative air humidity is 50 %.

Table 1: Number of paper samples in each roughness-pressure (force) combination.

Printing force	PPS10		
	1.24 μm	1.15 μm	1.11 μm
250 N	3	3	3
350 N	3	3	3
600 N	2	2	2

Before printing, we selected three test areas from the printing layout of a Heliotest strip. The first two areas, partly overlapping with each other, were in the conventional screening area that resembles visually fulltone printing, and the third area was in the beginning of the variable halftone screen area that is usually examined for the 20th missing dot [8]. The selected areas were imaged with a photometric stereo device that applies the principles described in [5]. The method is based on photographic imaging with slanting illumination and it provides reflectance and surface topography maps from exactly the same area of the paper sample. Our implementation of the measurement equipment additionally provides optical transmittance images by taking pictures of the samples with a bright illumination at the reverse side. All the images are in RGB colors and contain 2268 x 1512 pixels. The image size is 22.5 x 15 mm, and thus the pixel size is approximately 10 x 10 μm .

The imaged paper strips were printed and then the test areas were imaged again by the same procedure as before printing. The 2D measurements obtained before and after printing were aligned at subpixel accuracy by an image registration method based on cross-correlation [16]. It applies a global affine transformation [20] which, however, cannot correct the potential geometrical distortions of the image caused by the imaging optics. The distortions can be examined from the transformation fitting error map. In this experiment we observed that lens distortions larger than 0.2 pixels occur only at the edges and corners of the images and the distortions are always smaller than 0.5 pixels in the aligned images. The image registration and alignment was therefore considered accurate enough for our purpose. However, the possibility of increasing optical distortions towards the corners of the images was taken into account in the development of the dot pattern detection algorithm.

3 Dot pattern detection

The green channel of the print reflectance measurement is the most sensitive of the RGB channels to the red printing ink used in the IGT printing test. Therefore we have chosen to search for the raster dot locations from the green channel. To adapt to the possibility of the regular pattern having slightly different scale and/or direction in the opposite corners of the image, we split the print reflectance image into blocks that are processed separately. Very robust results have been obtained by using eight blocks of equal size. From each block, the dots are searched by a two-step procedure utilizing first the Fourier domain regularity information and then spatial correlations. The following two subsections will describe the steps.

3.1 Regular pattern search in 2D Fourier domain

In the first step of the raster dot localization, 2D Fourier transform is applied to the reflectance map. We apply the Welch spectrum estimate [19] with a Gaussian smoothing window to attenuate the side lobes of the peaks in the spectrum. Figure 1 (a) presents a typical spectrum estimate from a printed sample that is of relatively high quality in our IGT test printing series. A section of the corresponding print reflectance map is shown in Figure 1 (b). The spectrum peaks that can be reliably resolved from their background are located (excluding the centre peak), and their distances from each other are computed. The distances are collected into an $M \times 2$ matrix, D , in which each row is of the form $[\Delta k_x, \Delta k_y]$, where k_x and k_y denote the wave number (in units of $1/\text{mm}$) in the horizontal and vertical directions, respectively. The most frequently occurring entries in D indicate the dominating spacing of the spectrum peaks. This information is compressed by the histogram of the peak distances.

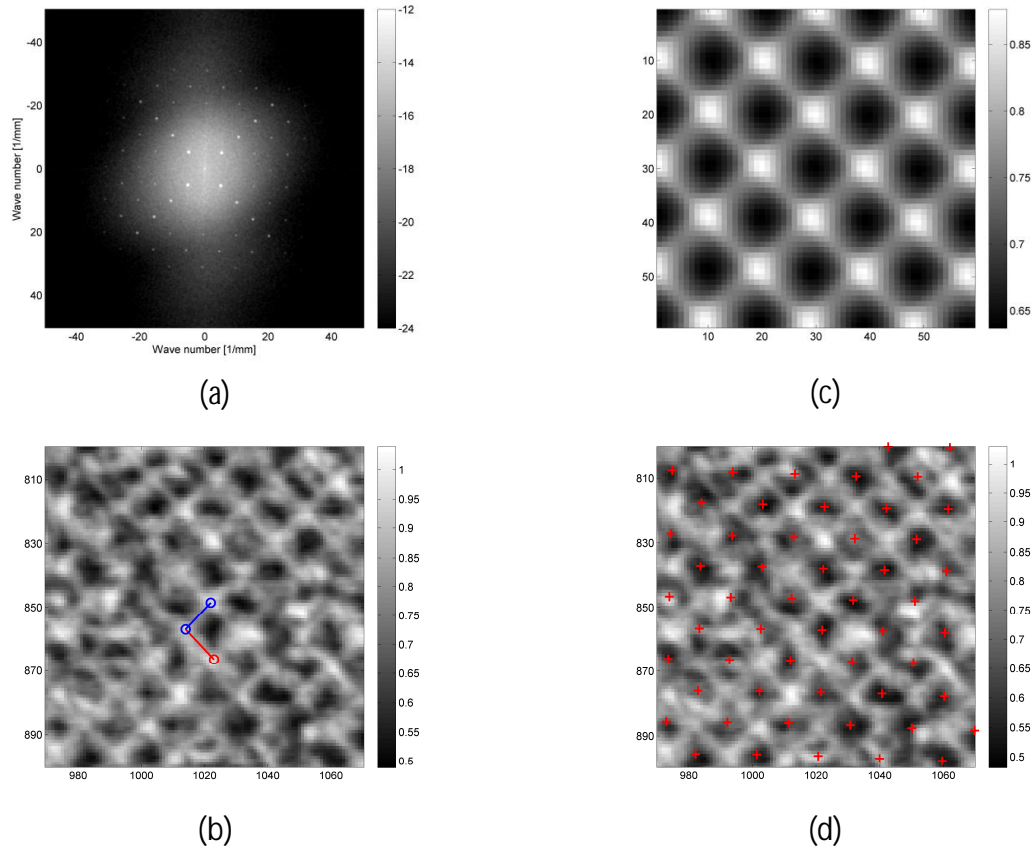


Figure 1: Raster dot search. (a) Spectrum estimate of print reflectance on logarithmic scale. (b) Found basis vectors drawn on top of a section of the print reflectance. (c) Convolution target applied in the refined search step. (d) Final grid points marked by red.

Two basis vectors are needed to determine the 2D regular structure. The first vector is determined by the entries of D that caused the highest peak in the histogram of D . The second vector is then chosen so that it does not point in the same direction as the first vector, but is still based on one of the highest peaks in D . The regular structure of the screening dot pattern is equally visible in all directions in our images, and thus the two basis vectors are found easily. They are of the form $[\Delta k_x, \Delta k_y]$. Finally the basis vectors are converted from the wave number space of the Fourier domain into spatial units (pixels). Figure 1 (b) illustrates the spatial basis vectors on top of the print reflectance map. They are duplicated in each image block to form a grid that covers the area from which the vectors were estimated. The result from the first phase of the raster dot search is thus a regular block-specific grid that indicates the average spacing of the ink dots. This grid is typically not centered to the raster dots, but that will be corrected in the second phase of the search procedure.

3.2 Refined search in spatial domain

The objective is to make the grid indicate the coordinates where the centres of the raster dots would be if they all had printed perfectly on the paper. Therefore, a large number - typically several hundred - of square shaped areas in each block are picked from around the grid coordinates provided by the first step. We define each square to cover three to four raster dots in both directions. The average of the squares, denoted as the *template*, represents an estimate of the average print quality in the image block. It also serves as a tool to shift the block-specific grid very close to the centres of the raster dots. In each block, we locate the centres of the raster dots in the *template* and determine the shift from the centre pixel of the template to the nearest raster dot centre. Then we apply this shift to the grid coordinates of the image block, and repeat this procedure in each block. Consequently, picking the square shaped areas from around the new grid coordinates provides a template that is centered on a raster dot. Figure 1 (c) illustrates a centered template, computed as the average of the small squares over the total image area.

The template, such as that shown in Figure 1 (c), is a prototype of the print reflectance in the paper sample. Thus we use it as a convolution target to search for similar patterns from the print reflectance map. As pointed out by Khalaj et al. [10], this self-reference method is convenient in that all the necessary information can be extracted from the image that is being analyzed, and no database is needed. The locations of maximum local correlation between the print reflectance image and the convolution target determine the final subpixel grid. By this procedure, the possible deviations from the regular pattern, caused by lens distortions, paper stretching or other reasons, are taken into consideration. The result is an accurate subpixel estimate of the location of each raster dot. Figure 1 (d) gives an example of the final grid points.

Although we have implemented the point search method using gravure printed samples as a test case, we expect it to be very useful also with other printing methods. Figure 2 presents examples of gravure and offset-printed halftone areas from which the dot locations have been successfully found by our method.

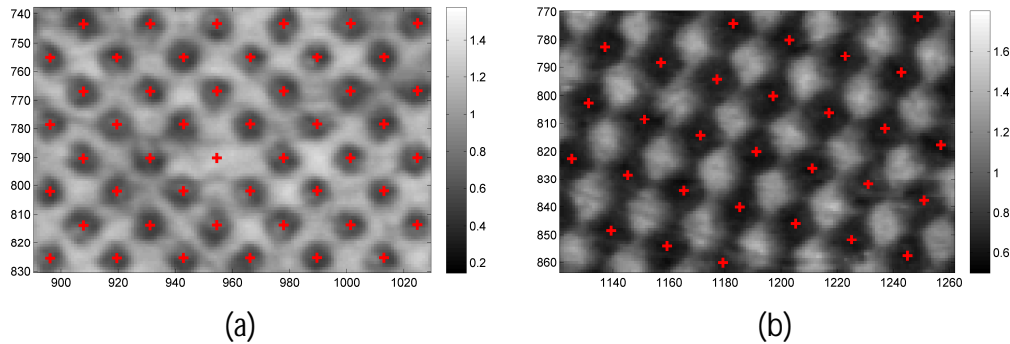


Figure 2: Examples of found raster dot locations. (a) Halftone area of a Heliotest layout. (b) 50 % halftone test area of an offset-printed newspaper.

4 Analysis of printed dots

The detection of the raster pattern allows us to extract the areas of individual raster dots from the aligned print reflectance and surface topography maps. Each gravure printed sample examined in this work contains approximately 15000 dots on the 22.5 x 15 mm analysis area. This section introduces two analysis methods applied to the data. The first approach is to restrict the analysis to those points that were supposed to be covered by ink in the printing, in order to determine how large a proportion of the missing printing ink can be predicted based on the surface topography measurement. The second approach analyzes the properties of the raster dots based on their reflectance values and aims to form clusters of high and low quality dots in order to characterize the print quality.

Due to the supercalendering, some fibres on the paper surface appear dark in our topography maps, as if they were depressions. To prevent these erroneous surface height observations from affecting the analysis results, they must be removed from the analysis area. We obtain a high contrast image of the darkened fibres through the principal component analysis (PCA) [4] of the 6-dimensional image that consists of the RGB channels of the unprinted reflectance and transmittance measurements in which the fibres are also visible. By thresholding this principal component image so that 10 % of the lowest intensities are selected, we obtain a binary mask that indicates the erroneous pixels. A morphological opening operation of the mask further improves the result by reducing noise and connecting broken lines and patterns. We have made the mask to cover a rather large proportion of the image area to make sure that the number of erroneous pixels is minimized in the analysis. When the mask is applied to the grid of raster dots, slightly less than one third of the dots are discarded. Thus the number of raster dots in the analysis is still larger than 10000. This reduced data set is used throughout the analyses presented in the rest of this paper.

4.1 Coincidence of defects in topography and print

The first step in estimating the contribution of surface topography to the missing ink is to separate the pixels that belong to the ink dot area from those that lie on the void area between the dots. For this purpose the average radius of the dots is estimated from the print prototype (see Figure 1 (c)). In our work the radius is 4.5 pixels. Then, at each grid point found outside the darkened fibre area, those pixels that lie within the allowed radius

are selected from the aligned maps of unprinted surface topography and print reflectance. The pixels that lie in the regular void area of the print are not analyzed.

The overall dependence between topography and print reflectance is weak even in the restricted data set. Thus we concentrate on the tails of the probability distributions and perform a simple classification into abnormal and normal observations. The surface topography values are classified as abnormal if they are below a certain threshold, i.e., they represent abnormally deep pits or depressions. The print reflectance values are classified as abnormal if they are exceptionally high, i.e., ink is missing. The abnormal pixels of each measurement are indicated by the corresponding binary masks that have logical 1's in the abnormal points and logical 0's elsewhere. The overlap of the 1's of the topography mask and reflectance mask is then measured.

Since no ground truth is available on the amount of defects in the print or abnormalities in surface topography, we apply several mask percentages, p . For instance, the value $p = 3\%$ means that three percent of the pixels that were found valid for the analysis purposes are marked abnormal. They correspond to the tail of the distribution of the measurement values. The same mask percentage is always applied to both the topography and print reflectance measurements. The value of p varies in this work from 0.5% to 15%. The probability of accidental coincidence of the topography and reflectance masks obviously increases linearly with p . Therefore we subtract the value of p from the computed overlap percentage.

4.2 Analysis of print quality with SOM and clustering

Self-organizing map (SOM) [11] and clustering [18] are used to detect representative samples of the main characteristics of the raster dots. In this case, the individual raster dots are extracted from the print reflectance map as square shaped areas from around the valid grid coordinates and interpolated to have their exact centre points in the middle pixel of the square. The size of each square is 13 x 13 pixels. In high quality raster dots, printing ink is expected to appear in the middle as a dark, round area of diameter 9 pixels.

The SOM with 200 nodes is first trained using six features computed from the print reflectance data: the overall mean and standard deviation in the raster dot, and the mean values and standard deviations in the inner and outer circular partitions of the dot. In this study we use a 1-dimensional SOM which is initialized along the first principal component of the 6-dimensional feature space [9]. Using SOM as an intermediate step reduces the computational load. It also helps in visualizing the results. SOM arranges the nodes along a line by their proximity. Due to the initialization by PCA, the poor and high print quality dots tend to be organized in the opposite ends of the line providing a plausible interpretation of the results. These data do not have distinct clusters but spread out smoothly in the data space. However, hierarchical clustering with complete linkage [9] applied to the code vectors of the 1-dimensional SOM has shown to reveal useful clusters. We have chosen to form ten clusters. The mean values and standard deviations of the raster dots within each cluster are calculated to represent the main characteristics of the clusters. Finally, the similar data selection procedure as described above is performed on the aligned surface topography map, and the mean values and standard deviations of the topography selections are calculated in the clusters that were determined based on the print reflectance. Examples of the results will be given in the following section.

5 Results

The analysis of the aligned topography and reflectance measurements reveals the degree to which the surface topography has been the reason for missing ink. An earlier study with fulltone test areas has found 7 % to 18 % overlap between missing ink and the surface depressions in offset printing [15]. Figure 3 presents our results from the gravure printing experiment. They are comparable with those of the offset trial, except for the smoothest paper quality. The abnormally deep points in the surface topography of the unprinted SC paper seem to have some ability to predict the missing ink. Figure 3 also shows that the predictive power increases with increasing printing nip pressure. This implies that the surface depressions - at least in SC paper - are not as sensitive to increasing nip pressure as the other factors that explain missing ink. By visual assessment, the increasing nip pressure clearly improves the print quality.

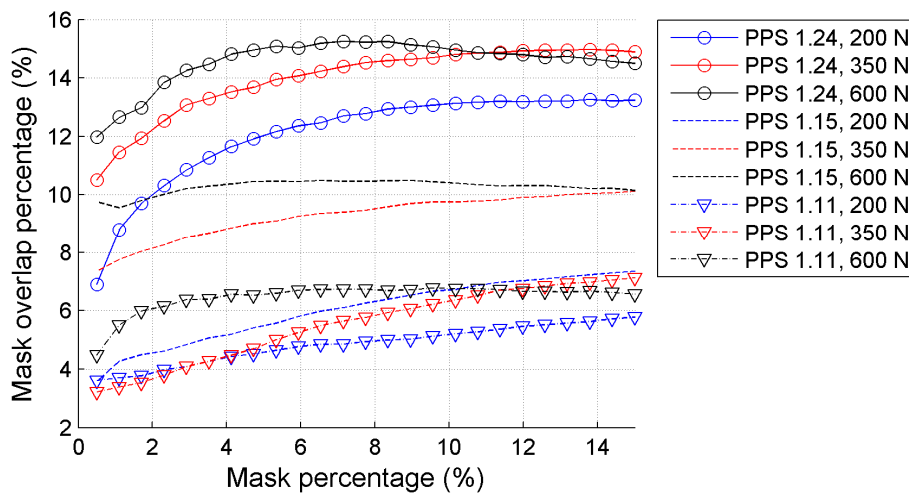


Figure 3: Overlap of the masks of missing ink and topography depressions. Each curve presents the average of two or three test areas as depicted in Table 1. The mask percentage, p , has been subtracted from each curve.

SOM and clustering have been applied to the raster dots to form clusters that characterize the quality of the print. The clusters are based on the print reflectance measurement but the surface topography of the unprinted paper is also examined inside the clusters formed. Figures 4 and 5 illustrate typical results from the opposite ends of the range of tested conditions (in terms of paper roughness and printing pressure). In the high print quality sample presented in Figure 4, approximately 80 % of the raster dots can be considered to have printed successfully. They are contained in five clusters that are also characterized by smooth surface topography free of deep depressions. A few small clusters on the right present raster dots with ink missing in the centre, and the mean values of surface topography in these clusters imply pits of the same size scale. These clusters cover 4-7 % of the raster dots, which is also in line with the overlap percentage of abnormalities presented in Figure 3.

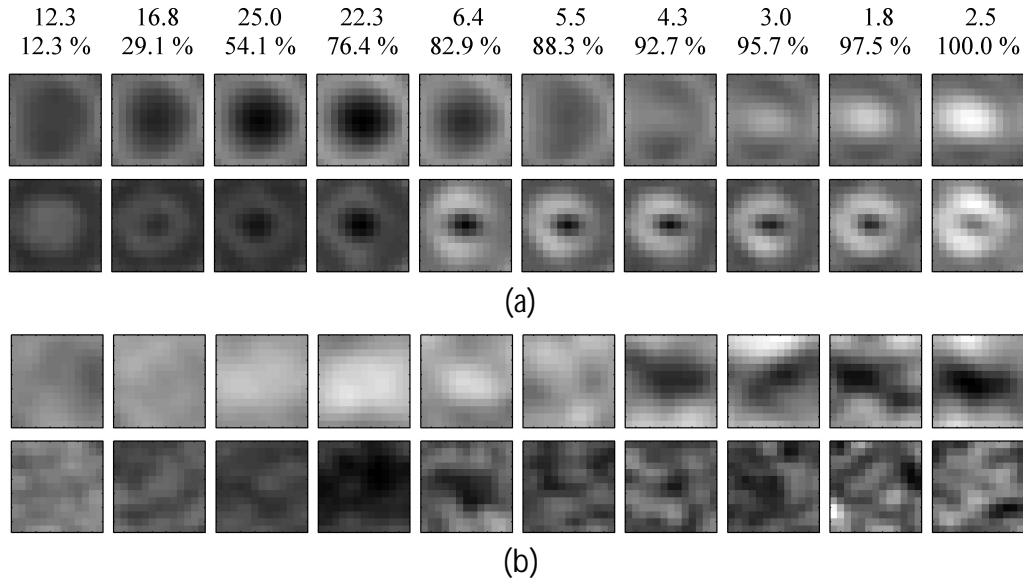


Figure 4: Raster dot clusters from a smooth paper (PPS 1.11 μm) printed at the highest pressure (force 600 N). The percentages of raster dots falling into each cluster, as well as the cumulative percentages, are given at the top. (a) Print reflectance, showing the mean of the raster dots in each cluster in the top row and the standard deviations in the bottom row. (b) Corresponding mean and standard deviation from unprinted surface topography.

Figure 5 presents the clustering results for one of the lowest quality paper samples of the test. In this sample, only 30-40 % of the raster dots are of high quality. The low standard deviation in the middle of the raster dots in several clusters also confirms that missing ink is very common in this sample. Similarly to Figure 4, the deep depressions of surface topography mainly appear in the clusters on the right, where the clusters seem to have formed due to clearly missing ink or variable quality of raster dots.

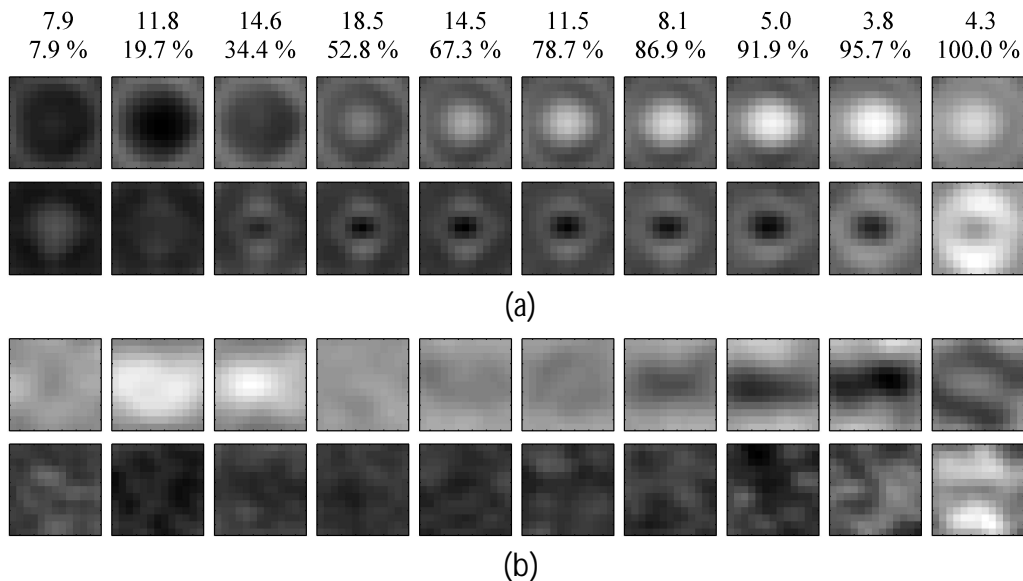


Figure 5: Raster dot clusters from the roughest paper (PPS 1.24 μm) printed at the lowest pressure (250 N). (a) Print reflectance, (b) Surface topography. See Figure 4 for details.

6 Conclusion

In this work we have examined the occurrence of missing or partly missing raster dots and their relation to the surface topography of unprinted paper. We have demonstrated the developed tools with SC paper samples printed by an IGT gravure test printer. To analyze the correspondence between surface topography and print reflectance, it is necessary to identify the dot locations. We have proposed a new method to locate robustly the subpixel coordinates of the raster dots and used the found coordinates to extract the raster dots from the print reflectance images.

We have found that the depressions in the surface topography moderately predict the missing ink in this gravure printing experiment. At maximum, 15 % of the exceptional surface depressions coincide with the locations of missing ink. As expected, this happens with the roughest SC sample used in the test. The effect of increasing printing nip pressure has also been studied, and the results imply that the pressure increase slightly improves the probability of finding missing ink from points that have been detected as surface depressions. However, the roughness of the paper samples has a larger impact on this predictive capability than the pressure. Applying SOM and hierarchical clustering to the raster dots has shown to be an efficient method for visualizing the large data set and for characterizing the print quality. The connection between small but deep paper surface depressions and missing printing ink is also visible in the clustering results, which encourages to use this method in the future analyses of paper surface properties and halftone print quality.

References

- [1] Barros, G.G.: Influence of substrate topography on ink distribution in flexography. Ph.D. thesis, Karlstad University (2006)
- [2] Bristow, J.A., Ekman, H.: Paper properties affecting gravure print quality. *TAPPI Journal*, 64(10):115-118 (1981)
- [3] Eerola, T., Kämäräinen, J.-K., Lensu, L., Kälviäinen, H.: Visual print quality evaluation using computational features. In: G. Bebis et al. (eds.) *Proceedings of the 3rd International Symposium on Visual Computing (ISVC 2007)*. Part I, pp. 403-413, Lake Tahoe (2007)
- [4] Geladi, P., Grahn, H.: *Multivariate Image Analysis*, John Wiley & Sons, Chichester (1996)
- [5] Hansson, P., Johansson, P.-Å.: Topography and reflectance analysis of paper surfaces using a photometric stereo method. *Optical Engineering* 39(9):2555-2561 (2000)
- [6] Heintze, H.U., Gordon, R.W.: Tuning of the GRI proof press as a predictor of rotonews print quality in the pressroom. *TAPPI Journal*, 62(11):97-101 (1979)
- [7] Hendry, I.F.: Some techniques for the assessment of coated art papers. *TAPPI Journal*, 44(10):725-731 (1961)
- [8] IGT Testing Systems: IGT Information leaflet W41 (2003)

- [9] Johnson, R.A., Wichern, D.W.: Applied multivariate statistical analysis, 4th ed., Prentice-Hall, Upper Saddle River (1998)
- [10] Khalaj, B.H., Aghajan, H.K., Kailath, T.: Patterned wafer inspection by high resolution spectral estimation techniques. *Machine Vision and Applications*, 7(3):178-185 (1994)
- [11] Kohonen, T.: Self-Organizing Maps, Series in Information Sciences, Vol. 30, Springer, Heidelberg (1995)
- [12] Lipshitz, H., Bridger, M., Derman, G.: On the relationships between topography and gloss. *TAPPI Journal*, 73(10):237-245 (1990)
- [13] MacGregor, M.A., Johansson, P.-Å., Béland, M.-C.: Measurement of small-scale gloss variation in printed paper. In: Proceedings of the 1994 International Printing and Graphic Arts Conference, pp. 33-43, Halifax (1994)
- [14] Mangin, P.J., Béland, M.-C., Cormier, L.M.: A structural approach to paper surface compressibility - relationship with printing characteristics. In: C.F. Baker (ed.) Transactions of the 10th Fundamental Research Symposium, Vol. 3, pp. 1397-1427, Oxford (1993)
- [15] Mettänen, M., Hirn, U., Lauri, M., Ritala, R.: Probabilistic analysis of small-scale print defects with aligned 2D measurements. Accepted for publication in: Transactions of the 14th Fundamental Research Symposium, Oxford (2009)
- [16] Mettänen, M., Ihalainen, H., Ritala, R.: Alignment and statistical analysis of 2D small-scale paper property maps. *Appita Journal*, 61(4):323-330 (2008)
- [17] Vartiainen, J.: Measuring irregularities and surface defects from printed patterns. Ph.D. thesis, Lappeenranta University of Technology (2007)
- [18] Vesanto, J., Alhoniemi, E.: Clustering of the self-organizing map. *IEEE Transactions on Neural Networks*, 11(3):586-600 (2000)
- [19] Welch, P.D.: The use of Fast Fourier Transform for the estimation of power spectra: A method based on time averaging over short, modified periodograms. *IEEE Transactions on Audio and Electroacoustics* 15(2):70-73 (1967)
- [20] Wolberg, G.: Digital Image Warping, IEEE Computer Society Press, Los Alamitos (1990)

Publication IV

Mettänen, M., Hirn, U., Lauri, M. and Ritala, R. (2009): Probabilistic analysis of small-scale print defects with aligned 2D measurements. *Trans. 14th Fundamental Research Symposium: Advances in Pulp and Paper Research* (ed. S.J. I'Anson), Oxford, UK, September 2009, pp. 1293-1323.

© 2009 The Pulp and Paper Fundamental Research Society. Reprinted, with permission, from Transactions of the 14th Fundamental Research Symposium.

PROBABILISTIC ANALYSIS OF SMALL-SCALE PRINT DEFECTS WITH ALIGNED 2D MEASUREMENTS

*Marja Mettänen¹, Ulrich Hirn², Mikko Lauri³
and Risto Ritala⁴*

^{1,3,4}Department of Automation Science and Engineering, Tampere University of Technology, P.O. Box 692, 33101 Tampere, Finland, ²Institute of Paper, Pulp and Fibre Technology, Graz University of Technology, Kopernikusgasse 24, 8010 Graz, Austria

ABSTRACT

We present an analysis of the pointwise relationship between the reflectance of print and the surface topography of the paper before printing. We have measured the surface topography and reflectance of paper before and after printing in a sheet-fed pilot offset printing press. The 2D measurement maps have been aligned to obtain local print reflectance and surface topography values for every spatial position on the samples. In contrast to the various deterministic modeling approaches, which imply an a priori defined underlying mathematical model, we apply probabilistic analysis. Therefore we first estimate joint probability density functions (pdfs) of local topography and print reflectance using Gaussian Mixture Models (GMMs). From these pdfs we select paper regions with unusual properties, i.e. regions from the tails of the pdfs. These anomaly maps are analyzed for interrelations between the print reflectance and surface topography, its gradient

¹ Corresponding author, email: marja.mettanen@tut.fi

and local variance. The degree of interrelation is characterized by the mutual information (MI), a measure to quantify statistical dependence without making assumptions about the linear or non-linear nature of the regression dependence. The significance of the MI values is confirmed by simulation based statistical hypothesis testing. The objective is to offer answers to the question: How does the observation of an exceptional topography point on the paper surface change our information about whether the print quality attainable at that point will be exceptional or not? The results suggest that topography in combination with its local variance have the most prominent interrelation to small scale print anomalies. Furthermore it is shown that regions with abnormal topography have at least ten-fold higher probability to exhibit exceptionally high print reflectance, compared to randomly selected regions.

1 INTRODUCTION

Earlier work in the research of paper related print unevenness has focused on identifying overall paper properties, such as PPS roughness, air leakage porosity or formation index that would explain variations in print quality. These studies (e.g. [1–3]) analyzed the relationship between paper properties and print quality, also including parameters related to ink properties and to the printing process. Print quality was assessed with ink demand, print-through and evenness of the scanned reflectance of printed area [4], or with subjective quality rankings [5]. Regression models in which print quality was explained in terms of paper properties were identified. Extensive studies were also published on identifying and evaluating the ink transfer equations that would relate the amount of ink transferred to the paper with the characteristics of the paper and the printing process (e.g. [6–8]).

In more recent work 2D measurements of local paper properties have been increasingly employed as many small-scale print defects can directly be related to inhomogeneities in the paper structure. Statistically significant correlations have been established between spatially aligned 2D measurements of paper surface topography, formation and print quality (local gloss or print reflectance) [9–12]. These studies have focused on identifying deterministic relationships, usually linear ones, between local paper properties and local print characteristics.

In our work we will also examine the relationships between a local paper

property, namely surface topography, and local print reflectance¹. However, we do not employ deterministic models, but instead we analyze the probabilistic relationship. Our key approach is to identify ‘abnormal’ regions in the paper by analyzing the (joint) probability density functions (pdfs) of the measured properties. By ‘abnormal regions’ we mean paper regions that have very unlikely, i.e. extreme, properties compared to the typical statistical behaviour of the data. Such regions correspond to values in the tails of the pdfs. Having identified the ‘abnormal’ regions we examine the relationship between surface topography and print reflectance in these regions. These relationships are quantified using mutual information (MI), a measure for the mutual dependence between the variables in the pdf. We compute MI from Gaussian Mixture Model (GMM) estimates [14, 15] of the joint pdfs of the abnormal points, which gives more stable results than computing MI directly from histograms [16]. We also examine conditional probabilities to quantify how much more likely it is that a print defect occurs at a point of an exceptional topography than on the average, and study how much the answer will depend on the size of the exceptional topography area.

This paper is organized as follows. In Section 2 we introduce the measurements analyzed in this work and describe the alignment of the measured 2D maps. Section 3 introduces the statistical analysis methods that we apply to the image data, and it also proposes two approaches to test the statistical significance of the analyses. Results are presented in Section 4 and conclusions are drawn in Section 5.

2 MEASUREMENT DATA

2.1 Measurements

In this work we concentrate on analyzing the dependence between the reflectance measurements of printed paper and the surface topography of the paper before printing. The applied topography measurement method is based on photometric stereo and it closely resembles the one presented in [17]. It is a camera-based measurement that provides reflectance and topography maps from exactly the same area of the paper sample. The test areas of paper samples have been imaged in this study both before and after printing. We interpret the reflectance measurement of the printed paper so that dark areas correspond to normal print quality and the bright spots in the reflectance

¹ This is not a true reflectance measurement (as described in [13]) but rather a photographic image of the paper surface.

map correspond to local print defects with missing or inadequate ink transmission. In the surface topography presentation, dark shades of gray are used to denote pits and light shades denote surface elevations.

The measurement data analyzed in this work is from a printing test where 16 newspaper sheets with PPS roughness of 2.61 μm , 2.77 μm , 3.16 μm or 3.63 μm (4 sheets each) have been printed with a sheet-fed pilot offset printing press. Each of the 16 paper sheets contains two test areas relevant for this work, both printed with full tone cyan. One of the areas has been printed with normal 4-colour offset settings with all four printing units pressing the paper. The other area has been printed so that only the cyan printing unit is in contact with the paper and thus the back-trap phenomenon is eliminated. On one of the paper sheets, the normal cyan area has been discarded from the analysis because the sheet has wrinkled at the printed area. The final number of imaged areas is thus 31, containing 15 normal cyan areas and 16 non-back-trap areas. The size of each imaged area is 22.5 mm by 15 mm and the image size is 2268 by 1512 pixels. This results in a pixel size of 10 μm by 10 μm .

The analyzed surface topography maps have been high-pass filtered with wavelength limit 250 μm , which emphasizes the sharp pits and elevations on the surface. A local variance map and a map of the local gradients in the printing direction have been computed from the high-pass filtered topography and used in the analyses as well. This allows also other surface properties than height to explain the print quality.

2.2 Image alignment

Accurate alignment of the 2D measurements is a prerequisite for the probabilistic analysis. The printed reflectance measurement is, due to the measurement method [17], already exactly aligned with the printed topography map, and the same holds for the measurements of the unprinted paper. Thus it is sufficient to register and align either the reflectance or topography measurements acquired before and after printing. We register the unprinted and printed topography maps because they resemble each other more than the unprinted and printed reflectance measurements.

The image registration is based on point mapping [18] that is the primary approach to register images with random textures. A set of matching points is searched from the reference and target images (i.e., the unprinted and printed topography maps) using cross-correlation coefficient of the surroundings as the similarity measure of the matching points. Typical values of the local cross-correlation maxima are above $r = 0.8$ when registering the topography maps. The subpixel coordinates of the cross-correlation maxima are

estimated by fitting a second order 2D polynomial to the surroundings of each cross-correlation peak. This provides the subpixel coordinates of the matching points. A global affine transformation [19] is fitted to the set of matching points and applied to the coordinates of the target image to overlay them with those of the reference image. Our registration is in two phases for accuracy, computational efficiency and robustness. The first phase estimates the translation only, and the second phase iteratively refines the transformation estimate, introducing also the rotation and shear deformation. When the selected affine transformation model is appropriate for the application, the transformation fitting error is less than 0.1 pixels [20]. The details on the image registration procedure have been presented in [20, 21].

The camera optics causes slight geometric distortion at the edges and corners of the images. As a result, the selected global affine transformation is not exactly the optimal way to warp the coordinates. The error that remains between the aligned coordinates may exceed one pixel in the corners of the image. To ensure accurate pointwise analysis of topography and print reflectance, only the parts of the images with less than half a pixel dislocation have been selected for the analysis. Still, the number of the pixels included on each of the 31 test areas is more than two million.

3 STATISTICAL ANALYSIS

After aligning the measurements, we analyze the dependence between the measured variables. We analyze probabilistic relationships instead of deterministic models because we do not want to restrict ourselves to an a-priori defined deterministic model between print reflectance and surface topography. In probabilistic analysis, we measure the interdependence of the variables based on their marginal, conditional and joint probability density functions (pdfs). Examples of pdf estimates for two variables are given in Figure 1. The *marginal pdf* of one variable is the 1-dimensional pdf calculated from the 2D pdf by integrating over the whole range of the other variable, Figure 1 (b-c). The *conditional pdf*, $f_{Y|X}(y|X=x)$, is the probability density of variable Y given a fixed value $X=x$, e.g. the print reflectance given that surface topography is $-3.5 \mu\text{m}$, Figure 1 (a,c). Such analysis reveals how much information we gain on the printed reflectance in a specified point by observing the value of the surface topography in that point.

Generally, a relatively small number of observations suffice to estimate reliably the pdfs of the variables in their normal value range. However, it is especially important to have reliable estimates for the tail regions of the pdfs because they represent the abnormal regions of paper we are interested in.

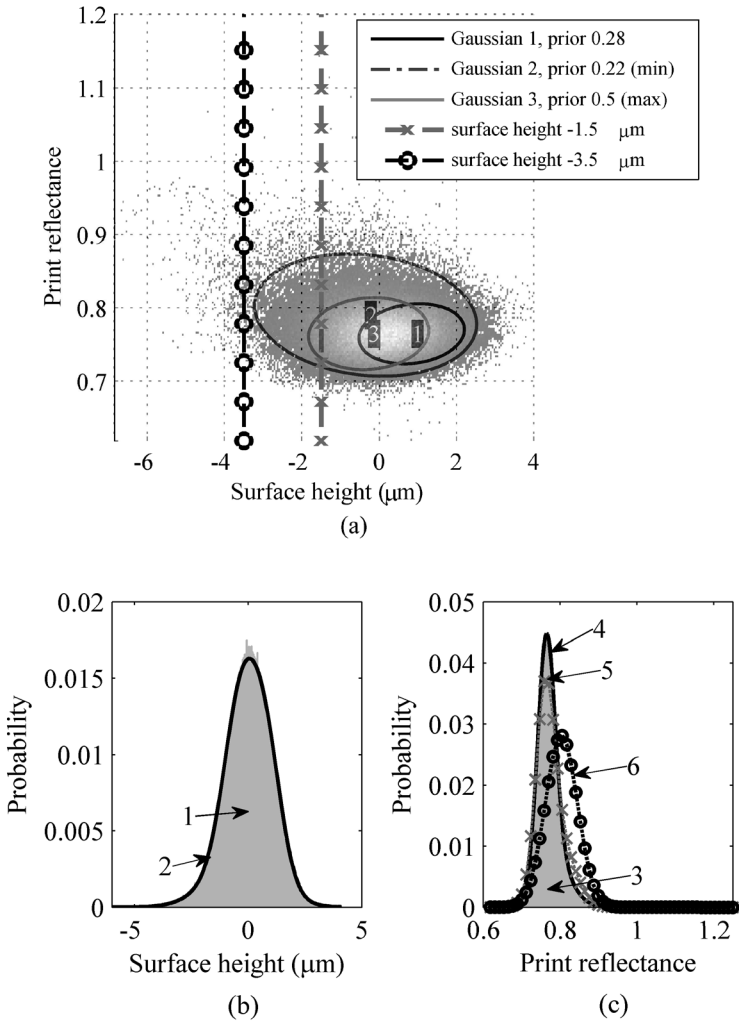


Figure 1. (a) Histogram-based and GMM-based joint pdf estimates of surface topography and print reflectance. The ellipses denote the 2σ equal probability contours of the components of the GMM. (b) Marginal pdf of surface topography (1: histogram-based, 2: GMM-based). (c) Marginal pdf of print reflectance (3: histogram-based, 4: GMM-based), and the conditional pdfs on condition that surface topography value is $-1.5 \mu\text{m}$ or $-3.5 \mu\text{m}$ (curves 5 and 6, respectively).

With image based measurements, we have huge amounts of data and thus we can obtain pdf estimates that describe reliably also the low-probability tail areas of the pdfs. Certain observed values can be classified as abnormal based on their falling into the tail area of the pdf. Thus we can analyze, how much information we have on the reflectance in a specified point given that the corresponding surface topography value has been deemed abnormal.

In this section, we first briefly introduce the GMM method by which we estimate the probability density functions. We study marginal and conditional pdfs and recognize the weak overall dependence between surface topography and print reflectance. Then we proceed to the selection of the abnormal points and study how they are located in the measurement area. As the first approach to verify the statistical significance of the analysis results, we present a method to test whether the abnormal points are spatially localized or just randomly and independently distributed in the plane. We then introduce the concept of mutual information (MI) to characterize the probabilistic dependence between two or more variables. Our second approach to verify the significance of the results consists of a comparison of the obtained MI values with the corresponding simulation results. The simulation is based on null hypothesis that print reflectance and surface topography are statistically independent. The last subsection provides more insight into the interpretation of the MI results by considering the probabilities of coincidences of abnormality in the measured variables.

3.1 Estimation of probability density functions

The joint probability density functions (pdfs) of the variables analyzed in this work differ clearly from Gaussian distributions. Thus they are estimated with Gaussian Mixture Models (GMMs) [14], known to describe complex multi-variate pdfs with quite few parameters. A GMM is a weighted sum of N Gaussian distribution components. For a d -dimensional random variable \mathbf{X} the pdf is described by GMM as

$$f(\mathbf{x}) = \sum_{i=1}^N c_i (2\pi)^{-d/2} (\det(\mathbf{C}_i))^{-1/2} \exp\left[-\frac{1}{2}(\mathbf{x} - \boldsymbol{\mu}_i)^T \mathbf{C}_i^{-1}(\mathbf{x} - \boldsymbol{\mu}_i)\right]. \quad (1)$$

Only three types of parameters are needed for each Gaussian component: the weight of the component c_i (prior), mean vector $\boldsymbol{\mu}_i$, and covariance matrix \mathbf{C}_i . The parameters can be estimated by the expectation maximization (EM) algorithm [22]. We apply the algorithm described in [23] which – unlike the standard EM algorithm – is capable of selecting the number of mixture components without supervision. It is worth noting that the true probability

distribution of the underlying random variable \mathbf{X} is unknown, and thus the estimation procedure is initialized randomly and it searches the optimal parameter values iteratively. Two GMM models trained with the same data thus differ slightly from each other but both are appropriate estimates of the true pdf when the number of points used for the estimation is high enough. We always use more than a thousand data points to estimate a GMM, which produces very robust results.

Figure 1 (a) gives an example of a 2D joint pdf approximated as the joint histogram and modeled as a 3-component GMM. The marginal pdfs of the variables are shown by the discrete histogram presentations and continuous GMMs in Figure 1 (b-c). In Figure 1 (c), two conditional pdfs of print reflectance are exemplified, given that the surface topography value is fixed either at $-1.5 \mu\text{m}$ or at $-3.5 \mu\text{m}$. In the former case, the conditional and marginal pdfs of print reflectance closely resemble each other, while the latter conditional pdf clearly deviates from the marginal pdf. This illustrates the fact that the statistical dependence between print reflectance and the unprinted surface topography is considerably stronger at the markedly low values of surface topography ($-3.5 \mu\text{m}$) than at the relatively typical topography values ($-1.5 \mu\text{m}$).

3.2 Selection of points based on abnormality

The overall dependence between surface topography and print reflectance is weak, as exemplified in Figure 1. This means that predicting the print reflectance in a specified point by measuring the surface topography in that point is highly uncertain in the general case: very little information in addition to that provided by the marginal pdf is gained. We therefore proceed to identifying and examining the abnormal points of the measured maps. The hypothesis is that the dependences are much more significant at the tail areas of the distributions.

3.2.1 Construction of the mask

A binary mask is constructed to select the abnormal points from the measurement data. The mask can be formed based on the joint pdf of the measured variables, or based on the extremeness of the values of single variables. Figure 2 exemplifies the mask identification procedure using the joint pdf of unprinted surface topography and print reflectance as a basis for the mask. The joint pdf is visualized by the joint histogram, and the line on top of the histogram denotes the mask criterion boundary. The mask selects the points outside the boundary, i.e. the points that correspond to the least likely

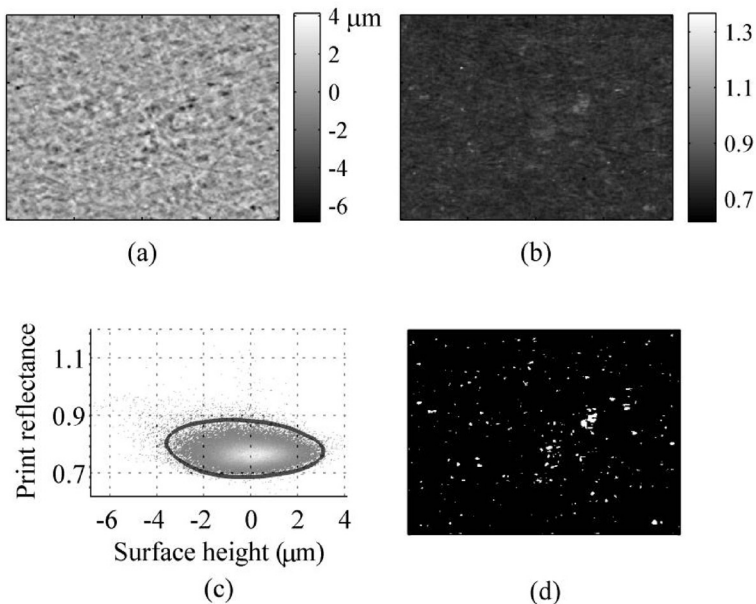


Figure 2. (a) Unprinted high-pass filtered surface topography and (b) print reflectance (reflected intensity in arbitrary units) on a 4 mm by 3 mm selection of a full tone cyan printing area. (c) Joint histogram of the variables together with the probability thresholding limit, $C(p)$ (gray curve), where $p = 1.5\%$. (d) The resulting mask that shows by white the 1.5% of pixels with the most unlikely combinations of topography and print reflectance.

p percent of the combinations of surface height and print reflectance. These points of the mask are given a value 1 while the rest of the mask assumes value 0. Figure 2 (d) shows the $p = 1.5\%$ of pixels that have the lowest values in the joint pdf, Figure 2 (c).

Mathematically, denoting the pdf of the (vector) variable \mathbf{X} as $f(\mathbf{X})$, the condition for an observation \mathbf{x} at location i to be abnormal to degree p is

$$f(\mathbf{x}) < C(p), \tag{2}$$

where the relationship between C and p is determined through

$$p = p(C) = \int_{f(\mathbf{x}) < C} f(\mathbf{x}) d\mathbf{x}. \tag{3}$$

The mask indicates those locations i that satisfy the above condition at the

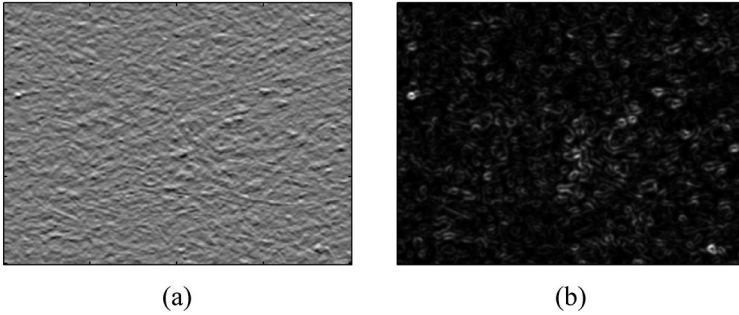


Figure 3. (a) Gradient and (b) local variance maps of the surface topography shown in Figure 2 (a). The gradient has been computed in the printing direction, i.e. y -direction. Both maps have been normalized to unit variance and thus the color bars are not shown.

chosen degree of abnormality, p . In other words, the selected points are responsible for the percentile p of the distribution of \mathbf{X} . In the case shown in Figure 2, the random variable \mathbf{X} is 2-dimensional, containing the observations of both surface topography and print reflectance.

We evaluate the relationship between surface topography and print reflectance in two setups: in ‘forward’ and ‘backward’ analysis. In the backward analysis we select regions with ‘abnormal print’, using the tail of the marginal pdf of print reflectance, and examine whether the topography might be responsible for these print defects. In forward analysis, we test how well the various selections of surface property characteristics are able to predict missing ink. The mask regions are selected according to paper surface properties: surface topography, its gradient and its local variance. We employ both the marginal and joint pdfs of the surface properties to select the abnormal points from the topography map, and then we examine the interrelation of these points with the local print reflectance. Figure 3 presents the gradient and variance maps corresponding to the surface topography shown in Figure 2 (a).

The mask construction methods that directly select the mask points from the tail areas of the pdfs, as discussed above, operate over the whole image area at once. We have additionally examined in the forward analysis a two-step mask construction procedure in which the selected areas are locally refined. This procedure is aimed to find regions with low topography values that additionally have large local variation in topography.

Step 1:

- a. Select a relatively small number, K , of the lowest values of the surface topography map.
- b. Assign a label to each connected group of pixels found. This produces a ‘seed mask’ with typically 100–200 labeled objects.

Step 2: Repeat for each seed object

- c. Set a window of size d by d pixels around the center of the seed object.
- d. Select a percentage q of the highest local variance values inside the window.
- e. Assign a label to each connected group of pixels found in the local window. This produces a local d by d mask with typically 1–5 labeled objects.
- f. Augment the seed object by the all the local labeled objects that have overlap with the seed object.

The result of the second stage is an augmented topography mask that takes into account the shape of the surroundings of the topography pits. We have used the following parameters in the algorithm: $K = 1000$, $K = 1500$ and $K = 2000$; $d = 35$; $q = 5\%$.

Unlike the other masks, a fixed mask percentage is not applied in this technique. Instead, the number of pixels selected by the mask depends on the content of the image and on the parameters defined above. We have applied very low values of K in the seed masks, which produces low mask percentages, typically $0.2\% \dots 0.5\%$. The choice of small K was made because the objective was to produce masks that differ clearly from the other forward masks. In addition, the labeling and processing of the seed objects becomes computationally demanding when the number of seeds increases. Table 1 summarizes the masks used in the analysis.

3.2.2 Spatial correlation of mask points

Studying the coincidence of abnormality at single pixel level is rather a limited perspective. We include the spatial aspect of abnormalities as follows. After constructing the mask, we examine how the masked points are distributed in the plane by counting the number of 1’s in the mask inside a sliding window. The statistical significance of the spatial extent of mask point areas is evaluated by comparing the result of the sliding summation to the null hypothesis of uniformly and independently distributed mask points. If the null hypothesis is true, the summation in the sliding window produces binomial distributed numbers. As the average mask coverage is small, it is

Table 1. Summary of masks.

<i>Analysis</i>	<i>Mask name</i>	<i>Points selected according to</i>	<i>Mask percentages</i>
Forward	Topo	lowest values of unprinted topography	0.2 % . . . 1.5 %
Forward	TGV	most unlikely combinations of topography, its (y-)gradient and its variance	0.2 % . . . 1.5 %
Forward	LocalVar	a low percentage of the lowest topography spots with local refining to take into account the variance of surface topography values around the selected pits	0.2 % . . . 0.5 %
Backward	Refl.	highest values of print reflectance	0.2 % . . . 1.5 %
Overall	Random	uniformly and randomly distributed points	0.2 % . . . 1.5 %

particularly efficient to test the null hypothesis by studying the distribution of the *maximum* number of points within the sliding window.

The null hypothesis can be simulated by repeatedly drawing M samples from a binomial distribution with parameters n and p , where n denotes the size (in pixels) of the sliding window and p is the mask coverage. We denote the samples as $N \sim \text{bin}(n, p)$. The number of samples, M , equals to the number of pixels in the image divided by n , i.e. the number of independent summation results obtainable in the image area. The histogram in Figure 4 (a) presents the distribution of $M = 10785$ samples from a binomial distribution with parameters $n = 225$ and $p = 0.015$, and implies that if the mask points were uniformly and independently distributed, a sliding 15 by 15 (i.e. 225) pixel window would almost always contain 10 mask points or less. The maximum of the M -sample set is recorded; the maximum in the simulation run shown in Figure 4 (a) was 12. To obtain a histogram estimate of the distribution of the *maximum* number of 1's in the mask inside a sliding window when the null hypothesis is true, we could repeat the experiment many times, each time recording the maximum value from the M -sample set. However, there is an analytical way. If the mask point positions are correlated, there will be more samples of exceptionally high density of points (inside a window) than according to the null hypothesis. Hence we choose as our decision variable the maximum of N among the M observations and call it N_{\max} . The probability that the random variable N_{\max} (in M observations) takes a given value

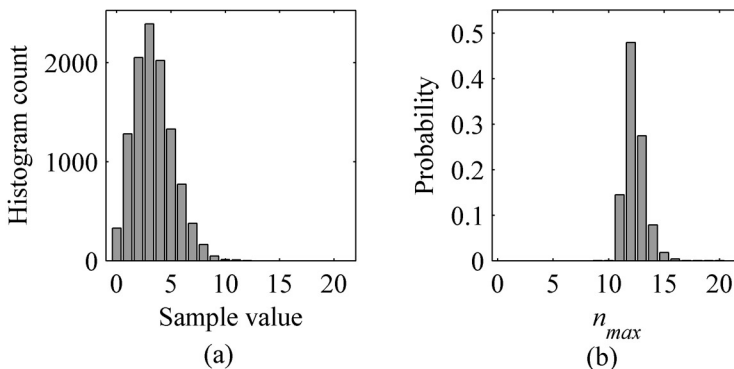


Figure 4. (a) Histogram of 10785 binomially ($\text{bin}(n,p)$) distributed random numbers with parameters $n = 225$ and $p = 0.015$. (b) Probability of the maxima of drawing 10785 samples from $\text{bin}(225,0.015)$.

n_{\max} , $P_{\max}(N_{\max} = n_{\max})$, can be calculated with standard order statistics. Figure 4 (b) illustrates such probability P_{\max} as a function of n_{\max} .

The idea behind this test is to show that the mask regions found by our procedures are much larger than for random masks. This indicates that the selected abnormal points are not uniformly placed but spatially correlated, i.e. they in fact represent regions of abnormal paper properties. The spatial correlation of the points of the mask under testing is statistically significant at points where the sliding summation result of the mask exceeds a chosen percentile, e.g. 99%, of P_{\max} .

We apply the simulation results in Section 4 and show that in our masks the number of 1's inside a sliding window exceeds the maxima of the binomial distributed numbers and thus our masks are not random.

3.3 Analysis of dependence through mutual information

3.3.1 Mutual information

Mutual information (MI) characterizes the interdependence of any two random variables, whatever the functional form of their joint pdf may be, and without making assumptions about the linear or nonlinear nature of their regression dependence. MI specifies how much the uncertainty about one variable is reduced by knowing the value of the other variable: it is a measure of how much information a variable carries about another variable. MI is symmetric and always non-negative – it reaches the value of zero if and only

if the variables are statistically independent. MI is calculated between the measured variables based on the pdf estimate. We use the parametric GMM presentation of the joint pdf instead of histogram because the former produces robust MI estimates whereas the histogram based MI depends heavily on the number of histogram bins [16]. Let us denote by \mathbf{X} and \mathbf{Y} the (possibly multidimensional) random variables. Let the joint pdf be $f(\mathbf{x}, \mathbf{y})$ and the marginal pdfs of \mathbf{X} and \mathbf{Y} $f_X(\mathbf{x})$ and $f_Y(\mathbf{y})$, respectively. The MI between \mathbf{X} and \mathbf{Y} , $I(\mathbf{X}; \mathbf{Y})$, is defined as [15]

$$I(\mathbf{X}; \mathbf{Y}) = \int_Y \int_X f(\mathbf{x}, \mathbf{y}) \log \left(\frac{f(\mathbf{x}, \mathbf{y})}{f_X(\mathbf{x})f_Y(\mathbf{y})} \right) d\mathbf{x} d\mathbf{y}. \quad (4)$$

If the logarithm is of base e , the unit of MI is nat, and with base 2 logarithm the unit is bit.

By the concept of mutual information, it is possible to examine any statistical dependences, without restricting the analysis to the Gaussian statistics as the standard correlation and R-squared analyses do. However, the interpretation of MI is less intuitive. In the case of jointly Gaussian distributions, the dependence between two variables, X and Y , is linear, and MI reveals information identical to the coefficient of determination of linear regression, R^2 . For joint Gaussian pdfs, MI is related to this familiar R-squared concept by [24]

$$I(X; Y) = -1/2 * \log(1 - R^2) \quad (5)$$

The same can be generalized to the Gaussian joint distributions of more than two variables by using the covariance matrix instead of a scalar correlation coefficient.

In a typical data analysis task the distributions are not Gaussian, and the above reasoning is inadequate. In practice, the absolute values of MI may not be as important as the maximization of MI with respect to certain criteria. This is the case, for instance, in various image registration applications where the objective in optimizing the image transformation parameters is to maximize the mutual information between the pair of images [25, 26]. In our analyses, the absolute MI values are also of less importance. We measure the MI between print reflectance and the topography-related variables and search for a topography-based strategy of selecting the abnormal points that maximizes the MI. Interpretations for the results are searched through comparisons and simulations, as described in the rest of this section.

3.3.2 Statistical significance of mutual information

We estimate MI from data sets selected by the masks described in Section 3.2.1. Because MI is by definition larger or equal to zero, the MI estimate from a finite data set is always larger than zero even if the sampled variables were statistically independent. To assess the statistical significance of the MI between random variables \mathbf{X} and \mathbf{Y} , we test by simulations, how estimated MIs are distributed when variables are statistically independent and the data set is of finite size.

The first idea to simulate statistically independent data sets might be to use white noise. However, when the masks are set up according to the true data, the simulated data must have spatial correlations identical to the ones in true data of each of the individual variables. Thus we need a procedure to make the topography and print reflectance maps statistically independent while maintaining their internal spatial structure. This can be achieved by randomizing one of the maps. We have chosen rather arbitrarily the topography map to be randomized.

The key idea in the randomization of the topography map is that the spectrum of the random map is kept identical to the spectrum of the original topography map, and hence the spatial autocorrelation of the data is kept identical as well. This is achieved through manipulation in the Fourier domain. The high-pass filtered surface topography map is first transformed into the Fourier domain by 2D Fast Fourier Transform (FFT). Then the phases at each frequency are chosen as randomly and uniformly distributed values between 0 and 2π while keeping the amplitude unchanged. Finally the 2D inverse FFT of the modified Fourier transform produces a topography map whose variance and spectrum are identical to those of the original map but which is uncorrelated with the original map. We refer to the resulting image as random-phase topography. Figure 5 presents a comparison of the original and simulated topography maps, their spectra and the corresponding pdfs. The original and simulated pdfs differ slightly because the original pdf was not Gaussian which would be a prerequisite to preserve the exact pdf. The slight differences between the original and simulated spectra are caused by the finite size of the image: edge effects are not simulated in the random phase spectrum.

Figure 6 gives an example of simulated and true MI values between surface topography and print reflectance. Both the true and simulated cases employ the true print reflectance map and select the data points using a locally refined topography mask (LocalVar mask with $p = 0.3\%$), but the simulation uses random-phase topography images in the place of the true topography measurement. Both sets of results have variance larger than zero but the MIs

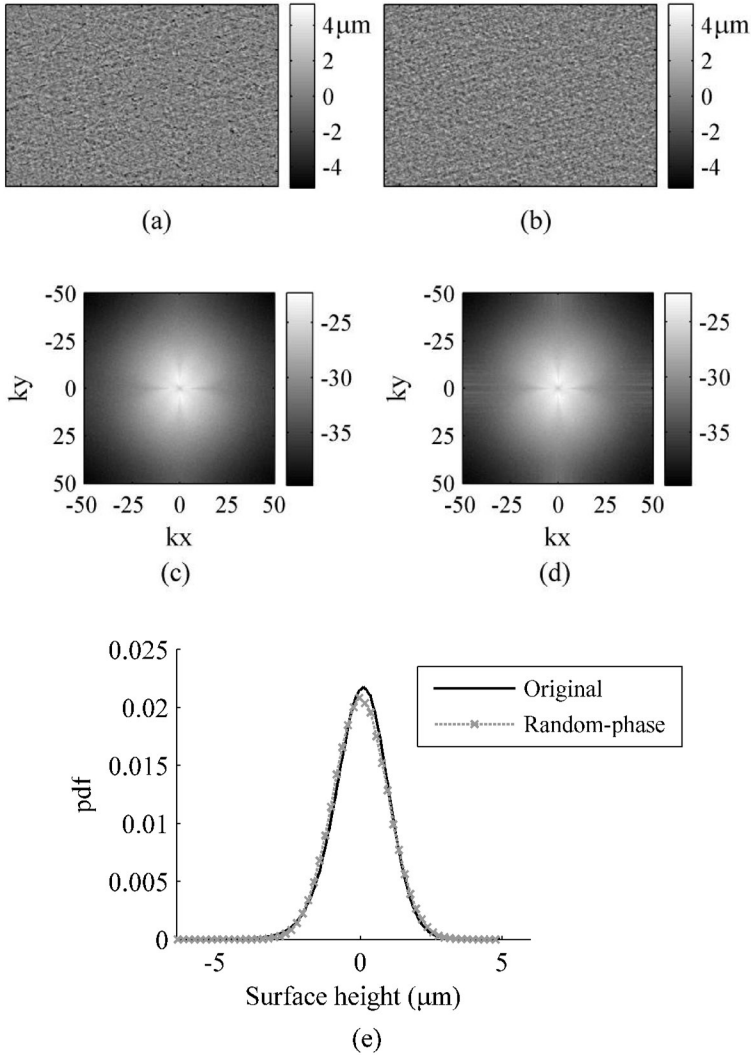


Figure 5. Simulation of topography by randomizing the phase information. (a) Original surface topography on a 9 mm by 6 mm selection, (b) corresponding random-phase topography, (c) logarithm of the 2D spectrum of the original topography, (d) logarithm of the 2D spectrum of the random-phase topography, (e) marginal pdfs of the original and random-phase topography images.

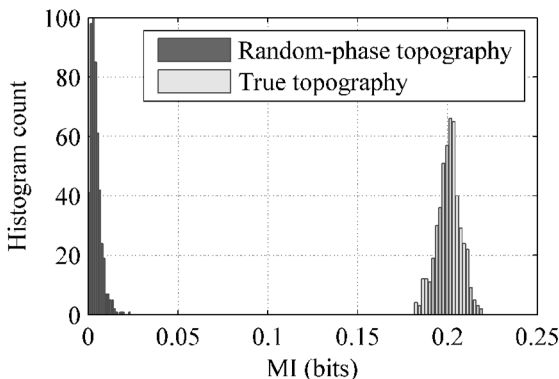


Figure 6. Histogram of 500 MI values computed between print reflectance and simulated topography and comparison with 500 repetitions of MI computation using the true data from one of the non-back-trap cyan samples.

computed from true data are always much higher than the simulated MIs. The differences in MI between repeated calculations are caused by three factors. Firstly, since we are estimating the pdfs by GMM using a different random initialization each time, the GMM estimates differ slightly from each other even if the input data stays exactly the same. Secondly, the numerical integration applied in the MI computation causes minor deviation to the results. Thirdly, in the simulation, we generate a new random-phase topography data at each simulation experiment.

3.4 Coincidence of abnormalities

As the final analysis method, we examine the coincidence of abnormalities in the measurements. We classify the observations of topography and print reflectance into normal or abnormal classes individually – with their marginal probabilities – and then compute the probabilities of coincidences of abnormality, $p(y \neq \text{normal} \mid x \neq \text{normal})$. This resembles the technique used in [9]. Specifically, we measure the probability of having a print defect in a spot that has been deemed abnormal based on its surface topography. We also examine the dependence of the results on the size of the exceptional topography spot.

We do not have subjective evaluations or other references to classify the values of the print reflectance map as normal or abnormal. Therefore masking is based on the selected degree of abnormality, i.e., the selected percentile

of the pdf that determines where the ‘normal’ part of the pdf turns into the ‘abnormal’ tail. Various mask percentages are tested. We apply the same mask percentage to both the print reflectance map and the surface topography map, and then examine the overlap of the masks. If the occurrence of an abnormality in the print reflectance does not depend on the classification (normal/abnormal) of the corresponding spot in the surface topography map, the expected overlap of the masks equals the selected mask percentage. The results presented in Section 4 show that the overlap percentages are considerably larger than that. This will provide a new insight into the interpretation of the MI results as well.

4 RESULTS

Masks with abnormality degree, p , varied between 0.2 % and 1.5 % have been generated for the whole set of images. The masks indicate the p percent most abnormal points of the variables and their combinations according to the ‘forward’ and ‘backward’ approaches introduced in Section 3.2.1. The backward approach applies a mask that indicates the highest values of the print reflectance map (Refl. mask) and the forward approach applies three topography-based masks (Topo, TGV, and LocalVar masks) as listed in Table 1. In addition, we have used a random mask in which the number of points specified by p is distributed independently and uniformly on the image area. This corresponds to modeling the overall dependence between print reflectance and unprinted topography, without classifying the observations into normal or abnormal categories.

In this section, we first verify the spatial correlation of the mask points by comparing the masks with the null hypothesis of randomly and independently distributed mask points, as described in Section 3.2.2. Then, for each mask, we estimate the joint pdf of the variables in the points indicated by the mask, and calculate the mutual information from the pdf. The statistical significance of the MI results is evaluated by comparing the results with simulations that use random-phase surface topography instead of the original aligned topography map, as described in Section 3.3.2. Finally, we study the overlap of the forward and backward masks and show that observing an exceptional value in the surface topography map provides useful information for predicting the occurrence of a print defect in that point.

4.1 Spatial correlation of mask points

We test whether the positions of mask points in the image are correlated or not, the null hypothesis being that no correlation exists. Let us study a win-

dow of \sqrt{n} by \sqrt{n} pixels within the image. If the mask point positions are not correlated, then the number of mask points within such window is binomially distributed $N \sim \text{bin}(n, p)$, where p is the proportion of masked points in all the points (i.e. the mask percentage). If the image size is \sqrt{m} by \sqrt{m} pixels we may generate $M = m/n$ independent samples of N . If the mask point positions are correlated, there will be more samples of exceptionally high density of points and exceptionally low density of mask points than according to the null hypothesis. Hence we choose as our decision variable the maximum of N among the M observation and call it N_{\max} .

As noted in Section 3.2.2, the probability that N_{\max} (in M observations) takes a given value n_{\max} , $P_{\max}(N_{\max} = n_{\max})$, can be calculated with standard order statistics. The probability in the case $n = 225$, $p = 0.015$ and $M = 10785$, corresponding to the mask parameters studied in Figure 4 in Section 3.2.2, is shown in Figure 7 (a). The probability that N_{\max} exceeds the value $n_{\max} = 17$ is 0.001. Figure 7 (b) gives a typical example of observed distribution of number of mask points per 15 by 15 pixel windows with 10785 independent observations in total. The maximum of these is over 100. Hence the null hypothesis is rejected on a confidence level of 0.001 and we conclude that the positions of mask points in the images are correlated.

For all paper samples, the Topo, TGV and Refl. masks with 5 mask percentages varying between 0.2 % and 1.5 % have been analyzed by the sliding summation technique using window sizes from 10 by 10 pixels to 30 by 30

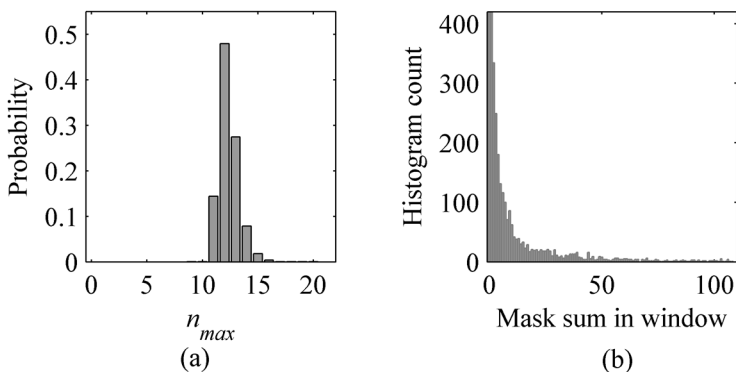


Figure 7. (a) Probability of the maxima of random variables from binomial distribution $\text{bin}(255, 0.015)$. (b) Histogram of the 10785 sums of a 1.5 % TGV mask inside a sliding window of size 15 by 15 (255) pixels. The axes in (b) have been zoomed for visualization: the highest peak was 8208 and the last non-zero bin was 181.

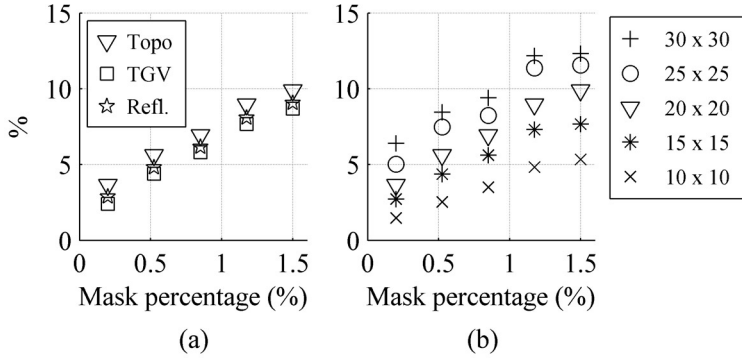


Figure 8. The proportion of the mask pixels that are to a very high probability spatially concentrated. (a) Topo, TGV and Refl. masks with window size 20 by 20 pixels, (b) Effect of window size demonstrated with the Topo mask. In (b), the reference binomial distribution corresponding to a marker has parameters n and p , where n is denoted by the marker type and p is the location of the marker on the x -axis.

pixels. Each time the histogram of the sliding summation results has been compared with the corresponding maxima histogram obtained from the repeated binomial distribution sampling. We have counted how large proportion of the independent sliding summation results exceeds the 99 % percentile of the maxima distribution such as that shown in Figure 7 (a). This is a measure for the proportion of mask pixels that is to a very high probability spatially concentrated. Figure 8 (a) presents the results for the three mask types with the window size fixed to 20 by 20 pixels. The local concentrations of the mask points are slightly more frequent in the Topo mask than in TGV and Refl. masks. Figure 8 (b) uses the Topo mask again to illustrate the effect of the sliding window size on the results. In conclusion, Figure 8 confirms that, independent of the selected mask percentage and type, there are always numerous locations in the mask where the local sum of the mask points exceeds the value that it would most likely maximally have if the mask points were randomly and independently distributed. The proportion of the significantly spatially concentrated mask points increases with the mask percentage.

4.2 Mutual information and its significance

With each mask, we have estimated by GMM the joint pdf of the masked points of the four maps: print reflectance (R), surface topography (T), the

gradient of surface topography (G), and the local variance of surface topography (V). This joint pdf estimate is used to compute the mutual information between print reflectance and the topography-related variables and their combinations. From all possible combinations of datasets we report the results for the four combinations that contain reflectance and topography: RT, RTG, RTV and RTGV. It is thus possible to assess whether the gradient of the surface is a better predictor of print reflectance than the local variance of the surface topography, or vice versa.

To assess the statistical significance of the MI results computed based on the measurements, the corresponding MI values have been computed using simulated random-phase surface topography data together with the true reflectance measurements. In this analysis, the simulated topography map replaces the true topography before the gradient and variance maps are computed. The simulated topography map thus preserves its relationship with the gradient and variance maps like the original topography map. As described in Section 3.3.2, the simulation also preserves the spatial correlations of the original topography map, as well as the marginal pdf. When the simulated topography data is used in GMM estimation and MI computation together with the original reflectance map, the dependences are very weak because the topography is random with respect to the reflectance. The simulated case thus serves as a reference and indicates the level of MI attainable even with random data when the sample size is finite.

The smallest masks select 0.2 % of the points of the measurement maps (that is approximately 5000 data points) while the largest mask selects 1.5 %. The mask percentage slightly affects the MI values but the effect depends on the type of mask used. The results of the MI analysis are reported in Table 2 for the non-back-trap samples and in Table 3 for the normal samples. Comparison of the values shows that the interdependence between topography and print reflectance is stronger in the samples printed without back-trap conditions than with normal printing conditions. This seems reasonable since back-trap related print unevenness is also linked to paper properties like formation or porosity variations [27] which are not related to small-scale topography variations.

The MI values given in the tables are the average results of the 16 non-back-trap or 15 normal samples. The tables report the lowest and highest mask percentages used, and the MI results obtained with 0.3 . . . 1.2 % masks fall between these values. The standard deviations corresponding to the MI averages are not given in the tables but Figures 9 and 10 illustrate the deviation in the form of 95 % confidence limits.

Figure 9 shows a graphical view of the ‘forward’ analysis results with 0.37 % masks, and Figure 10 respectively the ‘backward’ analysis results with

Table 2. Average mutual information between topography characteristics and print reflectance for the 16 non-back-trap Cyan samples in forward and backward analyses, and overall (using the random mask). (*) Mask based on random-phase topography and applied to the same random-phase topography with true reflectance data. (**) Mask based on reflectance and applied to the same reflectance with random-phase topography. (***) Random mask applied to true reflectance and random-phase topography.

Mask	MI (bits) with $p = 0.2\%$					MI (bits) with $p = 1.5\%$						
	RT	RTG	RTV	RTGV	RT	RTG	RTV	RTGV	RT	RTG	RTV	RTGV
Forward												
LocalVar	0.27	0.33	0.34	0.39	–	–	–	–	–	–	–	–
TGV	0.25	0.31	0.30	0.37	0.17	0.20	0.22	0.25	0.15	0.15	0.15	0.15
Topo	0.06	0.08	0.10	0.11	0.09	0.12	0.14	0.15	0.06	0.06	0.06	0.06
RandPhase (*)	0.006	0.04	0.03	0.07	0.007	0.03	0.02	0.06	0.007	0.03	0.02	0.06
Backward												
Refl.	0.06	0.12	0.15	0.25	0.04	0.10	0.13	0.20	0.04	0.10	0.13	0.20
Refl.+RP (**)	0.01	0.06	0.08	0.16	0.003	0.04	0.06	0.12	0.003	0.04	0.06	0.12
Overall												
Random	0.04	0.07	0.10	0.12	0.03	0.06	0.09	0.11	0.03	0.06	0.09	0.11
Random+RP (***)	0.001	0.02	0.02	0.05	0.001	0.01	0.02	0.04	0.001	0.01	0.02	0.04

Table 3. Average mutual information between topography characteristics and print reflectance for the 15 normal Cyan samples in forward and backward analyses, and overall (using the random mask). (*) – (**), see Table 2.

Mask	MI (bits) with $p = 0.2\%$					MI (bits) with $p = 1.5\%$						
	RT	RTG	RTV	RTGV	RT	RTG	RTV	RTGV	RT	RTG	RTV	RTGV
Forward												
LocalVar	0.20	0.28	0.27	0.34	–	–	–	–	–	–	–	–
TGV	0.17	0.25	0.23	0.32	0.11	0.15	0.16	0.19	0.11	0.15	0.16	0.19
Topo	0.08	0.10	0.13	0.14	0.08	0.12	0.14	0.15	0.08	0.12	0.14	0.15
RandPhase (*)	0.01	0.04	0.03	0.06	0.006	0.02	0.02	0.04	0.006	0.02	0.02	0.04
Backward												
Refl.	0.03	0.09	0.12	0.21	0.02	0.08	0.10	0.18	0.02	0.08	0.10	0.18
Refl.+RP (**)	0.01	0.06	0.08	0.16	0.003	0.04	0.06	0.12	0.003	0.04	0.06	0.12
Overall												
Random	0.02	0.04	0.06	0.08	0.02	0.04	0.07	0.08	0.02	0.04	0.07	0.08
Random+RP (***)	0.002	0.02	0.02	0.05	0.001	0.02	0.01	0.03	0.001	0.02	0.01	0.03

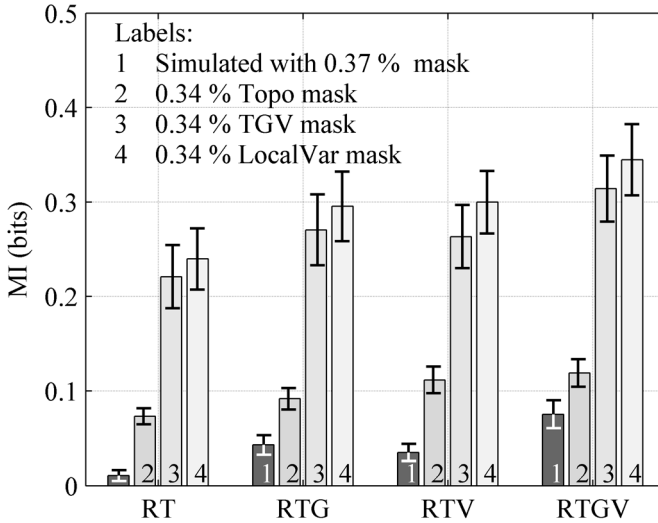


Figure 9. Comparison of MI in true topography-based masks and random-phase simulations for non-back-trap Cyan samples. Mutual information has been evaluated between the combinations of variables denoted on the horizontal axis. The whiskers at the end of the bars indicate the 95% confidence limits among the 16 samples.

the same mask percentage. The labeled bars in Figures 9 and 10 correspond to the masks listed in Tables 2 and 3. ‘Forward’ refers to the fact that abnormal points are identified based on paper surface properties that may give a prediction for the print result. ‘Backward’ means that the abnormal regions are identified from the print, which may be used to analyze the print defects. The overall mutual information results, computed without the identification of any abnormalities and given at the bottom of Tables 2 and 3, have not been plotted but they can be compared in the tables with the corresponding simulated results that use random-phase topography in the place of the true topography. The comparison shows that even though the overall dependence between surface topography and print reflectance is weak, it is consistently higher than the MI computed from random data.

According to Figure 9, the highest MI results are obtained by selecting the points by the locally refined topography mask that accounts for the variance in the surroundings of the selected topography pits (LocalVar mask). This masking strategy seems to be best suited to select regions in which the paper surface properties and print reflectance have significant statistical dependence. The mask based on the joint distribution of the three topography-

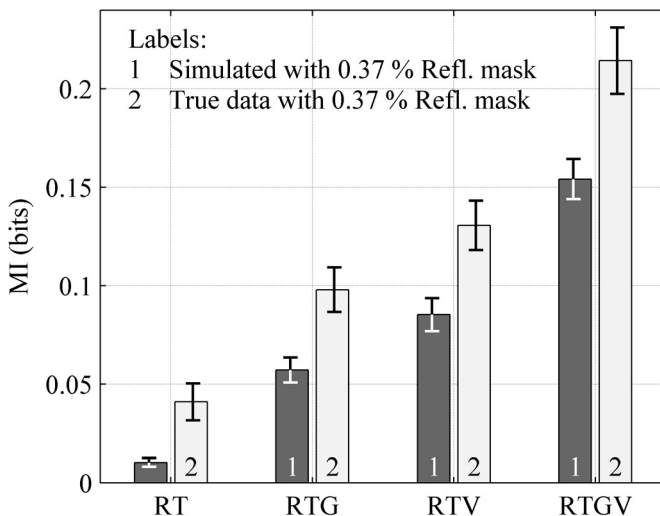


Figure 10. MI computed using true data from non-back-trap Cyan samples or a data set where the topography map has been replaced by random-phase topography. Both cases use a reflectance-based mask with $p = 0.37\%$. Mutual information has been evaluated between the combinations of variables denoted on the horizontal axis. The whiskers at the end of the bars indicate the 95% confidence limits among the 16 samples.

related variables (TGV mask) provides the second highest mutual information between the print reflectance and the explanatory variables. Comparison between TGV mask and Topo mask shows that surface topography, its gradient and local variance together reveal more interrelation between topography and reflectance than the topography map alone.

Mutual information between a set of variables can only increase or stay the same when the number of variables increases, because a new variable introduced in the joint pdf model can never reduce the dependences that have already been described by the model. Therefore the MI values – also the simulated ones – presented in Figures 9 and 10 increase from left to right, when the RT combination is switched to RTG or RTV, and further when proceeding to the 4-variable combination, RTGV. As the simulated values also increase, it is justified to assess how the MI develops in the variable combinations and masking strategies with respect to the simulated MI (the dark gray bars). Based on this comparison between the true data-based MI and the respective simulated results, MI is higher in the RTV combination

than in the RTG combination in the backward mask and all forward masks, except the TGV mask. This implies that the local variance of surface topography may be a slightly better predictor of the print reflectance than the gradient of topography. Comparing the 3-variable and 4-variable combinations in the forward case reveals that MI is not significantly higher in the combination of all the four variables than in a combination of three variables where either the gradient or local variance of the surface topography has been excluded. In the backward analysis the fourth variable introduces some new information. This means that, for the prediction of print reflectance in the abnormal points of surface topography, the information between V and G is redundant, but when explaining the observed print anomalies by the topography characteristics, both the gradient and the variance carry useful information.

Finally, Figures 9 and 10 show that the dependence between surface topography properties and print reflectance is, on average, weaker in the print defect spots than in the spots of abnormal surface topography, because print defects are also caused by other paper properties than surface topography. However, identifying the abnormal topography points does facilitate the prediction of print reflectance.

4.3 Coincidence of abnormalities

The coincidences of the ‘forward’ masks with the ‘backward’ masks have been evaluated to measure the probability of observing an abnormally high value in the print reflectance map on condition that the surface topography in that point has been classified abnormal. The forward masks are the Topo, TGV and LocalVar masks that were used in the MI analyses as well, and the backward mask is the one that selects points of exceptionally high print reflectance. The coincidence analysis always applies the same mask percentage, p , for the forward and backward masks, studying the range from $p = 0.2\%$ to $p = 1.5\%$.

The typical overlap of topography abnormalities with the points of unusually high print reflectance varies from 7 % to 12 % in the normally printed cyan samples and from 10 % to 18 % in the non-back-trap cyan samples. The Topo mask produces slightly higher overlaps than the LocalVar or TGV masks. The overlap percentages in all the cases are considerably larger than the probability for an accidental coincidence of the masks which equals p . As the mask percentage is increased, both the accidental and the realized overlaps of the topography and print reflectance abnormalities increase, but within the low mask percentages studied in this work, the latter increases considerably faster (as a function of p) than p itself. This means that

the increase in the overlap is a result of true coincidence of abnormal regions in surface topography and print reflectance.

The forward masks have also been divided into sub-masks that only contain objects (connected group of pixels) of specified sizes, and their coincidence with the reflectance mask has been measured as the proportion of overlapping pixels. This reveals, as a function of the size of the exceptional topography area, the probability of observing an unusually high print reflectance on condition that the topography shows abnormal behavior.

Figure 11 presents the overlap results, averaged over the 16 non-back-trap samples within each mask type. For Topo and TGV masks, the smallest and largest mask percentages are presented, Figure 11 (a-d). In the locally refined topography masks the range of mask percentages is so narrow ($p = 0.2 \% \dots 0.5 \%$) that one diagram represents the results sufficiently. In the averaging between the paper samples, the overlaps in each size category have been weighted by the number of (the specified size) objects found in each sample. The variance of the overlap results among the paper samples is high in the size categories where the number of objects is relatively low. However, the results clearly show that, also inside the size categories, the surface topography anomalies coincide with print defects with a considerably higher probability than the accidental probability, p .

The results presented in Figure 11 cover the range of overlaps detected with the various mask construction techniques and mask percentages. The regions selected by the Topo mask show increasing overlap with the reflectance mask when the size of the abnormal topography regions increase, as illustrated in Figure 11 (a,b). With the TGV masks this tendency is not as strong as with Topo masks. The average overlap between the TGV mask regions and reflectance mask remains between approximately 10 % and 20 % over the range of object size categories in Figure 11 (d) where $p = 1.5 \%$. At the lowest mask percentage ($p = 0.2 \%$), Figure 11 (c), the TGV mask selections do not coincide with the brightest print reflectance points so well. Figure 11 (e) shows that abnormal topography regions of small size have particularly high overlap with the mask of print defects, if these topography regions are selected by the LocalVar mask. The differences in the results between the mask types are addressed to the fundamentally different methods of constructing the masks. The TGV and LocalVar masks tend to select larger individual regions of the topography map than the Topo mask because the former are based on the properties of the surroundings of the topography depressions, and not only the topography values as such. Overall, this reason reduces the overlap of the TGV and LocalVar masks with the corresponding reflectance mask.

Topo mask reaches the largest overlap with the print defects, whereas

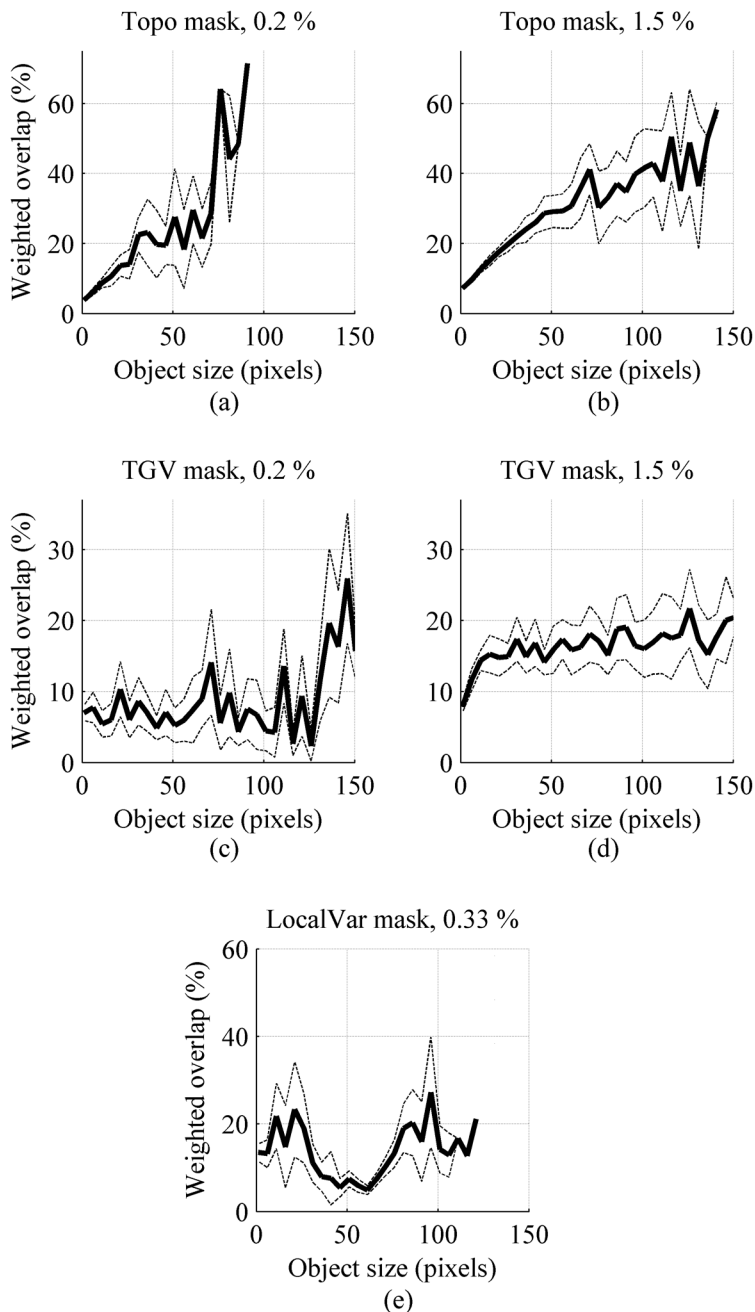


Figure 11. Overlap of the reflectance mask with the forward masks as a function of the size of objects picked from the forward masks. (a) Topo mask with $p = 0.2 \%$, (b) Topo mask with $p = 1.5 \%$, (c) TGV mask with $p = 0.2 \%$, (d) TGV mask with $p = 1.5 \%$, (e) LocalVar mask with $p = 0.33 \%$. The dashed lines represent the 95 % confidence limits of the 16 non-back-trap results.

Section 4.2 showed that the mutual information between print reflectance and surface properties is not as high in the Topo mask as in the other forward masks. This may be due to the fact that Topo mask causes an abrupt edge to the space of topography observations, since the mask selects points in which the topography values fall below a certain threshold. Hence the GMMs are not able to describe the joint pdf of the surface properties and print reflectance in a similar precision as in the case of TGV and LocalVar mask points. It must also be noted that mutual information describes basically different interrelations than the plain overlap of two binary masks.

5 CONCLUSIONS

We have estimated the pointwise joint probability density functions of print reflectance and surface topography characteristics of newsprint paper printed in a sheet fed pilot offset press. We have studied the mutual relationships both throughout the observation range and in anomalous points, i.e. points with unusual topography or print reflectance. Applying GMMs and MI we have suggested a procedure to identify regions on the paper with exceptional values of topography, topography gradient and topography variance. These regions have a highly increased – at least tenfold – probability to have extremely high print reflectance, compared to randomly selected regions.

Our results have shown that topography, its gradient and its local variance all contribute to identifying the regions where the surface characteristics and print reflectance have stronger than average interdependence. Independent of the search strategy for the identification of regions with exceptional topography, the modeling results inside these regions always suggest that surface topography in combination with its local variance are the most important variables to describe the interrelation between small-scale paper surface topography and local print reflectance. We have confirmed the statistical significance of our results by showing that unrelated data with the same statistical and spatial correlation properties as the true data shows negligible values for MI compared to the interrelations revealed by our analysis.

The probabilistic approach, which does not assume an underlying mathematical model describing the interrelations between target variable, i.e. print reflectance, and its explanatory variables (e.g. topography), provides a viable alternative to the various deterministic modeling approaches that need a priori formulation of a model. The simulation methods that have been developed to prove the statistical significance of the mutual information found between the analyzed variables provide a quantitative interpretation

for MI. This might contribute to a better applicability of information theoretic analysis methods in pulp and paper research.

REFERENCES

1. J.M. Fetsko and A.C. Zettlemoyer. Factors affecting print gloss and uniformity. *Tappi* **45**(8):667–681, 1962.
2. J.R. Parker. Fundamental paper properties in relation to printability. In **The Fundamental Properties of Paper Related to Its Uses**, *Trans. 5th Fund. Res. Symp.*, (ed. F. Bolam), pp517–543, BPBIF, London, 1976.
3. S.T.P. Karttunen. Structure and behaviour of a paper's surface in printing. In **The Fundamental Properties of Paper Related to Its Uses**, *Trans. 5th Fund. Res. Symp.*, (ed. F. Bolam), pp544–560, BPBIF, London, 1976.
4. B. Lyne. Machine-calendering: implications for surface structure and printing properties. *Tappi J.* **59**(8):101–106, 1976.
5. I.F. Hendry. Some techniques for the assessment of coated art papers. *Tappi* **44**(10):725–731, 1961.
6. W.C. Walker and J.M. Fetsko. A concept of ink transfer in printing. *American Ink Maker* **33**(12):38–71, 1955.
7. I. Ichikawa, K. Sato and Y. Ito. A new concept of ink transfer equation. *Research Bulletin of the Government Printing Bureau*, Japan, No. 1, 1962.
8. P.J. Mangin, M.B. Lyne, D.H. Page and J.H. De Grâce. Ink transfer equations – parameter estimation and interpretation. In proc. *Adv. in Printing Science and Techn.*, (ed. W.H. Banks), Vol. 16, pp180–205, Pentech Press, London, 1982.
9. G.G. Barros. Influence of substrate topography on ink distribution in flexography. PhD Thesis, Karlstad University, Sweden, 2006.
10. I.M. Kajanto. Pointwise dependence between local grammage and local print density. *Paper and Timber* **73**(4):338–345, 1991.
11. M.A. MacGregor, P.-Å. Johansson and M.-C. Béland. Measurement of small-scale gloss variation in printed paper. In proc. *1994 Int. Printing and Graphic Arts Conf.*, pp33–43, Halifax, 1994.
12. A. Dickson. Evaluating the relationship between grammage, topography and print properties in newsprint. In proc. *60th Appita Annual Conference*, pp19–23, Melbourne, 2006.
13. H.F. Rance (ed.). *Handbook of paper science*. Elsevier, Amsterdam, 1982.
14. I.T. Nabney. *Netlab: Algorithms for pattern recognition*. Springer-Verlag, London, 2002.
15. C.M. Bishop. *Pattern recognition and machine learning*. Springer, Singapore, 2006.
16. R. Steuer, J. Kurths, C.O. Daub, J. Weise and J. Selbig. The mutual information: Detecting and evaluating dependencies between variables. *Bioinformatics* **18**(Suppl.2):231–240, 2002.
17. P. Hansson and P.-Å. Johansson. Topography and reflectance analysis of paper

- surfaces using a photometric stereo method, *Optical Engineering* **39**(9):2555–2561, 2000.
18. L. Brown. A survey of image registration techniques. *ACM Computing Surveys* **24**(4):325–376, 1992.
 19. G. Wolberg. Digital image warping. IEEE Computer Society Press, 1990.
 20. M.R. Lähdekorpi, H.A.T. Ihalainen and R.K. Ritala. Using image registration and alignment to compare alternative 2D measurements. In proc. *XVIII IMEKO Word Congress*, Rio de Janeiro, 2006.
 21. M.R. Mettänen, H.A.T. Ihalainen and R.K. Ritala. Alignment and statistical analysis of 2D small-scale paper property maps. *Appita Journal* **61**(4):323–330, 2008.
 22. A.P. Dempster, N.M. Laird and D.B. Rubin. Maximum likelihood from incomplete data via the EM algorithm. *J. Royal Statistical Soc. Series B* **39**(1):1–38, 1977.
 23. M.A.T. Figueiredo and A.K. Jain. Unsupervised learning of finite mixture models. *IEEE Trans. Pattern Analysis and Machine Intelligence* **24**(3):381–396, 2002.
 24. S. Kullback. Information theory and statistics. Dover Publications, Inc., Mineola, New York, 1997.
 25. P. Viola and W.M. Wells. Alignment by maximization of mutual information. *International J. of Computer Vision* **24**(2):137–154, 1997.
 26. B. Zitova and J. Flusser. Image registration methods: a survey. *Image and Vision Computing* **21**(11):977–1000, 2003.
 27. I. Kajanto. The effect of formation on print quality with woodfree offset papers. *Nordic Pulp and Paper Res. J.* **4**(1):8–15, 1989.

Publication V

Mettänen, M. and Ritala, R. (2009): Measurement as information channel with an application to printability. *Proc. XIX IMEKO World Congress*, Lisbon, Portugal, September 2009, pp. 1086-1090.

© 2009 IMEKO. Reprinted, with permission, from Proceedings of the IMEKO XIX World Congress. Publication available at www.imeko.org.

MEASUREMENT AS INFORMATION CHANNEL WITH AN APPLICATION TO PRINTABILITY

Marja Mettänen, Risto Ritala

Tampere University of Technology, Department of Automation Science and Engineering
P.O. Box 692, 33101 Tampere, Finland, e-mail: firstname.lastname@tut.fi

Abstract – Printability of paper is a multidimensional concept consisting of runnability and print quality. The lack of definition for print quality makes printability rather ambiguous. In this paper we discuss the measurability of the high-level printability and print quality and present an interpretation of the measurements of low-level print quality related characteristics as information channels about high-level concepts. This enables the construction of a layered model in which the information provided by measurements is propagated to infer about higher level concepts of quality, eventually supporting decision making. As an example, we present a case study of low-level print quality defects caused by the small-scale measurable properties of the paper, and consider the meaning of this process from the viewpoint of print quality analysis.

Keywords: printability, print quality, Bayesian network

1. INTRODUCTION

The concept of printability of paper is ambiguous yet of high practical importance in paper trade, and in product and process development. Printability refers to the quality potential of the paper as a substrate in a specified printing process [1]. Runnability, i.e., the maximum speed of a printing machine without encountering problems, can also be regarded as a part of printability. A paper of good printability thus does not jam or break in the printing press, withstands post-press operations without ink smearing or papers sticking together, and has a high print quality. The topic of main emphasis in this paper, print quality, is high-dimensional by definition and does not have absolute terms. Thus there exists no generally accepted or formulated way of measuring the overall printability.

Laboratory printing tests can provide useful information about printability [1]. Early research in printability focused on identifying paper property measurements that are related to print quality. Measurement methods that deliver one single value to characterize paper structural aspects were applied; examples are PPS roughness, air leakage porosity or a formation index. These studies (e.g. [2,3]) searched for the interrelations between coarse-scale paper properties and print quality, also integrating parameters related to ink properties and the printing process. The measured paper properties were correlated with parameters describing

printability, such as ink demand, print-through and evenness of the reflectance of printed area [4].

In more recent work 2D measurements of local paper properties have been increasingly employed. Analyzing the microstructure of the paper through the multi-channel 2D measurements is justified by the fact that the microstructure and its inhomogeneity are associated with printability and with the quality of the final printed product. Statistically significant correlation has been established between spatially aligned 2D measurements of paper surface topography, formation and print quality [5,6].

Printability has also been approached from the human assessment point of view. Recently, the attributes that the jury members have used when assessing the quality of printed images, have been systematically analyzed to determine the perceptually relevant quality dimensions [7]. Some relations have been successfully established between physical measures and subjective assessments, for instance within the unevenness of print [8].

As shown above, various measurements are being made on characteristics that are certainly related to printability. However, compared to the strict definition of measurability, as defined by e.g. Ferris [9], Finkelstein [10] and Campbell [11], printability intrinsically is not a measurable characteristic, and neither is print quality; they are not objective.

This paper discusses how the different approaches can be integrated into a unified one and how such measurement approach should be considered from the measurement theory point of view.

We will address this problem in the present paper with the following structure. Section 2 will discuss the basic philosophy of measuring and measurability, and describe generalized measurements as information channels. In Section 3 we will use this formulation and consider the measurement information with regard to assessing print quality. This approach will lead to a natural presentation of information in the form of conditional probabilities that propagate in a network model and support the inference about high-level concepts - and thus also decision making based on measurement information. In Section 4, we will demonstrate a Bayesian network model as a tool for implementing the information flow. We will also present an example of inferring about print quality defects through the examination of small-scale surface topography measurement of paper. Conclusions, both concerning practical printability

assessment and the generalizability of the approach to other areas where human assessment is to be linked with measurement data, will be drawn in Section 5.

2. MEASURABILITY AND INFORMATION CHANNEL

What should the object of examination be like in order to be definable as a *measurable* quantity? As reviewed in [12], Campbell [11] has proposed in 1920: Measurability may be established by, first, “proving that the characteristic under investigation involves an empirical *order relation*”, and second, by either (a) “finding a physical *addition* operation that allows the construction of a reference measurement scale and then performing measurement by comparison with it”, or (b) “finding some *physical law* that allows the measure to be expressed as a function of other quantities”. According to [12], at the time of Campbell’s theory, sensation intensities could not be considered measurable quantities because it was impossible to define an addition operation for them. Later the requirement of additivity has been relieved by, e.g., accepting the equality of *ratios* to form the reference scale, and by utilizing representational theory largely developed among behavioral scientists. However, the requirement of *objectivity* remains in the definitions of measurement (e.g. [9], [10]). It means that, as numbers are assigned to properties in the measurement process, the numbers must be independent of the observer within the error limits. Our target of interest, high-level printability (or the affiliated perceived print quality), is not objective and hence we consider it non-measurable.

How should we mathematically define the concept of measuring? Rossi [13] presents both deterministic and probabilistic models for the measurement process. We apply the probabilistic approach. Let the random variable Y denote the target property that is being measured and let the random variable X denote the observations of Y . We shall allow X and Y to be vector-valued or scalars and the value space of their components may be real numbers, or discrete finite or infinite sets. In the probabilistic definition, the measurement of the target value $Y = y$ is described as

$$f_{X|Y}(x|y). \quad (1)$$

The measurement description is thus equivalent to the probability density (or probability for discrete measurement value space) of the observations, given the target $Y = y$. Thus measurement is an information channel, described as a conditional probability density. The channel carries information about the property that is being measured. Using the Bayes formula, the information about the target, given that measurement value $X = x$ has been obtained, is

$$f_{Y|X}(y|x) = \frac{f_{X|Y}(x|y)f_Y(y)}{\int_{\text{domain}(Y)} f_{X|Y}(x|y)f_Y(y) dy}, \quad (2)$$

where $f_Y(y)$ is the a priori information about the target. This can be assumed uniform, maximum entropy, if no information about the target is available prior to making the measurement. The information carried by the probability densities (1) and (2) is valuable when used in decisions on, say, product development. The estimate of Y is commonly

taken as the value with the highest posterior probability density. The uncertainty is described by the second order terms of Taylor expansion of the logarithm of posterior probability density around the estimate of Y .

The Bayes formula (2) can be generalized also to cases where X or Y or both take discrete values. However, reducing the full measurement information of posterior probabilities to a single estimate value is questionable in this case. The most straightforward approach is to use the entire measurement information, the posterior probability, rather than estimates, in decision making. Many measurement concepts generalize quite naturally to such interpretation. For instance, the sensitivity of a measurement generalizes to comparing the measurement information through Kullback-Leibler distances [14] between the posterior distributions resulting from different measurement values.

Moreover, in practice it makes no difference for the decision maker whether the information comes from a *measurement* in a strict sense, or from an information channel. Namely, in the strict definition of measurement, the uncertainty of the estimate should affect the decisions; also when providing the entire measurement information for the decision maker, she/he must have a specified attitude towards uncertainties. Providing the estimate and its uncertainty as a covariance matrix corresponds to approximating the measurement with a Gaussian probability density.

In summary, all measurements can be thought as information channels, but not every information channel is a measurement in the strict sense.

3. MEASUREMENT INFORMATION ON PRINT QUALITY

We aim at assessing the quality of the print, using instrumental measurements of the paper and the print. The perceptual print quality, as judged by a group of human observers, is the reference data against which the instrumentally measurable properties are compared. This is necessary for identifying the measurement description (1). Now the question addressed is: assuming such perception of a group of observers is consistent enough to specify the reference information, which are the physical features to be measured, and how are the measurement results related to the actual print quality, or to the reality concerning the target? We propose to model these interrelationships as a network with conditional probabilistic connections between the nodes, i.e. a Bayesian network. The data of instrumental measurement in this model/channel propagates through interconnected conditional joint probability densities.

To outline the structure of the model, we start from the subjectively assessed high-level print quality. The jury provides a discrete probability distribution over the predefined discrete scale of qualities. The result from the jury is thus a probability density on classification rather than an estimate of quality. The jury may assess the overall print quality using lower level quality concepts such as naturalness and clarity of details (usefulness) that are also on a discrete scale. The essential difference between the high-level and low-level quality concepts is that the former is

expected to be context dependent while the latter are not. Still, the level of abstractness and subjectiveness is high and the quality concepts are multidimensional. Evidence of both the context - and content - dependence and the multidimensionality of the quality perception can be found, for instance, in [15], where Leisti et al. analyze the data from a subjective paired comparison test augmented by an interview of each observer. The interview data reveals that the evaluators change their criteria for preference when the comparison conditions are changed [15]. The test images of an image quality assessment should therefore be selected very carefully to obtain consistent reference data from the jury.

Studies with ink-jet printing [7] and laser printing [15] have arrived in quite similar lists of attributes that the jury members have typically used when assessing the quality of printed images. These findings are valuable when selecting the relevant attributes to the nodes of the Bayesian network. The attributes fall into several hierarchical levels in the perception of quality. For instance, the frequently mentioned sharpness and brightness represent a lower level than naturalness. To facilitate the construction of a model of the whole information channel, we assume that the lowest perception level consists of special concepts called perceptual quality elements (PQEs). They are assumed to be the attributes of the image that the humans can directly assess and that their assessments - despite the non-physical nature - are objective. Hence a jury would largely have consistent opinions about them. Instrumental measurements of print quality lie on the bottom of the hierarchy together with the measurements of paper quality properties.

We also assume that because of objectiveness all the instrumental measurements are defined as conditional probabilities in which PQEs are to be considered as measurement targets, see (1). The instrumental measurements thus provide information about the reality concerning the PQEs. Eerola et al. have presented an extensive study about the instrumental (or computational) measures of paper and print characteristics and their correspondence with human visual rankings of print quality [16]. Their findings within inkjet printing support the selection of, e.g., paper gloss and brightness, as well as print contrast, mottling and color properties to the model of print quality.

4. BAYESIAN NETWORK AND 2D PROPERTY MAPS

A simplified graphical presentation of the proposed print quality model is shown in Fig. 1. It is a five-layered Bayesian network that realizes the hierarchy discussed in Section 3. The directed edges of the network, i.e. the arrows, describe the probabilistic relations between the nodes. The edges can be identified from a data set that contains parallel observations of the states of all nodes. For instance, identifying the edges between the instrumentally measurable print property layer and the PQE layer requires that both the instrumental measurements and jury's opinions about PQEs have been acquired from the same set of samples. As described in [17], the edges can be identified using e.g.

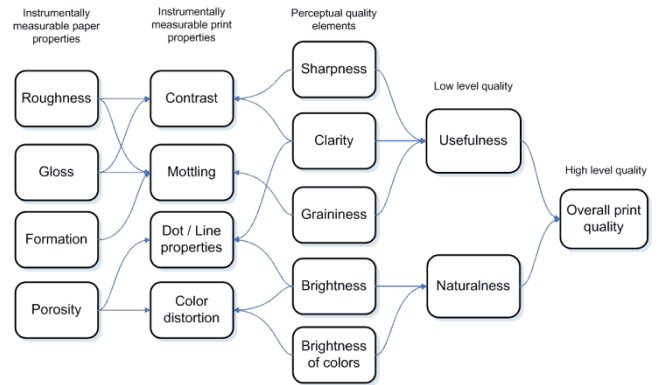


Fig. 1. An example configuration of the Bayesian network for the modelling of print quality.

correlation or mutual information (MI) as a similarity measure between the attributes in the identification data set. Pearson's correlation describes the linear dependence while MI also applies when the relations are nonlinear. The edges are identified as conditional state probability distributions at all combinations of states of the parent nodes.

It must be noted that the positions of the arrows in Fig. 1 are indicative and several other structures of the network are also possible. The data available so far does not support the simultaneous identification of all the edges between the nodes. However, the feasibility of a probabilistic network model in high-level quality assessment has already been shown by, e.g., Pulla et al. [17] who have successfully identified and analyzed a smaller Bayesian network structure in a case study of visual image quality on a laptop display. In the current study, we augment the setup by taking account of the paper and the printing process, and hence introducing the layer of instrumentally measurable paper properties. We present an example of inferring about the occurrence of print defects based on the detection of defects in the paper surface before printing. This example illustrates the use of measurement information under uncertainty.

We examine the relationship between the small-scale 2D measurements of the reflectance¹ of printed paper and the surface topography of unprinted paper. The interpretation is that high values of printed reflectance denote insufficient or missing printing ink. The analysis of the aligned topography and reflectance measurements reveals the degree to which the surface topography has affected the occurrence of such print defects. While earlier studies in the analysis of the aligned 2D maps of paper and print properties (e.g., [5,6]) have focused on identifying deterministic relationships between local paper properties and local print characteristics, we recognize the non-deterministic nature of the dependences and apply the conditional probability distributions as models of measurements and information channels.

The measurement data consists of surface topography maps and reflectance maps acquired from 16 newspaper samples before and after printing by a sheet-fed offset press. All the measurements are camera based and the pixel size is

¹ This is not a true reflectance measurement (as described in [18]) but rather a photographic image of the paper surface.

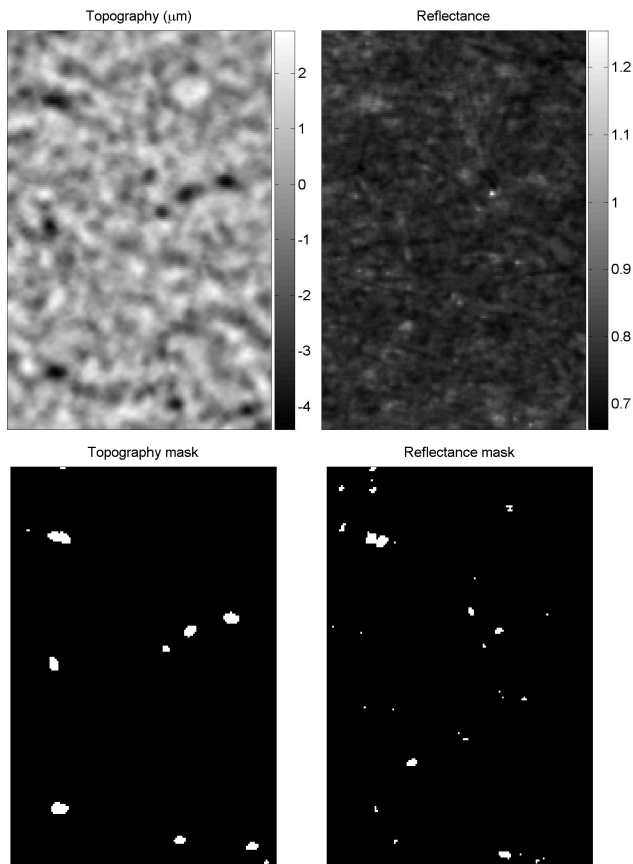


Fig. 2. Aligned measurements (top) and the corresponding anomaly masks on a 1.5 by 2 mm area. Left: unprinted surface topography, right: printed reflectance. The masks indicate 1 % of the lowest topography and 1 % of the highest reflectance points, respectively.

10 μm by 10 μm . The image area is 22.5 mm by 15 mm. The measurements before and after printing have been aligned with subpixel accuracy using a cross-correlation based method [19] and the center area of approximately 2.5 million pixels has been selected for analysis to avoid the geometrically distorted edges. Fig. 2 presents an example of the aligned measurements of unprinted surface topography and printed reflectance, zoomed on a 1.5 mm by 2 mm area to show small details. The lower part of Fig. 2 presents the corresponding anomaly masks that in this case indicate the

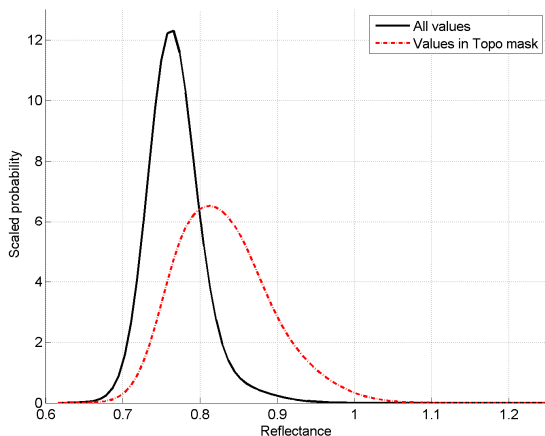


Fig. 3. Marginal (solid black) and conditional (dashed red) probability distributions of printed reflectance values. Both curves have been normalized so that their integrals equal one.

lowest 1 % percentile of the topography map (i.e. the most extreme pits) and the highest 1 % of the reflectance values (i.e. the brightest print defects).

The coincidence of the two masks implies that some of the deep depressions (pits) on the paper surface are responsible for missing printing ink. If there were no dependence between these phenomena, the overlap of the masks would equal the mask percentage, in this case 1 %. In the 16 paper samples analyzed, the average overlap between the 1 % reflectance and topography masks is approximately 15 %. The statistical dependence between surface topography and printed reflectance is also depicted in Fig. 3 by the conditional probability distribution of the reflectance values on condition that the topography value has been classified (by the 1 % mask) as exceptionally low. The conditional distribution predicts clearly higher printed reflectance values compared to the general behavior of the reflectance that is described by the marginal probability distribution. The paper sample used in the illustrations of Fig. 2 and Fig. 3 represents the sample set very well.

The probability distribution approach presented in the above example naturally connects to the Bayesian network idea of analyzing the print quality. Similarly as the detection of paper surface defects leads into information about potential print defects, the low level measurement information in general propagates and interconnects with the other information channels. The nodes of the network will be determined by the quality evaluation task in question and thereby according to the measurement information available. It is expected that the context of the print quality evaluation task will, to a large degree, determine the information that is relevant to be gathered [7, 15, 20].

5. CONCLUSIONS

Typically the printability of paper is understood as the print quality resulting from the interaction between the paper properties and printing parameters. A challenging problem stems from the basic philosophy of measuring as such when applied to paper printability. We have proposed to interpret the technical measurements and the subjective quality classifications as information channels, to be linked together by a Bayesian network model. This is a feasible way to connect the information of various abstraction levels and to support the evaluation of ambiguous - often subjective - characteristics that in the strict sense may not be measurable.

REFERENCES

- [1] [1] J.-E. Levlín and L. Söderhjelm, *Pulp and Paper Testing*, in Papermaking Science and Technology, Fapet Oy. Jyväskylä, Finland, 1999.
- [2] J. M. Fetsko and A. C. Zettlemyer, "Factors affecting print gloss and uniformity", *Tappi*, vol. 45, n°. 8, pp. 667-681, Aug. 1962.
- [3] J. R. Parker, "Fundamental paper properties in relation to printability", *Trans. of the 5th Fund. Res. Symp.*, (ed. F. Bolam), pp. 517-543, BPBIF, London, UK, 1976.

- [4] B. Lyne, "Machine-calendering: implications for surface structure and printing properties", *Tappi J.*, vol. 59, n° 8, pp. 101-106, Aug. 1976.
- [5] G. G. Barros, *Influence of substrate topography on ink distribution in flexography*, PhD Thesis, Karlstad University, Sweden, 2006.
- [6] I. M. Kajanto, "Pointwise dependence between local grammage and local print density", *Paper and Timber*, vol. 73, n° 4, pp. 338-345, 1991.
- [7] P. Oittinen, R. Halonen, A. Kokkonen, T. Leisti, G. Nyman, et al., "Framework for modeling visual printed image quality from the paper perspective", *SPIE/IS&T Electronic Imaging 2008, Image Qual. and System Perform. V*, San Jose, USA, Jan. 2008.
- [8] P. J. Mangin and M. Dubé, "Fundamental questions on print quality", *SPIE/IS&T Electronic Imaging 2006, Image Qual. and System Perform. III*, San Jose, USA, Jan. 2006.
- [9] T. L. J. Ferris, "A new definition of measurement", *Measurement*, vol. 36, n° 1, pp. 101-109, July 2004.
- [10] L. Finkelstein, "Widely, strongly and weakly defined measurement", *Measurement*, vol. 34, n° 1, pp. 39-48, July 2003.
- [11] N. R. Campbell, *Physics - The Elements*, (1920), reprinted as *Foundations of Science*, Dover, New York, 1957.
- [12] G. B. Rossi, "Measurability", *Measurement*, vol. 40, n° 6, pp. 545-562, July 2007.
- [13] G. B. Rossi, "A probabilistic model for measurement processes", *Measurement*, vol.34, n°2, pp. 85-99, Sep. 2003.
- [14] C. M. Bishop, *Pattern Recognition and Machine Learning*, Springer, Singapore, 2006.
- [15] T. Leisti, R. Halonen, A. Kokkonen, H. Weckman, M. Mettänen, et al., "Process perspective on image quality evaluation", *SPIE/IS&T Electronic Imaging 2008, Image Qual. and System Perform. V*, San Jose, USA, Jan. 2008.
- [16] T. Eerola, J.-K. Kamarainen, T. Leisti, R. Halonen, L. Lensu, et al., "Finding best measurable quantities for predicting human visual quality experience", *IEEE Int. Conf. on Systems, Man and Cybernetics*, pp. 733-738, Oct. 2008.
- [17] J. Pulla, M. Mettänen, K. Konkarikoski and R. Ritala, "Bayesian network model as an overall image quality measurement system", *12th IMEKO TC1&TC7 Symp. on Man Science & Measurement*, Annecy, France, Sep. 2008.
- [18] H. F. Rance (ed.), *Handbook of Paper Science*, Elsevier, Amsterdam, 1982.
- [19] M. Lähdekorpi, H. Ihalainen, and R. Ritala, "Using image registration and alignment to compare alternative 2D measurements", *XVIII IMEKO World Congress*, Rio de Janeiro, Brazil, Sep. 2006.
- [20] G. Nyman, J. Radun, T. Leisti, J. Oja, H. Ojanen, et al., "What do users really perceive - probing the subjective image quality", *SPIE/IS&T Electronic Imaging 2006, Image Qual. and System Perform. III*, San Jose, USA, Jan. 2006.

Publication VI

Mettänen, M. (2010): Methods for measuring and predicting the printability of paper. *Nordic Pulp & Paper Research Journal*, Vol. 25, No. 3, pp. 391-404.

© 2010 Nordic Pulp & Paper Research Journal. www.npprj.se.